Fall 2019

Photometric investigations of weathering rinds and coatings with implications for Mars

Kathleen Hoza
Western Washington University, kathleenhoza@gmail.com

Photometric investigations of weathering rinds and coatings with implications for Mars

By

Kathleen Hoza

Accepted in partial completion
of the requirements for the degree
Master of Science

ADVISORY COMMITTEE

Dr. Melissa Rice, Chair

Dr. Michael Kraft

Dr. Sean Mulcahy

GRADUATE SCHOOL

Dr. David Patrick, Interim Dean

Master's thesis

In presenting this thesis in partial fulfillment of the requirements for a master's degree at Western Washington University, I grant to Western Washington University the non-exclusive royalty-free right to archive, reproduce, distribute, and display the thesis in any and all forms, including electronic format, via any digital library mechanisms maintained by WWU.

I represent and warrant this is my original work, and does not infringe or violate any rights of others. I warrant that I have obtained written permissions from the owner of any third party copyrighted material included in these files.

I acknowledge that I retain ownership rights to the copyright of this work, including but not limited to the right to use all or part of this work in future works, such as articles or books.

Library users are granted permission for individual, research and non-commercial reproduction of this work for educational purposes only. Any further digital posting of this document requires specific permission from the author.

Any copying or publication of this thesis for commercial purposes, or for financial gain, is not allowed without my written permission.

Kathleen Hoza

5/30/2019

Photometric investigations of weathering rinds and coatings with implications for Mars

A thesis
presented to
the faculty of
Western Washington University

In partial fulfillment
of the requirements for the degree
Master of Science

By
Kathleen Hoza
June 2019

Abstract

Reflectance spectroscopy is a major technique for characterizing the composition of planetary surfaces, and has led to many key findings in planetary geology including the identification of an aqueous, neutral-pH environment on Mars. In laboratory measurements, reflectance spectrometers typically acquire data using a standard, fixed viewing geometry (e.g. incidence angle = 0 degrees, emission angle = 30 degrees). Measurements from orbital or in-situ spacecraft, however, may be acquired at a wide range of viewing geometries, depending on the orientation of the instrument relative to the target surface and the Sun. For many materials, the impact of viewing geometry on reflectance is minor; however, some materials' spectral signatures can be significantly influenced by these photometric effects. In particular, spectra of weathering rinds and rock coatings are likely to show photometric variability due to a number of factors which have only been characterized to a limited extent in previous studies. Because most planetary surfaces are weathered to some degree, understanding these effects may have far-reaching implications for planetary geology. In this work, our goal is to better constrain how photometric properties of Mars-analog surfaces vary as a function of the composition and microtexture of weathering rinds and coatings. We developed a new automated goniometer to enable the collection of reflectance spectra across a range of viewing geometries similar to those of spacecraft observations. We acquired spectrogoniometric measurements for naturally-weathered and synthetically-coated Mars analog samples (Columbia River Basalts), which we further characterized using scanning electron microscopy (SEM), atomic force microscopy (AFM), and x-ray diffraction (XRD). Our results show that thin (<10 microns) silica coatings on basalt substrates are not detectable at standard viewing geometries but exhibit diagnostic photometric effects including increased specularity and changes in slope parameters

in the visible and near-infrared. Additionally, we find that weathering processes may strongly influence the shapes of scattering lobes, with some naturally-weathered samples found to change from forward scattering to backscattering depending on the degree and nature of sample weathering. Collectively, these results show that photometric observations can provide significant insight into the weathering of Mars-relevant rocks. Because weathering occurs in the near-surface environment, this information could ultimately lead to an improved understanding of martian paleoclimate and contribute to assessments of martian habitability.

List of Figures and Tables

1. Introduction

Because of Mars' potential for ancient habitability, numerous past, present, and planned future missions from NASA and other space agencies have targeted Mars for research and exploration. Mars' capacity to support ancient life is largely investigated through observations of martian surface mineralogy (e.g. Bishop et al., 2004; Bibring et al., 2006; Ehlmann et al., 2008; Murchie et al., 2009, Grotzinger et al., 2013; Arvidson et al., 2014), which can yield clues to past and present environmental conditions including temperature, pH, and abundance of liquid water. One of the major techniques for characterizing mineral compositions is reflectance spectroscopy, which involves measuring the amount of light a surface reflects across a range of wavelengths to produce a reflectance spectrum. Many mineral identifications on Mars depend on a few key absorption bands diagnostic of specific minerals. For example, pyroxene and olivine, which are major constituents of the Mars' basaltic crust, both show Fe^{2+} crystal field effect absorptions around 900-1000 nm, but crystallographic differences between the two minerals shift the specific position of this absorption slightly (Figure 1A). Under the right conditions, weathering of basalt may produce smectite clays (e.g. Bishop et al., 2008), and new absorptions appear including an Fe^{3+} charge transfer absorption at ~500 nm, H_2O and OH^- vibrational overtones at 1400 nm and 1900 nm, and a metal-OH interaction creating an absorption near 2200 nm with the exact position depending on the specific composition of the clay (Pommerol and Schmitt, 2008) (Figure 1B). Silica, which can sometimes be an indicator of aqueous alteration, has similar hydration absorptions at 1400 nm and 1900 nm but lacks the Fe^{3+} absorption, and the metal-OH absorption is broadened due to a combination of two absorptions from Si-OH bend (~2210 nm) and stretch (~2260 nm) (Rice et al., 2013) (Figure 1B). On Mars, this particular distinction might be relatively difficult to observe in situ because

any of these signals may be influenced by the ubiquitous nanohematite dust, which also has an Fe^{3+} absorption centered at ~500 nm (e.g. McSween and Keil, 2000) (Figure 1B).

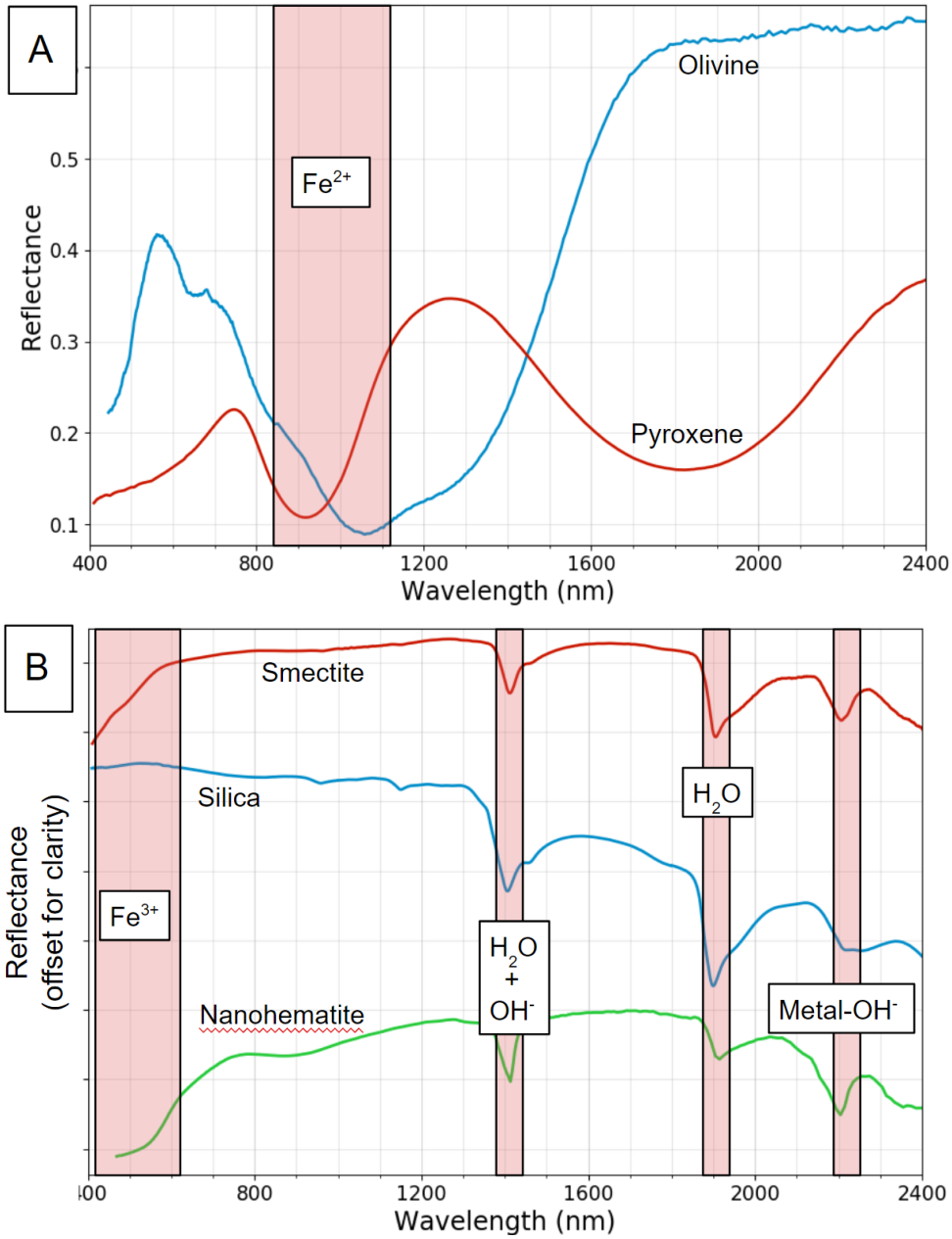

Figure 1: Reflectance spectra are shown for common minerals in basalt (A) and other martian materials (B). Labeled absorptions include an Fe^{2+} crystal field effect absorption in pyroxene at 900 nm and olivine at 1050 nm, a broad Fe^{3+} charge transfer absorption at ~500 nm in smectite clay and nanohematite, and H_2O vibrational absorptions in silica, smectite, and nanohematite.

Observations of absorption features like these have led to key findings relating to martian habitability, which include the characterization of an aqueous, neutral-pH environment in Mars' past (e.g., Ehlmann et al., 2012; Grotzinger et al., 2013) as well as the detection of the continued presence of trace amounts of briny surface water in Mars' present environment (e.g. Horgan and Bell, 2012).

As well as being correlated with specific mineralogical compositions, spectral signatures are known to vary as a function of viewing geometry, which is defined by the angular relationships between a light source illuminating a surface, a target material, and a detector measuring reflectance (Figure 2).

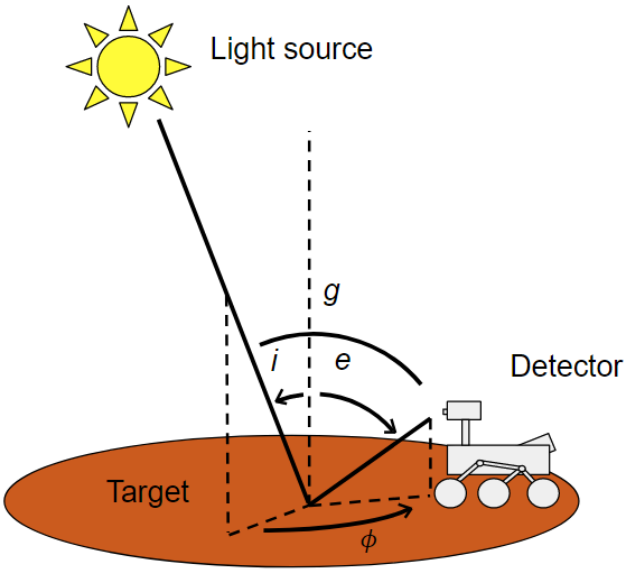

Figure 2: A viewing geometry is defined by an emission angle *e*, incidence angle *i,* and azimuth angle ϕ. Phase angle *g* is the angle between *e* and *i.*

One area of particular interest is the effect of viewing geometry on the reflectance spectra of weathered and coated rocks. These materials are important environmental indicators because they form in response to the near-surface environment. This means they can help inform assessments of the environment in which they are found, which may in turn have implications for habitability. Weathering rinds and coatings also influence spectral measurements of the rocks they form on, and it is necessary to understand their effects in order to effectively understand the bulk compositions of rocks measured with reflectance spectra. Although weathering rinds and coatings are known to have phase-dependent reflectance, that phase dependency has only been characterized to a limited degree in previous studies (e.g., Fischer and Pieters, 1993; Johnson et al., 2006). We aim to address this *problem* through investigating the following *hypothesis,* which will have significant *implications*:

- *Problem statement:* The effects of viewing geometry on the spectra of natural rock surfaces have potential to illuminate martian surface geology but are poorly understood.
- *Hypothesis:* Photometric properties of Mars-analog surfaces will vary as a function of the composition and microtexture of weathering rinds and coatings.
- *Implications:* Quantifying these variations will aid in characterizing martian surfaces and ultimately contribute to assessments of martian habitability.

In order to assess this hypothesis, we have characterized spectral and photometric effects for a suite of Mars analog weathering rinds and coatings in the laboratory. As a step toward linking the observed spectrophotometric effects to physicochemical causes, we have also characterized the mineralogy, chemistry, and microtexture of these same rinds and coatings along with their corresponding unaltered interiors. These characterizations have enabled us to

correlate specific types of coatings and rock weathering characteristics with specific spectrophotometric effects. If these same spectrophotometric effects were to be observed for martian rocks, it would be possible to form hypotheses about those martian rocks' likely textural and compositional characteristics. And, if the processes that lead to the formation of those textures and compositions on Earth are known, it could be concluded that those same processes might have affected the observed rock surfaces on Mars. Ultimately, inferences like this will result in an improved understanding of martian surface conditions and contribute to assessments of martian habitability.

The collection of photometric data for this study required the use of a system that enabled precise, high angular resolution (less than or equal to 5 degrees) positioning of a light source and detector relative to a weathered rock target material. Additionally, direct comparisons needed to be possible between spectra taken at different geometries, so that changes could be quantified from one geometry to the next, and data collection needed to be time-efficient and repeatable. A handful of instruments like this, all custom-built, exist at laboratories conducting photometric research. However, each existing goniometer was designed and fabricated for a specific research purpose, and while collaborations with other investigators were informative, the requirements of this project with regard to angular resolution, sample accommodation, and time-efficient automated data collection were not met by any existing goniometer. For this reason, it was necessary to design and fabricate a new custom goniometer in order to meet the requirements outlined above.

In order to produce a dataset with relevance to a wide array of past, present, and future Mars instruments, this study focused on wavelengths from 350-1350 nm, which is relevant to

numerous Mars multispectral imagers including Pancam on the Mars Exploration Rovers (MER) Spirit and Opportunity (Bell et al., 2003), Mastcam on Curiosity (Malin et al., 2010) and Mastcam-Z on Mars 2020 (Bell et al., 2014). In addition, this study also investigated longer near-infrared wavelengths out to 2500 nm in order to take full advantage the capabilities to other missions including the Compact Reconnaissance Imaging Spectrometer for Mars (CRISM) instrument on NASA's spacecraft Mars Reconnaissance Orbiter (MRO) (Murchie et al., 2007).

2. Background and Significance

2.1 Weathering rinds and coatings on Earth and Mars

Rock coatings and weathering rinds form in specific near-surface environments, and the detection of specific types of rinds and coatings can yield information about the environments in which they form. In some cases, minerals known to form in specific weathering environments have been linked to specific visible/near-infrared (VNIR) spectral signatures. For example, in martian stratigraphy, basalt in many areas is overlain by smectite clays which are in turn overlain by Al-rich phyllosilicates including kaolinite. Smectites are associated with basalt weathering in arid environments with low water:rock ratios whereas kaolinite has been found to form in areas with high rainfall and high water:rock ratios (Righi and Meunier, 1995; Borchardt, 1989), so these sequences on Mars could be interpreted as evidence for a relatively dry period followed by a period with abundant liquid water. Using analog basalts from the Deccan Traps, Greenburger et al., 2013 found that the depths of hydration features in VNIR spectra were directly correlated with the degree of alteration of their samples and could be used to differentiate unaltered basalt, moderately altered smectite-rich samples, and heavily altered kaolinite-rich samples. However, this work did not address the detection of these minerals when

present only as very thin rinds, and photometry might provide a way to detect them when their abundance is too low for VNIR signatures to be measurable.

Despite the importance of understanding basalt alteration to investigations of paleoclimate, significant uncertainty remains regarding exactly what phases are created during weathering processes. For example, Michalski et al., 2006 showed that weathered basalts have clay signatures in the thermal infrared (TIR) but did not show that clays increased from the interior to the rind. This leaves open the possibility that these clays were not formed during near-surface weathering and could instead have formed via an alternate process such as hydrothermal alteration at the time of rock formation, and more work is needed to investigate the conditions under which weathering of basalts results in clay formation. Also of interest is the fact that diagnostic absorption features for these same clays were not observed in VNIR spectra of the same rocks (Michalski et al., 2006). One hypothesized cause of this absence from VNIR spectra is that the clays are present only in thin rinds and microfractures at abundances invisible to VNIR spectroscopy. Photometry might provide a means to detect these low-abundance materials where spectroscopy overlooks them.

Like alteration products, coatings deposited on top of existing rock surfaces can be important environmental indicators. For example, on Earth, amorphous silica coatings have been interpreted to form from liquid water flowing across dusty rock surfaces, dissolving and then re-precipitating silica along the way (Dorn et al., 2013, Figure 3). Similar coatings have been hypothesized to exist on Mars (Kraft et al., 2003), and if they formed through similar aqueous processes then this could be evidence for relatively abundant liquid water at the time of deposition. However, alternative mechanisms exist for the deposition of amorphous silica. A

20-year laboratory experiment showed that silica coatings can also form in environments where water is present only as water vapor (Dorn, 2013). Without more precise characterization of detectable differences between coatings produced in these two different weathering environments, the possibility remains open that silica glazes on Mars could be the result of billions of years of water vapor interactions rather than fluid flows. This means that improving our ability to recognize spectral signatures of coatings that formed in wet versus dry environments could improve our understanding of surface geologic processes on Mars. Additionally, detection of more specific chemical characteristics of silica-coated rocks could provide additional insights into environmental conditions at the time of deposition. For example, if silica is transported in a low pH aqueous environment, this has been shown to facilitate the leaching of cations from the parent rock coupled with the preservation of network bonds, whereas full dissolution and reprecipitation processes are more likely to occur in relatively high pH environments (Minitti et al., 2007).

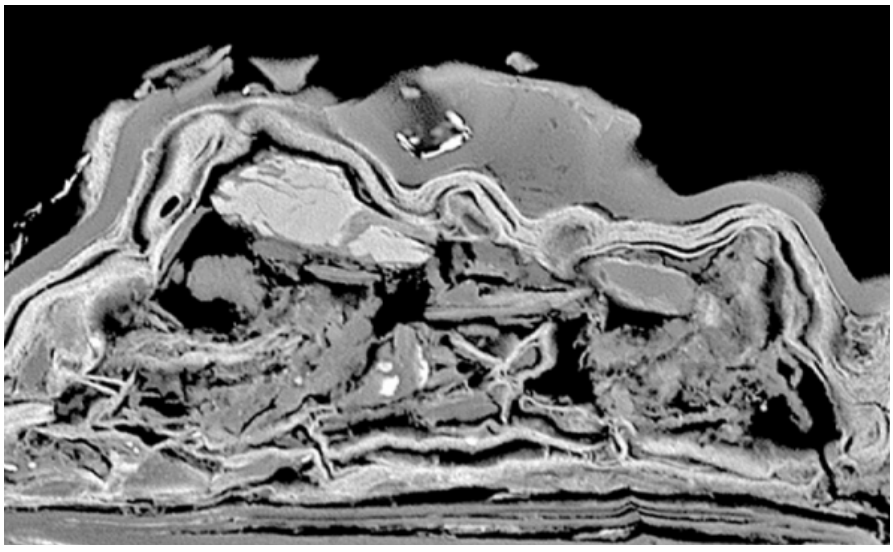

Figure 3: A back-scattered electron (BSE) image of a complex coated surface including a top layer of water-mobilized and transported silica. The presence of similar coatings on martian surfaces could indicate that similar aqueous conditions existed on Mars. Credit: Dorn et al., 2013.

In addition to being important in their own right, weathering rinds and coatings can also influence other measurements of martian reflectance. Spectroscopy can be very sensitive to low-abundance materials (Ehlmann et al., 2012) which means that when insufficiently understood, coatings can mask substrate signatures entirely and lead to significant misinterpretations of bulk rock composition. For example, thermal infrared (TIR) spectra have been interpreted to indicate large-scale presence of silica-rich rocks such as andesites on Mars (Bandfield et al., 2000). However, differentiation of martian crust into large quantities of felsic material would be unexpected based on the current understanding of martian crustal dynamics, and an alternative hypothesis has been proposed suggesting that these felsic signatures could instead be induced by thin coatings of silica-rich precipitates masking spectral signatures of underlying basaltic bulk compositions (Wyatt and McSween, 2002). This alternative model is supported by investigations of both VNIR and TIR spectra of unaltered basalt surfaces coated in the laboratory with silica-rich precipitate coatings (e.g., Kraft et al., 2003; Seelos et al., 2010). Another globally significant spectral trend is that dark regions of Mars have been shown to have an overall negative slope in the infrared (Johnson et al. 1999, Figure 4). This slope has been interpreted to arise from the widespread presence of thin ferric coatings on martian surfaces. These coatings are bright relative to their basaltic substrates, and at short wavelengths they are opaque, resulting in a comparatively bright signal. At long wavelengths, the coatings become transparent, and the signal is dominated by the dark spectrum of the underlying basalt. Because these coatings are present across large regions of Mars, understanding how they influence spectral data could have implications for many martian observations.

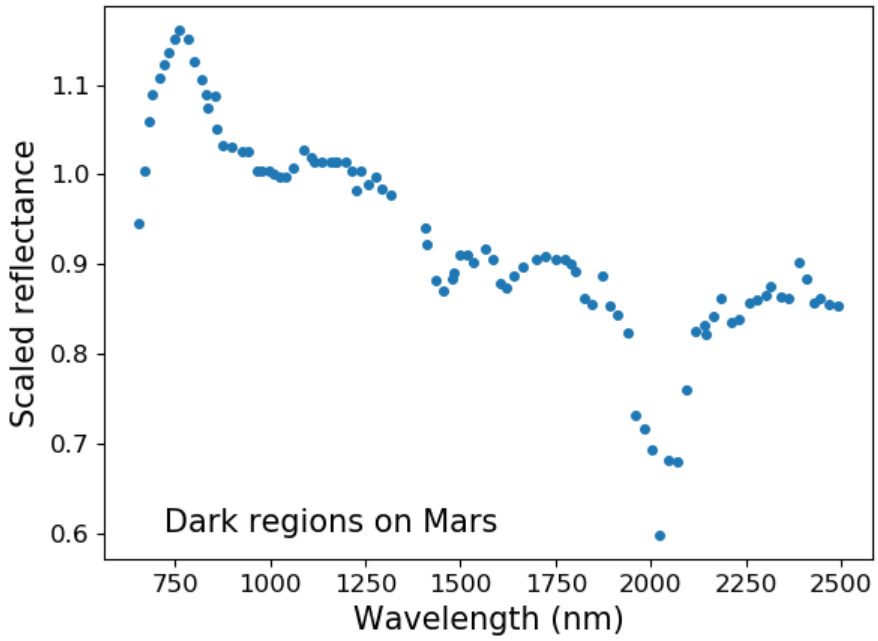

Figure 4: Dark regions on the martian surface are less reflective at longer wavelengths in the near infrared. Data extracted from Fischer and Pieters, 1993.

While current remote sensing and in-situ techniques have been used to characterize potential coatings and rinds on Mars to an extent, challenges continue to limit our understanding of these materials. For example, laser ablation spectroscopy has been a very effective tool for studying chemistry of many martian materials (Wiens et al. 2012). Because spectra from the first few pulses of laser activity are typically ignored, however, this technique may miss the presence of a rind or coating altogether. Reflectance spectroscopy, on the other hand, can be so influenced by low-abundance coatings that substrate signatures are lost entirely (e.g. Kraft et al., 2003). By introducing photometry as an additional tool for the characterization of potential rinds and coatings, more comprehensive interpretations of martian surface environments will be made possible.

2.2 Effects of viewing geometry on observations of weathered surfaces

Photometric effects are known to potentially influence spectral signatures, but work done to quantify the effects of viewing geometry on the spectra of natural rock surfaces has so far been limited. Instead, it is common practice to assume that laboratory spectra collected at a standard viewing geometry can be directly compared with spacecraft data, which may be taken at a wide range of geometries. Many surfaces reflect light nearly isotropically, and for those materials these assumptions introduce only minimal error. However, the limited work that has been done on photometry of martian surfaces has shown that these materials do exhibit changes in reflectance with viewing geometry, with photometric behavior ranging from backscattering to forward scattering (e.g. Johnson et al., 1999; Johnson et al., 2013). Furthermore, Hapke modeling allows those changes to be tied to physical properties of the target materials. For example, photometric variability has been used to make interpretations regarding porosity and particle size distribution for rocks and soil at the Pathfinder landing site (Johnson et al., 1999).

While any material's reflectance spectra may be influenced by viewing geometry, rocks with thin coatings or rinds are particularly likely to display photometric variability. One factor which may contribute to this sensitivity is that increasing path length through a coating at high phase angles increases the ratio of light-coating interactions to light-substrate interactions (Figure 5).

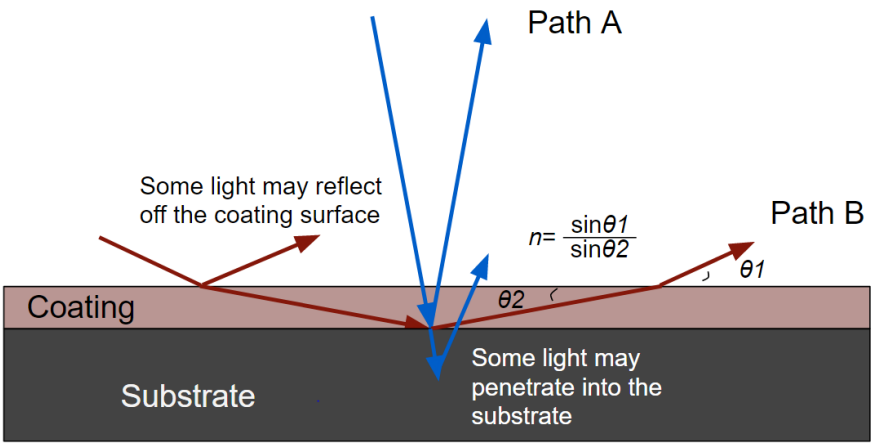

Figure 5: A light ray traveling at small incidence and emission angles (A) will interact with a translucent coating across a shorter path length than a light ray traveling at a high phase angle (B). Path length is also influenced by the index of refraction *n*, and light components may reflect from any point in the depth profile of the material (surface, within coating, coating-substrate boundary, or within substrate).

This may be the cause of photometric effects observed for rocks with laboratory-created ferric coatings. These coated rocks, which consist of thin layers of relatively bright ferric oxides deposited onto dark basalt substrates, become progressively darker at longer wavelengths when measured at standard viewing geometries, which is consistent with the trends described previously for large dark regions of Mars (Johnson et al. 1999, Fischer and Pieters 1993). However, spectral signatures of these ferric coatings can vary significantly with viewing geometry, with the trend of decreasing reflectance at longer wavelengths actually reversing at high phase angles (Figure 6). This phase reddening effect could be the result of the longer light-coating interaction path at high phase angles increasing the contribution from the coating and decreasing the contribution from the dark substrate beneath. However, it should also be noted that phase reddening has also been observed for martian and lunar soils (e.g. Johnson et al., 2013), and for these materials, phase reddening might be the result of other effects. For example, longer wavelengths have a general tendency to be relatively forward scattering, which could also contribute to bright signals at high phase angles (Fischer and Pieters 1993).

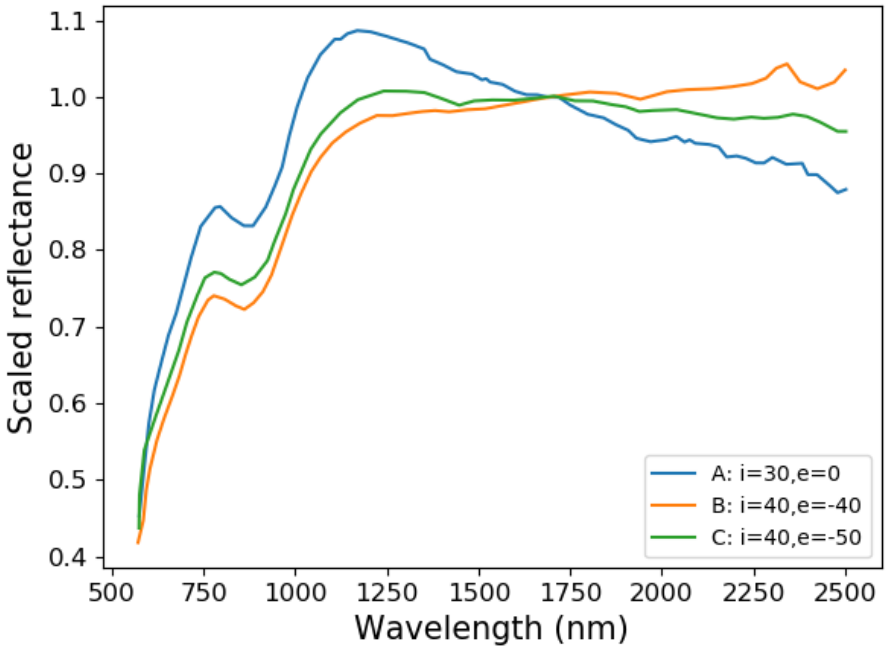

Figure 6: Spectra of basalt with a 225 micron ferric coating. NIR slopes are negative at forward scattering geometries (A, B) but positive at a backscattering geometry (C). Data extracted from Fischer and Pieters, 1993.

Other coatings, such as the silica-rich coatings discussed above, have high potential to smooth previously rough surfaces by filling in gaps. This can increase specularity of reflectance spectra and has been suggested as a possible cause of mirror-like reflectance at the Pathfinder landing site (Kraft and Greeley, 2000). Because weathering rinds and coatings are both widespread on Mars and also photometrically sensitive, a more quantitative understanding of coating photometry may provide key insights into martian mineralogy and climate.

2.3 Existing spectrogoniometer facilities

In order to study the photometry of weathering rinds and coatings, it is necessary to use a goniometer to precisely position a light source and detector relative to the target material. A

survey of goniometers existing prior to this project shows that none could satisfactorily meet the needs of this experiment, and because of this, a new goniometer needed to be constructed.

A goniometer was recently developed at the California Institute of Technology (Caltech) for planetary photometry research (Figure 7). It allows for a full range of incidence, emission, and azimuthal variation with 1 degree of angular resolution and a minimum phase angle of 15 degrees. However, the Caltech goniometer is not automated and the sample and goniometer arms must be manually positioned at each geometry. Photometric characterization of even a small suite of rock surfaces requires the collection of spectra at many hundreds of configurations, which would make the use of this goniometer time-prohibitive.

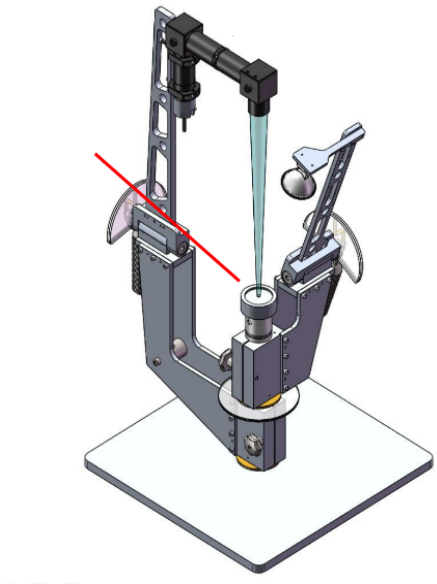

Figure 7: A custom goniometer at Caltech allows for precise relative positioning of a light source, detector, and target material, but must be manually positioned at each viewing geometry. Credit: modified from E. Graff, Caltech.

An automated goniometer designed to enable time-efficient collection of reflectance spectra has been built in the Bloomsburg University Goniometer (BUG) Lab (Figure 8). It has angular resolution of <1 degree and can accommodate phase angles from 3 degrees to 140 degrees, and can collect a full hemisphere of bidirectional reflectance data in about 1.5 hours for a single sample. However, the sample space for this goniometer is designed primarily to accommodate either powders or flat sheets such as those used for calibration target materials. This project will require taking a survey of spectra from cobble to small boulder-sized samples to gain a representative understanding of weathered basalt photometry, and these samples would not fit into this goniometer.

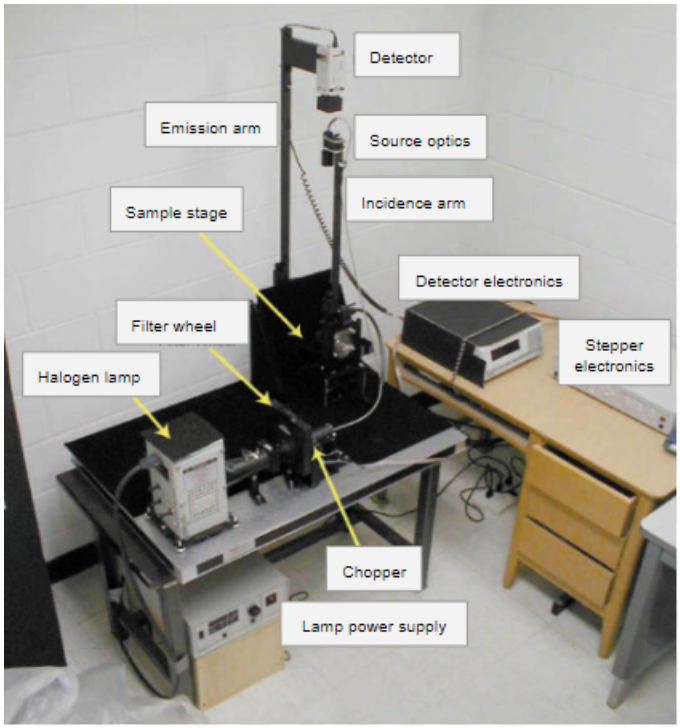

Figure 8: An automated goniometer at Bloomsburg University. Modified from Shepard, 2001.

Another automated goniometer was constructed at the Catholic University of Leuven (Figure 9) (Biliouris et al 2007), which also interfaces with an ASD spectrometer. Using this goniometer, it is possible to collect bidirectional reflectance data over a full hemisphere in ~2.5 hours for a single sample, and the geometry of this goniometer could allow for cobble-sized samples. However, this goniometer has angular resolution limited to 15 degrees for incidence and emission and 30 degrees for azimuth, which is not as high as the desired angular incidence and emission resolution of 5 degrees. Additionally, there is no capability to automatically transition between samples, or between samples and a white reference. This decreases efficiency of data collection, and also means that this goniometer does not re-calibrate to its white reference over the entire course of its 2.5 hour data collection cycle. It is standard practice to re-calibrate ASD spectrometers regularly throughout data collection in order to account for spectrometer drift (e.g. Cloutis et al., 2007. In WWU's spectroscopy lab, this is done every ~10 minutes). This raises questions about whether instrument instability might influence results from this setup.

Figure 9: A custom goniometer at the Catholic University of Leuven, Netherlands. Credit: Biliouris, 2007.

Overall, in order to meet project requirements with regard to time efficient data collection, sample accommodation, and angular resolution, it was necessary to construct a new custom goniometer at Western Washington University. This goniometer is fully automated, has 1 degree of angular resolution, a minimum phase angle of 15 degrees, and can accommodate either one large sample or a suite of up to 5 smaller samples along with a white reference.

3. Methods

3.1 Methods overview

In order to meet our research objectives, we first designed and built a spectrogoniometer system capable of measuring reflectance spectra of naturally-weathered rocks at a range of geometries. This step is described in detail in section *3.2 Automated spectrogoniometer system development.* Next, we developed a suite of Mars-relevant sample materials including basalt with precipitated silica-rich coatings and naturally-weathered surfaces. This step is described in detail in section *3.3 Sample collection and synthesis.* Finally, using our new spectrogoniometer system, we characterized the photometric properties of these samples. These properties were then linked to the mineralogy, chemistry, and microtexture of these samples as determined using a combination of other analytical techniques available at WWU. This step is described in detail in section *3.4 Data collection.*

3.2 Automated spectrogoniometer system development

3.2.1 Overview

A 2-dimensional design was selected for the goniometer with pivoting arms to hold the light source and detector (Figure 10). This experimental setup allows for the rapid, automated collection of reflectance spectra for multiple rocks (powders, slabs or hand samples) at a wide range of given geometries. For example, spectra for a suite of 5 samples at 10 different viewing geometries each can be acquired in under 1 hour, including time for data processing and plotting.

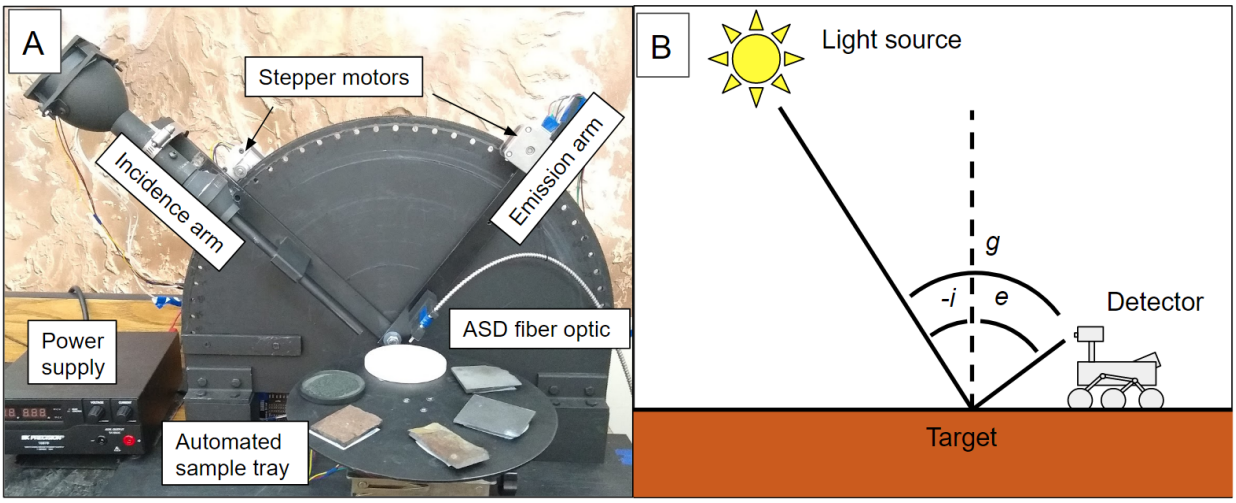

Figure 10A: A 2-dimensional goniometer enables reflectance spectra to be taken at a range of geometries. 10B: A 2-dimensional viewing geometry is defined by an emission angle *e* and incidence angle *i*. Phase angle *g* is the angle between *e* and *i*.

The system is controlled via two open source software packages, which are available on github at https://github.com/westernmarslab/autoasd and https://github.com/westernmarslab/autospec. The packages are also available on PyPi and may also be installed using the commands *pip install autoasd* and *pip install autospec*.

3.2.2 Goniometer system hardware

To facilitate the collection of photometric data, a goniometer has been constructed to interface with WWU's reflectance spectrometer (see Figure 10A). It consists of an aluminum backboard with two rotating arms, one holding a light source and the other holding a detector. Azimuth angle is held fixed at 0 or 180 degrees, and incidence and emission angles can vary from 0 to 90 degrees with a minimum phase angle of 15 degrees based on geometric limitations. Stepper motors attached to the incidence and emission arms enable automatic iterations through geometries with 1 degree of angular resolution, which enables efficient collection of spectra at high angular resolution. When using the automation features, incidence angles are currently restricted to -50 to 50 degrees, and emission angles are currently restricted to -35 to 65 degrees because of mechanical limitations and geometric constraints. This geometric range was deemed sufficient to reproduce the vast majority of observations taken by orbital and ground-based reflectance spectroscopy instruments.

Samples may be positioned using either 1) a manually adjusted sliding tray for large samples or 2) an automated rotating tray for smaller samples. The manually-operated tray can accommodate samples up to 7 inches tall, and the automated tray can hold 5 samples 3 inches in diameter, plus a disc of Spectralon® as a white reference material. This Spectralon® white reference material has been shown to be a near-isotropic scatterer at the relevant viewing geometries (Jackson et al. 1992) and a correction is applied to account for the non-Lambertian behavior that does exist (see section *3.1.2 Calibration*). This means that it is possible to collect a white reference at each viewing geometry, which corrects for the effects of changes in illumination spot size and detector field of view.

This instrument incorporates a light source based on the design used by the HOSERLab at the University of Winnipeg (Cloutis et al. 2006). It incorporates a USHIO FCS lightbulb and is powered by a BK Precision 1687B switching mode DC power supply. The bulb is rated at 150 W, but is run at 20 V and 114 W. This slightly decreased power output helps to reduce noise from heating the samples and detector.

Signal is collected by a fiber optic cable with a 25 degree field of view, giving it a spot size with a diameter of 1.3 cm on the sample when emission is 0 degrees. This cable channels input signal to an Analytical Spectral Devices, Inc. (ASD) FieldSpec 4 Hi-Res spectrometer, which has three internal detectors collecting signal across 2151 channels. The detectors are a 512-element silicon array VNIR detector that measures from 350-1000 nm, and two graded index InGaAs photodiode Near Infrared (NIR) detectors that measure signal from 1001-1800 nm and 1801-2500 nm, respectively. Together, these detectors allow for sampling at a resolution of 3 nm from 350-700 nm and 8 nm at 701-2500 nm.

3.2.3 Goniometer system software

3.2.3.1 Architecture

Custom software is used to operate the system via three computers all connected to a local spectroscopy lab network. The three computers are as follows:

1. Control computer. This is where the user gives input. Software running on this computer includes a Python Tkinter Graphical User Interface (GUI) that allows the user to input all parameters relating to sample configuration, spectrometer configuration, and desired

viewing geometries. This GUI also displays information about the current state of the system and includes a log of all actions taken during the current session (Figure 11).

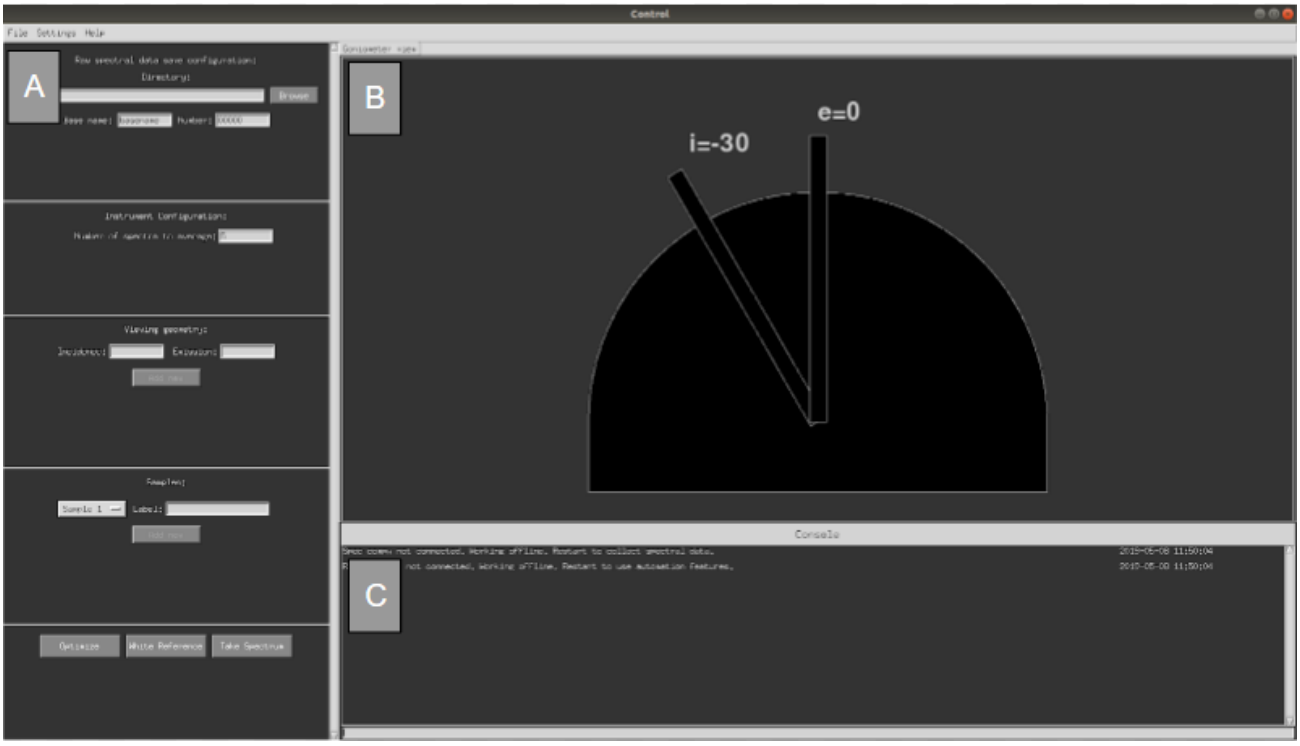

Figure 11A: Custom control software allows a user to give inputs regarding sample and instrument configuration and desired viewing geometries. 11B: A graphical representation of the goniometer gives the user a quick way to make sure the system is operating nominally. 11C: Information about actions taken during the current session are logged in a console.

2. Spectrometer computer. This computer is controlled via command files generated by the control computer and dropped into a shared folder on the local network. Following instructions in these command files, it runs GUI automation software that operates ASD's proprietary spectrometer control software (RS3) and spectral processing software (ViewSpec Pro). This enables the instrument to be optimized and a white reference taken at each viewing geometry. After each run of data collection, this spectral

processing software is used to apply a splice correction to remove artifacts generated at the positions where spectrometer detectors overlap.

3. Raspberry Pi. This computer is also controlled via command files generated by the control computer and dropped into a shared folder on the local network. Following instructions in these command files, it operates the motors driving the goniometer arms and sample tray.

3.2.3.2 Analytical tools and data visualization

As well as allowing the user to operate the goniometer and spectrometer, the software developed for this system includes a suite of tools that can be used to view and analyze spectrophotometric data. In the simplest case, spectra are plotted with wavelength on the x-axis in nanometers and reflectance relative to a lambertian reflector on the y-axis, and the parameters described below are plotted as a function of phase angle g = e - i (see Figure 10 above).

Key analytical capabilities include the following:

1. Normalizing spectra - Given a wavelength input by the user, all selected spectra are normalized by finding reflectance at that wavelength and dividing the full spectrum by that value (Figure 12).

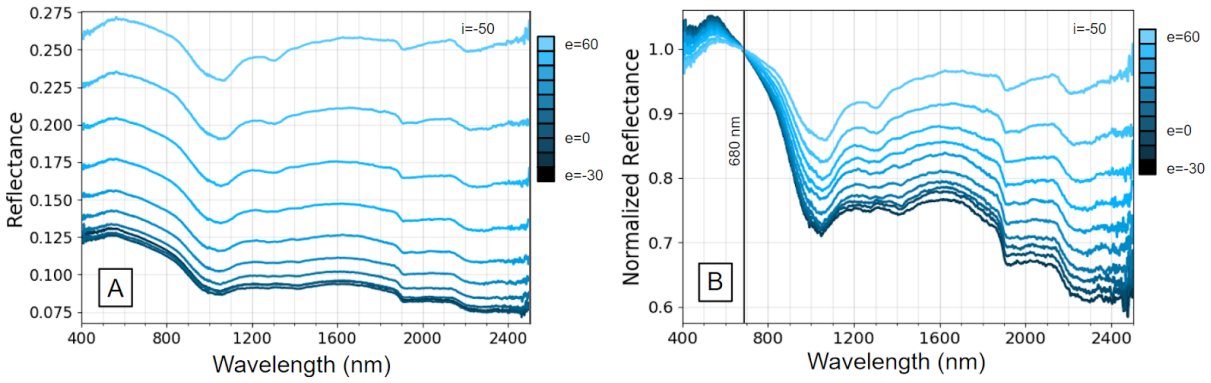

Figure 12: Spectra before (A) and after (B) normalization. In this case, the normalization wavelength specified was 680 nm.

2. Calculating spectral slope - Given a range of wavelengths, the software calculates slope for all selected spectra as the change in relative reflectance divided by the change in wavelength in nm (Figure 13).

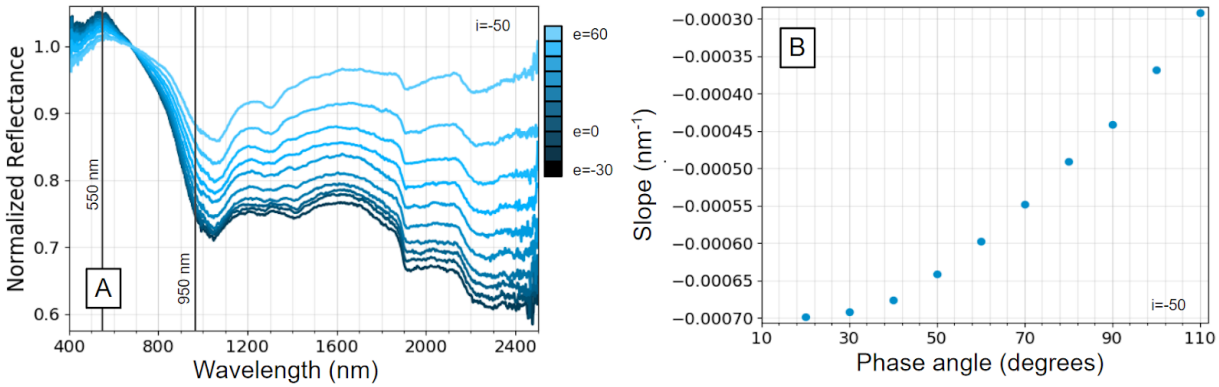

Figure 13: Spectral slopes are calculated from a range of wavelengths identified for spectra of interest (A) and can be plotted as a function of phase angle *g* (B). In this case, slopes are calculated from 550-950 nm and are shown to become less negative as phase angle increases.

3. Calculating band centers and depths - Given two shoulder locations input by the user, the software first identifies the continuum slope as a straight line between those shoulders. Then, the maximum and minimum values for reflectance are found within those wavelength ranges, and the differences are calculated between those points and

the continuum slope. If the difference is greater for the minimum value, that value is identified as the band center and band depth is reported as the positive ratio of that difference to the continuum reflectance at that point. Or, if the difference is greater for the maximum reflectance value, that value is identified as the band center, and the band depth is reported as the negative ratio of that difference to the continuum reflectance at that point (Figure 14).

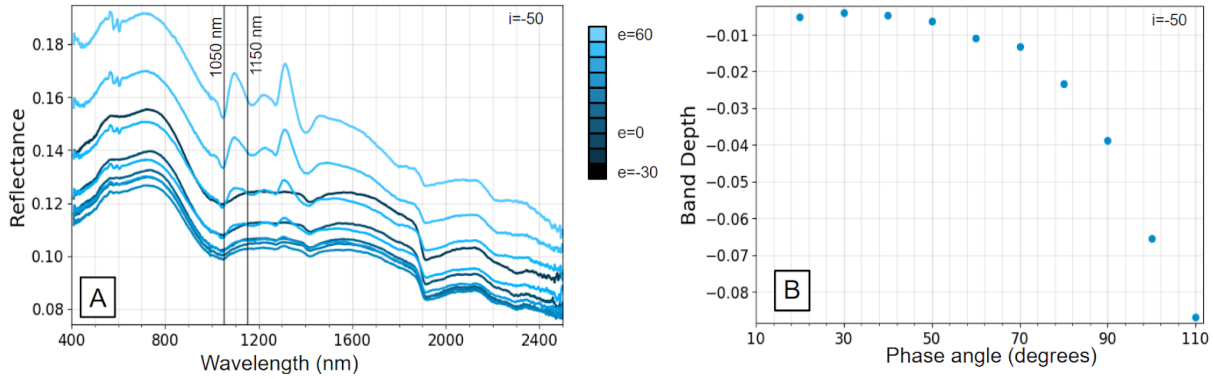

Figure 14: Band depth is measured as distance from a continuum calculated as a linear interpolation between reflectance at two shoulders identified by the user. In this case, shoulders are placed at 1050 and 1150 nm and band depth is negative.

4. Calculating average reflectance - Given a start and end wavelength, average reflectance is calculated as the mean value of reflectance over this range (Figure 15). For this project, when reflectance is reported at a single wavelength (e.g. 680 nm), the reported value is still averaged over a 4-6 nm range centered on that wavelength in order to minimize the impact of noise.

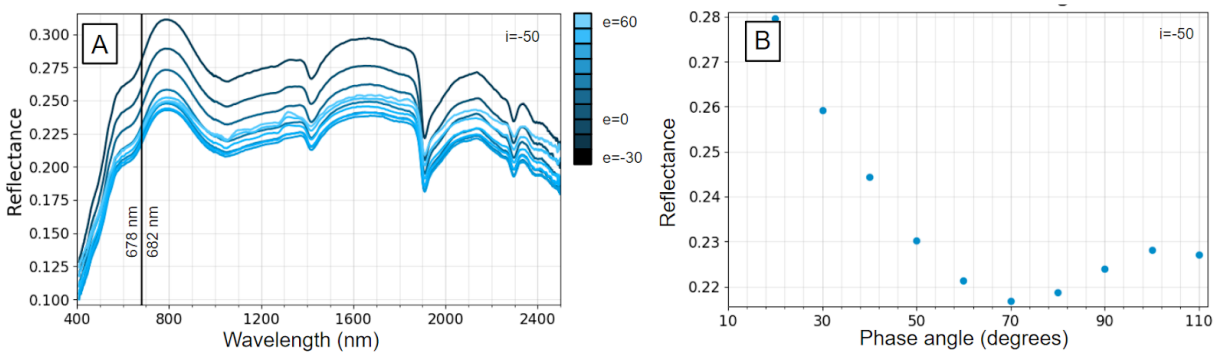

Figure 15: Reflectance at 680 nm is measured by averaging reflectance from 678-682 nm (A) and plotted as a function of phase angle (B)

5. Calculating non-reciprocity - Helmholtz reciprocity is calculated as the difference in relative reflectance between two reciprocal measurements for a given sample. See section *5.1.2 Helmholtz reciprocity* for a detailed discussion and examples.
6. Adding offset to spectra - To clearly see spectra from multiple samples on a single plot, it can be useful to add offset to some spectra (Figure 16).

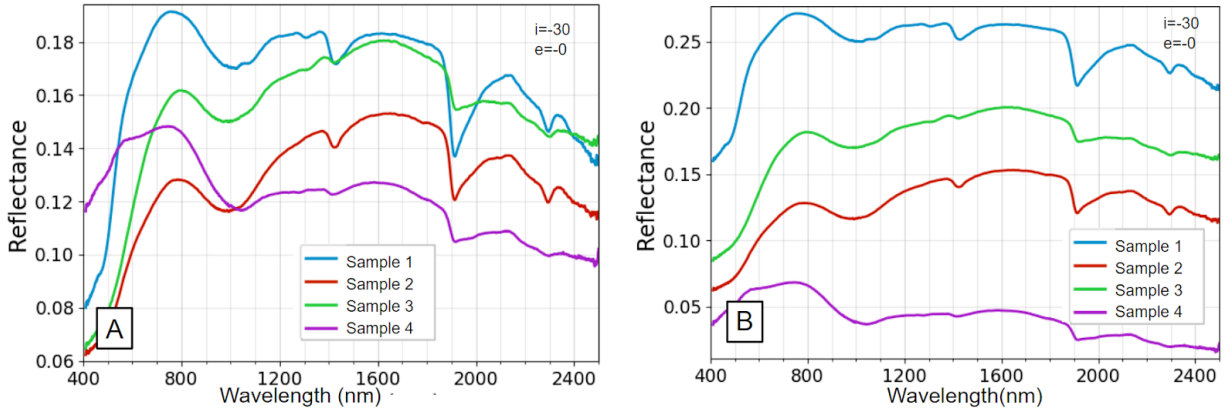

Figure 16: Overlapping spectra (A) can be hard to interpret, but adding offset to samples can add clarity (B).

7. Excluding suspect data - Some wavelength ranges have been found to be prone to polarization artifacts (see section *5.1.1 Polarization artifacts in high-phase angle measurements* for detailed discussion) and the software provides an option to remove

this data from results displayed, instead replacing it with a dashed line showing a linear interpolation between reflectance values measured at safe wavelengths (Figure 17).

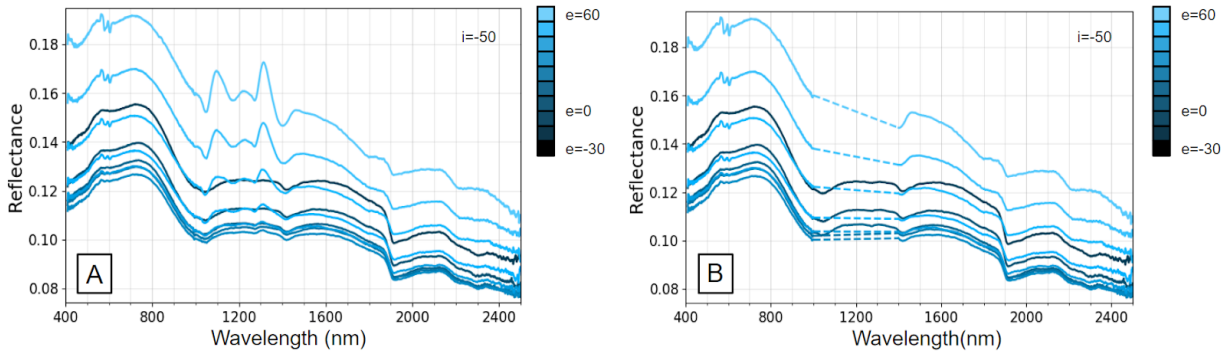

Figure 17: Polarization artifacts are known to affect wavelengths from 1000 to 1400 at high phase angles (A), so these wavelengths are omitted from our results (B).

When interpreting spectra taken at a wide range of geometries, alternative visualization techniques can be beneficial for displaying some photometric behaviors. For example, hemispherical plots showing reflectance (as calculated above) on the radial axis and emission angle varying with theta can be used to show the shapes of scattering lobes much more effectively than the original spectra (Figure 18).

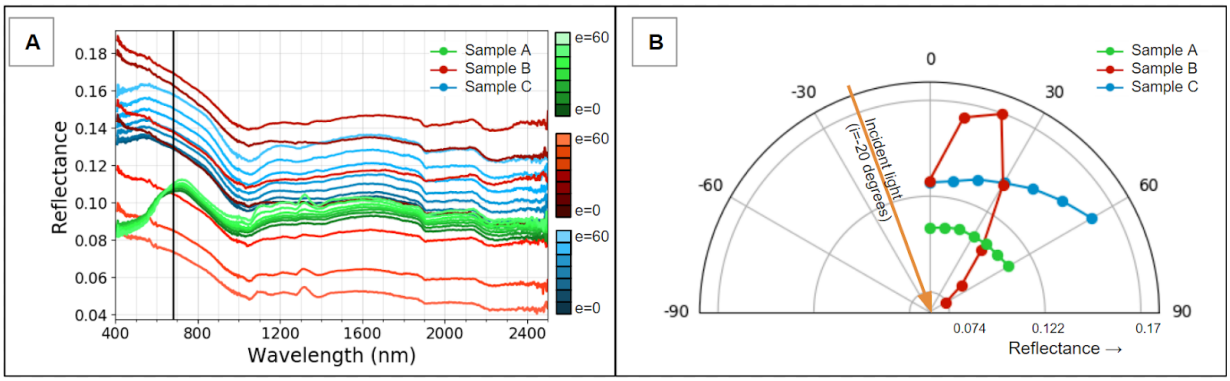

Figure 18: Reflectance is measured at 680 nm for three samples at an incidence angle of -20 degrees and emission angles varying from 0 degrees to 60 degrees (A). This data is then plotted on a hemispherical plot with reflectance on the radial axis and emission angle varying with theta (B).

Given the multi-dimensional nature of a photometric dataset, any of these techniques can become cluttered. To visualize data across a full range of viewing geometries, it is often more effective to use a heat map with emission angle on the x-axis, incidence angle on the y-axis, and a third parameter such as reflectance at each point represented by a color scale (Figure 19A-B). These heat maps can be used to show any of the spectral parameters described above, for example the slopes of normalized spectra from 550-950 nm are shown in Figure 19C-D. Note that the data collected with our spectrogoniometer system will always lie within a triangular region where $i \leq e - 15^o$. This is because geometric constraints on our system prevent the light source and detector arms from crossing, or from being closer than 15 degrees apart. For the data shown in Figure 19, the two arms were kept at least 20 degrees apart.

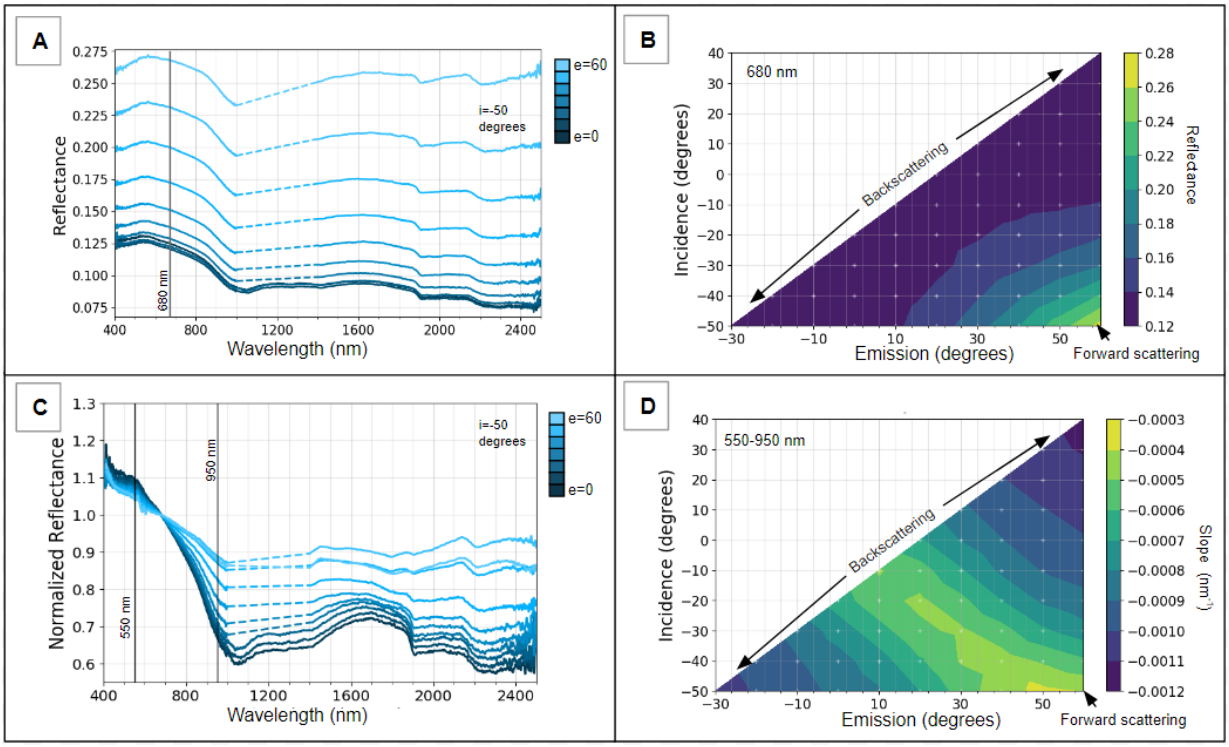

Figure 19A: Reflectance is measured at 680 nm from spectra at all viewing geometries for a given sample (incidence=-50 shown here). 19B: Reflectance is then plotted as a heat map in incidence, emission space with a color scale representing a range of reflectance. 19C: For a different sample, slope from 550-950 nm is measured for normalized spectra at all viewing geometries (incidence = -50 displayed here). 19D: Slope is then plotted on a heat map over incidence, emission space with the color scale corresponding to different slopes.

3.2.3 Goniometer system calibration

The ideal white reference material would have perfectly diffuse reflectance at all viewing geometries. In practice, such a material does not exist, and Spectralon® has been shown to have some geometry-dependent reflectance (Figure 20). To correct for this non-Lambertian behavior, measurements are scaled to published Spectralon® reflectance values using a linear interpolation when needed. These values were measured for light with a 680 nm wavelength, and for this reason photometric properties are measured at 680 nm when other characteristics of the spectra do not interfere with doing so.

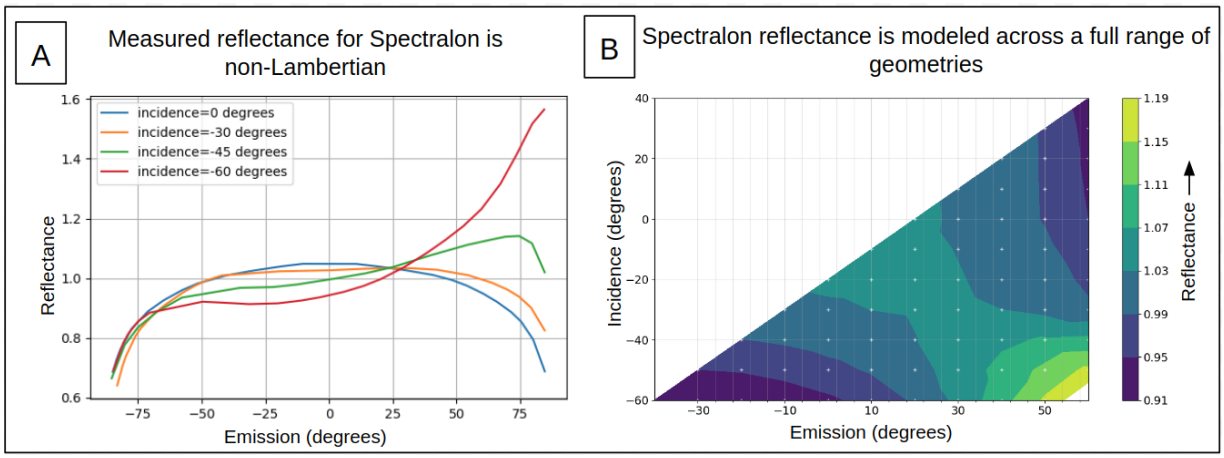

Figure 20: Reflectance data for Spectralon® was extracted from Biliouris et al., 2007 for a few viewing geometries (A). A linear interpolation is used to model reflectance at all relevant viewing geometries (B).

3.3 Sample collection and synthesis

3.3.1 Naturally-weathered basalt surfaces

Sixteen naturally-weathered Columbia River Basalt (CRB) samples were collected from the Roza flow at two study sites in the Channeled Scablands of eastern Washington State - Dry Falls and Frenchman Coulee (Figure 21). Samples were selected to provide a representative

overview of weathering patterns observed in the area, which has been identified in previous studies as a reasonable Mars analog site for weathered basalt (e.g. Wyatt and McSween 2002, Kraft et al. 2003, Michalski et al. 2006). A Munsell color chart was used to identify appropriate color descriptors.

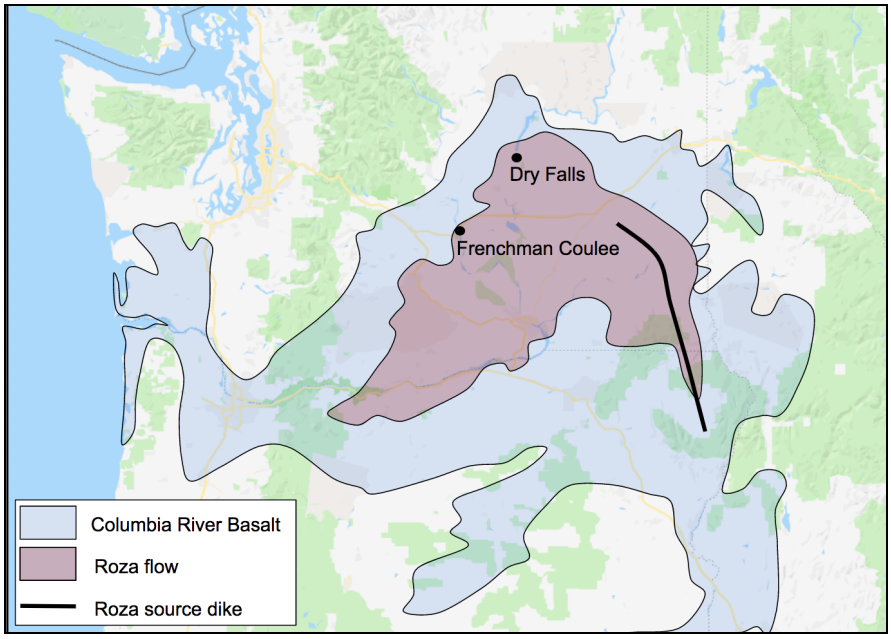

Figure 21: Columbia River basalt (red) covers much of eastern Washington and northern Oregon. The Roza flow is shown in red with a dark line indicating its source dike location. Study sites are marked in red. Data extracted from Camp et al., 2017 and Google Maps.

3.3.2 Unaltered basalt interiors

To study the unaltered interiors of weathered basalts and to prepare substrate materials for coated samples, CRB samples were cut with a rock saw to expose the interiors. These were cut into billets approximately 5 cm x 8 cm x 0.4 cm, which were then polished using 120 grit silicon carbide and ultrasonically cleaned.

3.3.3 Synthetic coating precipitation

A silica coating solution was made by using distilled water to dilute a 40% colloidal SiO_2 solution produced by Alfa Aesar to a 2.5% solution. A Fe(III)-rich coating solution was produced by taking this silica solution and adding 2% by weight nanohematite (30-50 nm diameter particles of Fe_2O_3 produced by Alfa Aesar). These solutions were then precipitated onto unaltered basalt billets by placing the unaltered samples onto a hot plate turned to medium heat and then coating them with a succession of 80 spritzes of solution, which was anticipated to create a coating 4 microns thick, from a spray bottle following Kraft et al. 2003. For the Fe-rich solutions, the bottle was agitated between each spritz in order to keep the nanohematite in suspension. In order to confirm the even distribution of precipitated coating material, these samples were examined in a Tescan Vega 3 Scanning Electron Microscope (SEM) operating at variable pressure with N_2 gas in the chamber, which does not require the samples to be carbon-coated or otherwise altered.

3.4 Data collection

3.4.1 Scanning Electron Microscopy (SEM)

WWU's Tescan Vega 3 scanning electron microscope was used to characterize the composition and morphology of unaltered interior samples and weathering rinds. Additionally, cross-sections of silica-coated samples were examined under SEM in order to characterize coating thickness and changes to surface topography. In preparation for SEM analysis, rocks were first embedded in Spurr resin (Electron Microscopy Sciences), which is a low-viscosity epoxy intended to penetrate and preserve potentially friable rinds and coatings, and then cut into cross-sections with a rock saw and polished to 1 μm smoothness. To prevent charging during SEM analysis, samples were coated with approximately 20 nm of carbon.

During data collection, the instrument was operated at an accelerating voltage of 10-15 kV with a working distance of 20 mm. Chemical composition maps were created using an Oxford 80 mm^2 Energy Dispersive Spectroscopy (EDS) detector, and Aztec software was used to extract spectra from regions within these maps and calculate semi-quantitative compositions of crystals identified in the rocks.

3.4.2 Atomic Force Microscopy (AFM)

To characterize changes in topographic profiles induced by the application of coatings, an unaltered basalt sample and a silica-coated basalt sample were each analyzed using a Bruker Bioscope Catalyst instrument operated in tapping mode. Conical silicon probes (Nanoscience Instruments) with a theoretical resolution of 8 nm were utilized with resonant frequencies near 300 kHz. 40-70 line scans across areas of a few hundred μm^2 were combined to form topographic surface images using NanoScope Analysis software. This data was used to provide a 3-dimensional view of surface texture/topography as a complement to 2-dimensional SEM cross-sectional images.

3.4.3 X-ray diffraction (XRD)

As a complement to SEM mineralogical characterization, WWU's PanAnalytical MRD Pro XRD machine (Cu $K\alpha$ x-ray source) was used to analyze the mineralogy of both the interior and exterior of each weathered sample selected for detailed study. XRD results from the rinds were compared to XRD results from the interiors in order to investigate any significant changes to mineralogy. To prepare powders for this process, rock interiors were crushed using a ball mill and weathered exteriors were mechanically separated using a Dremel rotary tool. The XRD

machine was run at 45 kV with a dwell time of 0.5 seconds per step and step size of 0.02 degrees. Data was collected from 3 to 55 degrees 2-theta.

Additional XRD data was collected for the clay-size (<2 micron diameter) fraction of the rind and interior of a naturally weathered rock specimen. To create these clay-fraction samples, powders were first prepared as described above for both the rind and interior of a rock. Then, these powders were added to beakers containing water 5 cm deep. The mixtures were stirred, sonicated, and then allowed to settle for 4.5 hours. Assuming particles settled following Stokes' Law, this resulted in particles ~2 microns in diameter or smaller remaining suspended in the fluid while larger particles sank to the bottoms of the beakers. Approximately 15 mL of fluid with clay-sized particles in suspension was extracted from these beakers and 0.1 g of sodium hexametaphosphate was added as a dispersive agent. These mixtures were then centrifuged at 8700 rpm for 10 minutes to concentrate the suspended minerals. The resulting solid material in each centrifuge tube was mixed with ~1 mL of water, and the slurry was spread across a glass slide and allowed to air dry overnight to preferentially orient clay minerals with their (001) planes parallel to the slide . XRD data was collected for each of these slides using the XRD machine operating at 40 kV and 20 mA with a dwell time of 3 s and a step size of .04 degrees. Although data was collected from 3-55 degrees 2-theta, the focus is on the 3-12 degree range since that is the key region for detecting clay signatures.

Clay composition can be further constrained by observing the degree to which lattice spacing expands when samples are treated with a liquid, commonly ethylene glycol. Following Poppe et. al., 2001, a slide containing a sample of the clay-size fraction of a naturally-produced weathering rind (prepared as described above) was placed on a shelf in a desiccator containing

ethylene glycol, and the desiccator was placed in an oven heated to 70 degrees Immediately after the sample was removed from the dessicator, XRD data was collected (40 kV, 20 mA, step size of .04), which enabled the quantification of the change in d-spacing effected by this treatment before the glycol evaporated from the sample.

3.4.4 Spectroscopy and Photometry

Naturally weathered samples, unaltered interiors, and coated basalt samples were all spectrally and photometrically characterized using WWU's new automated spectrogoniometer system (described in detail in section *3.2 Automated spectrogoniometer system development* above) to collect VNIR reflectance spectra at incidence angles from -50 to 30 degrees and emission angles ranging from -30 to 60 degrees with 10 degrees of angular resolution.

4. Results

4.1 Synthetically-coated sample results

4.1.1 Overview

Basalt substrates were found to consist primarily of labradorite, augite, olivine, and a felsic interstitial glass along with minor amounts of ilmenite and apatite. Also present was an altered mafic phase thought to be a weathering product of the other rock components. Standard geometry (i=-30, e=0) VNIR spectra show an Fe^{3+} absorption at ~500 nm along with an Fe^{2+} absorption at 900 nm and hydration features at 1400, 1900, and 2200 nm. The addition of a microns-thick amorphous silica coating made standard geometry spectra darker, but had minimal impact on absorption features' depths or positions. However, when spectra were taken at a range of geometries, observed photometric changes were significant. These included

increased specularity, which is likely related to smoothing of wavelength-scale roughness, as well as distinctive behavior from 550-950 nm and 1500-1700 nm.

4.1.1 Basalt substrate chemistry and mineralogy

SEM analysis shows that the basalt substrate used to create coated samples consists of labradorite (elongate crystals up to 500 microns in length), augite (~200 micron crystals), olivine (~150 micron crystals), ilmenite (~200 micron crystals), a felsic interstitial glass, and a mafic altered phase (Figure 22, Table 1). These results are confirmed by XRD data showing similar mineralogy (Figure 23).

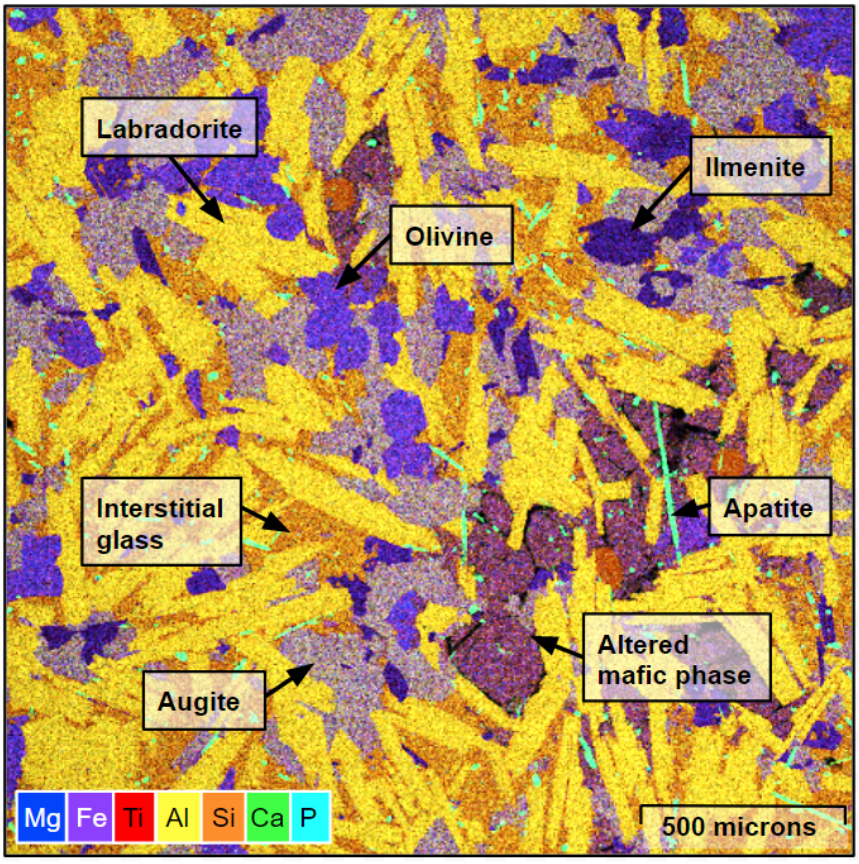

Figure 22: Phases identified in the basalt substrate include labradorite, Fo_{36} olivine, augite, ilmenite, and apatite. The substrate also contains a potassium-rich interstitial glass and an altered mafic phase. See Table 1 for chemistry.

Table 1: Composition of phases identified in the basalt substrate using SEM EDS analysis.

	Plag	Olv	Aug	Ilm	Ap	Altered mafic phase (average)	Interstitial glass
Weight % oxide							
SiO_2	56.29	32.46	51.38	0	0	50.7	74.99
FeO	0	51.09	13.69	47.72	0	37.2	0
Al_2O_3	28.24	0	2.94	0	0	4.6	12.87
MgO	0	16.44	14.11	1.86	0	4	0
CaO	10.63	0	17.89	0	60.11	2.4	0
K_2O	0	0	0	0	0	0.6	8.97
Na_2O	4.84	0	0	0	0	0.4	3.16
TiO_2	0	0	0	50.42	0	0	0
P_2O_5	0	0	0	0	39.89	0	0
Total	100	99.99	100.01	100	100	99.9	99.99
Cation per formula unit							
# oxygen	**8**	**4**	**6**	**3**	**26**	**6**	**N/A**
Si	2.52	0.98	1.93	0	0	2.029	-
Fe	0	1.29	0.43	1.01	0	1.245	-
Al	1.49	0	0.13	0	0	0.217	-
Mg	0	0.74	0.79	0.07	0	0.239	-
Ca	0.51	0	0.72	0	11.25	0.103	-
K	0	0	0	0	0	0.031	-
Na	0.42	0	0	0	0	0.031	-
Ti	0	0	0	0.96	0	0	-
P	0	0	0	0	5.9	0	-
Cation sum	**4.94**	**3.01**	**4**	**2.04**	**17.15**	**3.895**	**-**

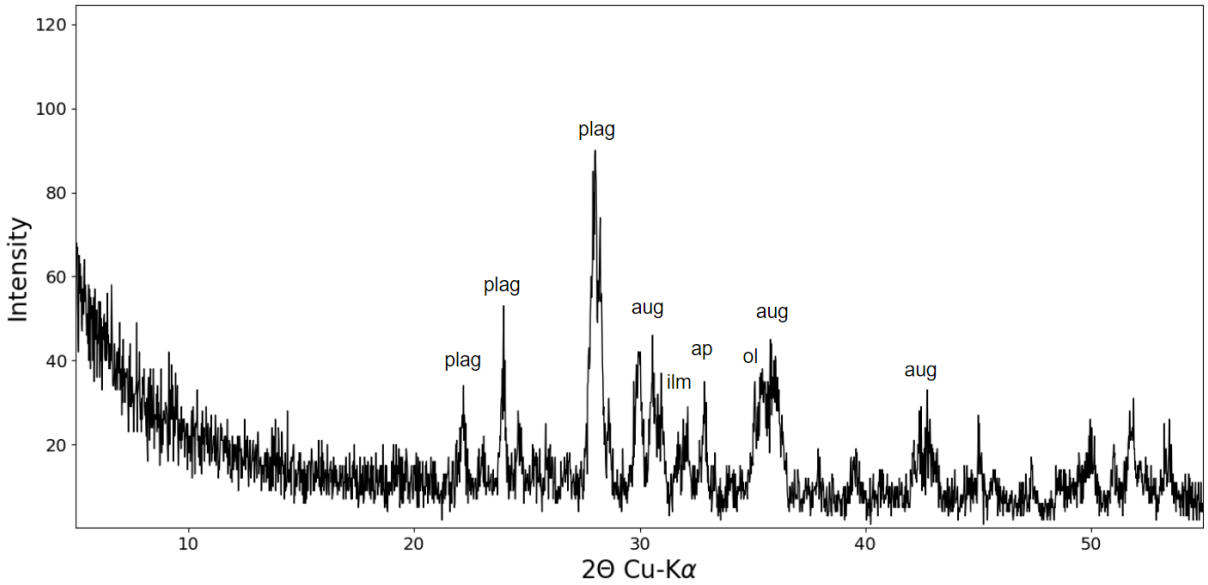

Figure 23: XRD data from a powdered sample of the basalt substrate shows peaks consistent with labradorite, augite, iron-rich olivine, ilmenite, and apatite. This confirms minerals identified from EDS data.

4.1.2 Coating distribution and morphology

Variable pressure SEM images show that the silica coating was distributed fairly evenly across the surface of the basalt sample, although it appears to settle into topographic lows and at topographic highs it becomes thin enough to allow signal from the underlying mafic materials to show through (Figure 24A). For the Fe-rich coating, although the silica component was similarly distributed across the substrate surface, the nanohematite was seen to aggregate into clumps up to ~50 microns in diameter rather than distributing evenly (Figure 24B).

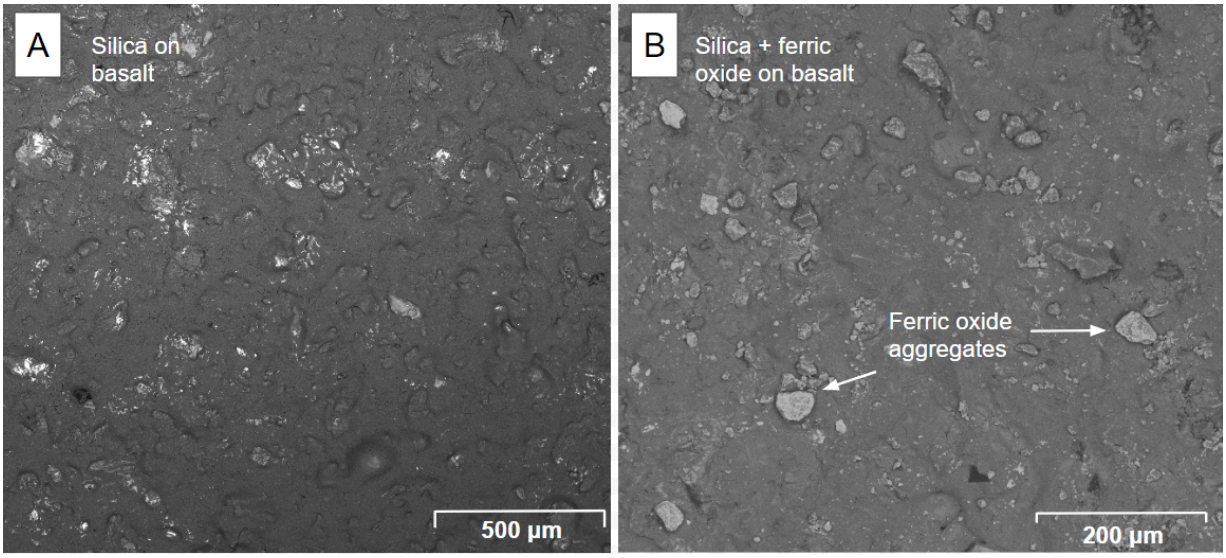

Figure 24A: Low-vacuum backscattered electron (BSE) SEM image of a silica coated sample. The coating is draped over the entire surface, but bright areas show that the coating is thin at topographic highs, allowing the bright basalt surface to show through the darker silica. Figure 24B: Low-vacuum backscattered electron (BSE) SEM image of a ferric oxide and silica coated sample. Ferric oxide forms aggregates of up to ~50 microns instead of remaining evenly distributed through the coating.

SEM images of a silica-coated sample cross section show that the coating smooths out surface roughness on the wavelength scale (<2 microns) while leaving large topological features intact (Figure 25A). This is further confirmed by AFM data (Figure 25B).

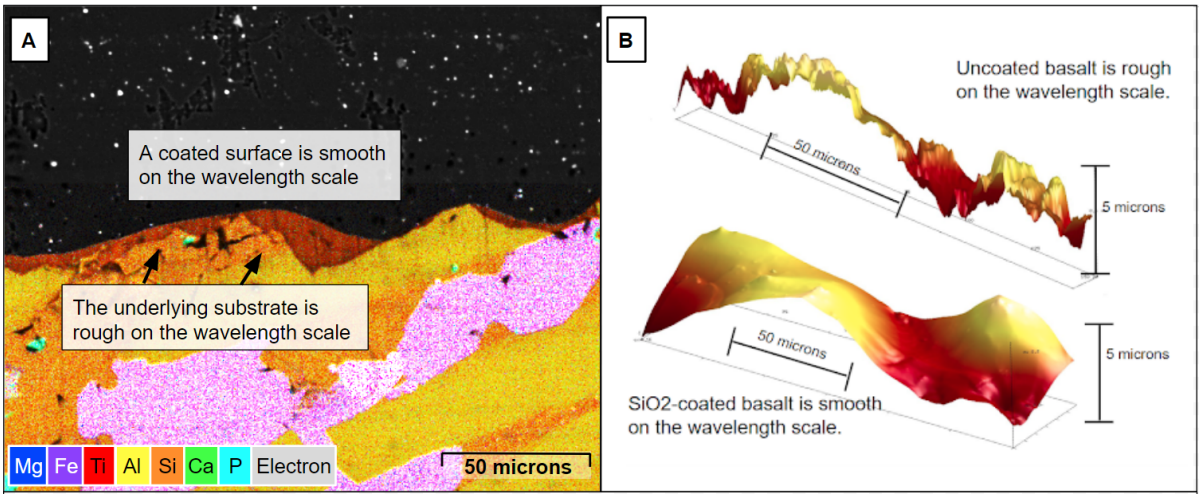

Figure 25A: A coated basalt cross-section is shown by overlaying an EDS composition map on an SEM BSE image. Compositional data shows a thin layer of amorphous silica (dark orange) draped over the substrate basalt surface (lighter orange, yellow, purple). BSE data (grayscale) shows the micron-scale fractures and roughness of the underlying substrate, which the coating smooths out while leaving larger topographic features intact. Figure 25B: This smoothing effect is confirmed in AFM images showing basalt surface roughness with and without an SiO_2 coating.

4.1.3 Spectroscopic and photometric effects of silica coatings

When measured at standard viewing geometries, spectra for coated and uncoated samples are largely indistinguishable, with similar band depths for Si absorption features (Figure 26A). However, when measured at a range of viewing geometries, two key differences become apparent. First, coated samples are far more specular than uncoated samples with the brightest reflectance occurring where *i*=-*e* and reflectance decreasing symmetrically on either side of that point (Figure 26B).

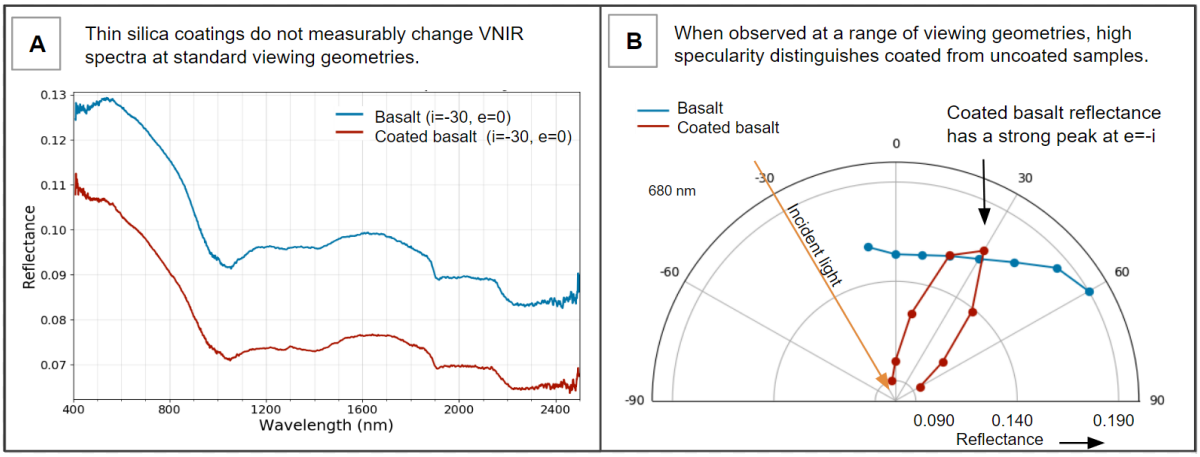

Figure 26A: Standard geometry spectra for a silica-coated basalt sample and its unaltered substrate (A) show minimal impact on diagnostic absorptions including the Fe^{2+} absorption at ~1050 nm, a hydration band at 1900 nm, and an Si-OH stretch absorption at ~2200 nm. However, a hemispherical plot for the same two samples showing reflectance at 680 nm on the radial axis and emission angle on the theta axis (B) shows significant differences in the shapes of the scattering lobes with the uncoated sample showing forward scattering behavior and the coated sample displaying specular reflection.

Additionally, coated samples are found to have distinctive photometric behavior in the spectral slopes from 550-950 nm (Figure 27A) and 1500-1700 nm (Figure 27B). For coated samples, the 550-950 nm slopes are flattest at the specular points (where *i*=-*e*) and become progressively steeper at geometries farther from that point. For uncoated samples, the photometric change in this slope is less than half the magnitude of the change for coated samples. And, it occurs in an

somewhat different pattern with the flattest slopes occurring at forward scattering geometries and slopes becoming steeper toward backscattering geometries. The spectral slope 1500-1700 nm also varies with viewing geometry for SiO_2-coated samples, with the most negative slopes occurring at forward scattering geometries, the most positive slopes occurring at backscattering geometries, and slopes near zero measured for moderate viewing geometries. For uncoated samples, this slope remains largely constant near zero regardless of viewing geometry.

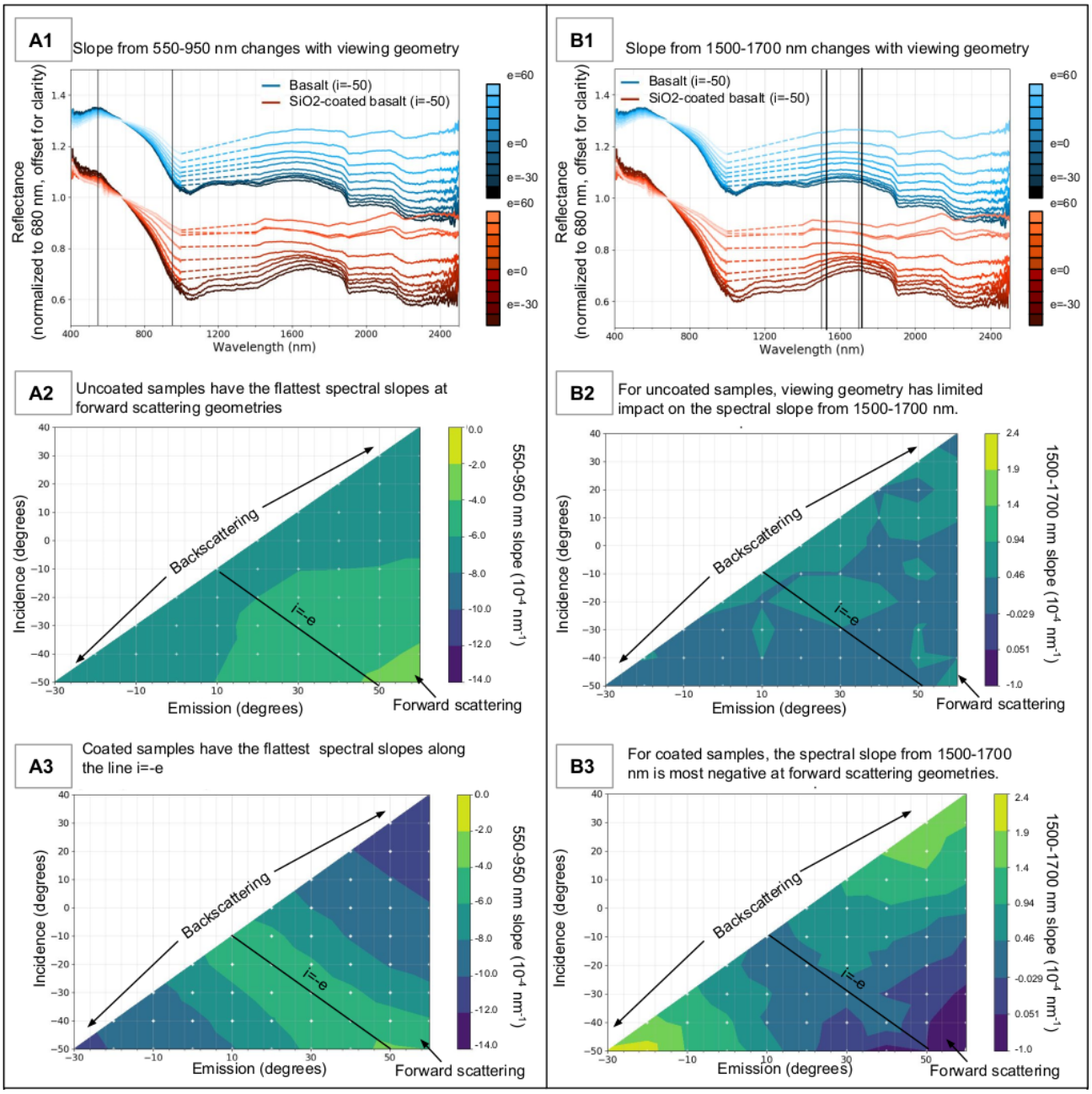

Figure 27: Spectrophotometry of basalt samples coated with a microns-thick layer of amorphous silica. Photometric behavior is examined for spectral slopes from 550-950 nm (A) and from 1500-1700 nm (B). Reflectance spectra collected at i=-50 and a range of emission angles and normalized to 680 nm (A.1, B.1) show the spectral slopes of interest changing with viewing geometry with black vertical lines marking shoulder locations. Heat maps show these slopes across a full goniometric sweep for uncoated (A.2, B.2) and coated (A.3, B.3) samples. Photometric effects are much more pronounced for the coated samples.

4.1.4 Spectroscopic and photometric effects of Fe-rich coatings

When measured at standard viewing geometries, spectra for coated and uncoated samples are similar at wavelengths longer than 720 nm. However, in visible wavelengths, they are distinguishable by the Fe^{3+} absorption at ~500 nm, which is significantly deeper for the coated sample than it is for the basalt interior (Figure 28A). Photometrically, the coated samples are slightly more specular than their unaltered counterparts, but the effect is far less pronounced than for pure silica coatings and the overall shape of the scattering lobe is closer to the unaltered interior than it is to the silica-coated sample (Figure 28B). Additionally, the spectral slope from 1500-1700 nm shows photometric behavior that is intermediate between the photometry of the interior and the photometry of silica-coated samples at those wavelengths (Figure 28C-D). The spectral slope from 550-950 nm, which was examined for the silica-coated samples, is masked by the Fe^{3+} absorption at 500 nm.

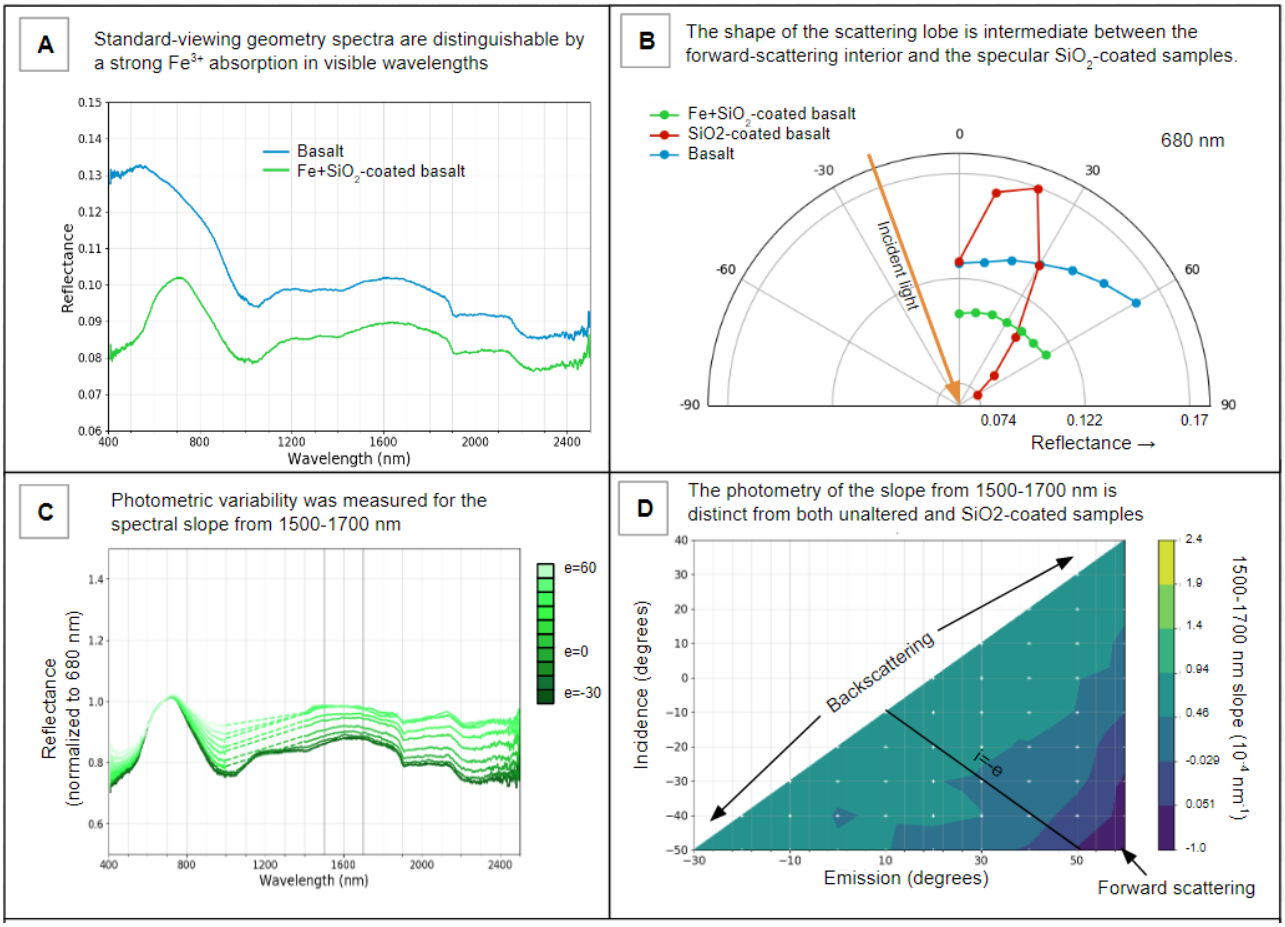

Figure 28: Spectrophotometry of samples coated with a mixture of silica and nanohematite. Standard geometry spectra (A) show that these samples have a diagnostic Fe^{3+} absorption in visible wavelengths. A polar plot with reflectance at 680 nm on the radial axis for incidence = -20 and varying emission angles (B) shows that samples with Fe-rich coatings have specularity intermediate between a basalt interior and an SiO_2-coated sample. Spectra for this same sample at i=-50 are shown normalized to 680 nm (C) to highlight changes in slope from 1500-1700 nm, and a heat map displaying values for this slope across a full goniometric sweep (D) shows that the slope is steepest at forward scattering geometries.

In addition to the trends described above, Fe-coated samples are found to show an overall negative spectral slope in the near infrared from 1700-2400 nm (Figure 29). This negative slope is steepest at backscattering geometries and closest to zero at forward scattering geometries.

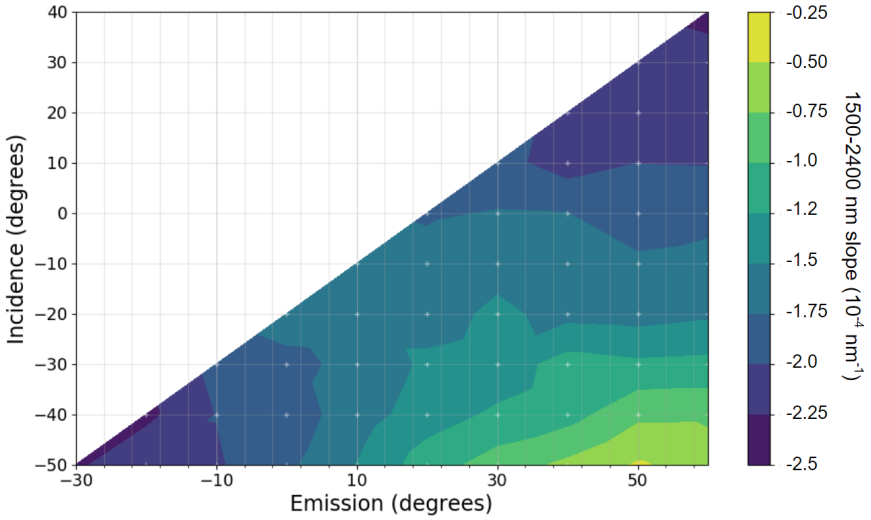

Figure 29: A heat map shows the spectral slope from 1500-2400 nm for a basalt sample with an Fe-rich coating. Slopes are least negative at forward scattering geometries.

4.2 Naturally-weathered surface results

4.2.1 Overview

Spectra collected at three viewing geometries from the nine Dry Falls samples and seven Frenchman Coulee samples show that the weathered surfaces display significant variation in spectral and photometric characteristics (Figure 30). Even within the same rock, strength and shape of absorption features varies from one surface to the next, and one surface may be backscattering while another is forward scattering. In hand sample, rocks range in appearance from dusky red and fairly smooth to pale yellowish brown and rough on the scale of medium sand-sized grains. Despite these differences, unifying features include key absorption features at ~500 nm (Fe^{3+} charge transfer), 1000 nm (Fe^{2+} crystal field effects), hydration bands around 1400 nm and 1900 nm, and a metal-OH stretch at ~2200 nm.

A: Dry Falls Basalt Exteriors

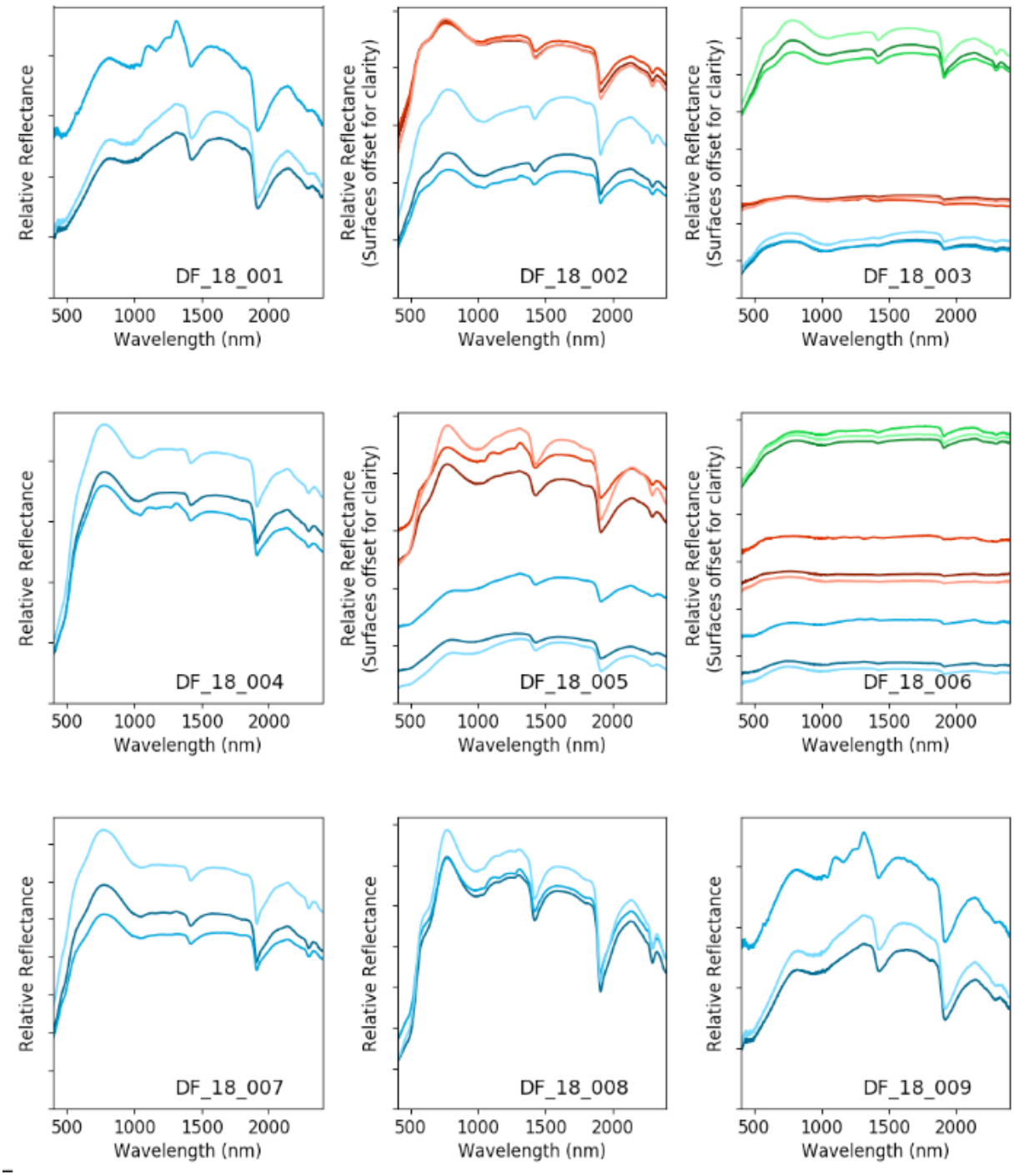

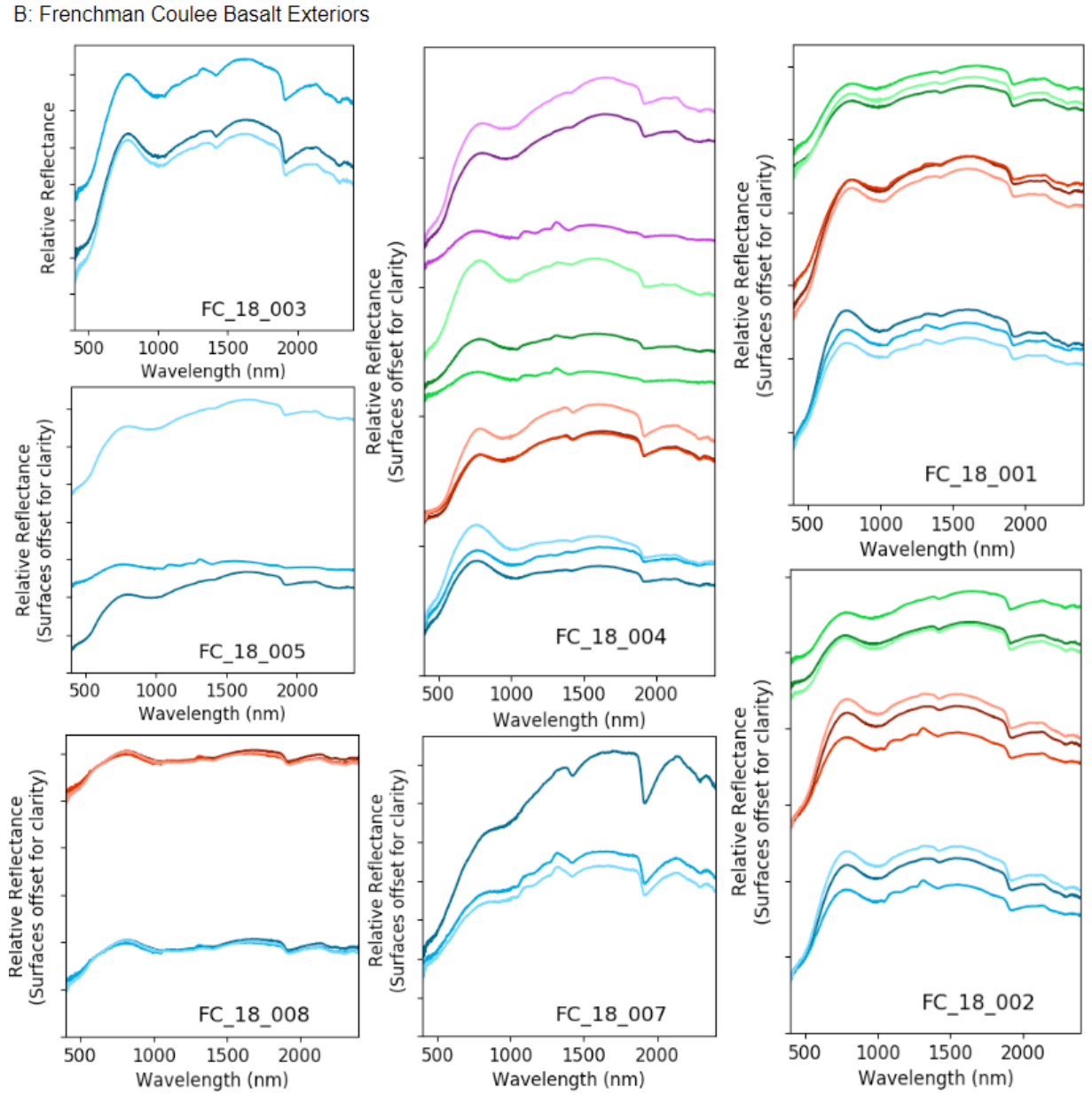

Figure 30: Spectra collected from the weathered exteriors of basalt samples from Dry Falls (A) and Frenchman Coulee (B) at three viewing geometries. Each plot shows data from a single rock with each hue (blue, red, green, or purple) representing a different area within that rock's surface. For a given hue, the darkest spectrum is the most backscattering (g=20 degrees), the medium spectrum is at a standard geometry (g=30 degrees) and the lightest is the most forward scattering (g=80 degrees).

From these samples, two were selected for detailed study - DF_18_003, which has a rind that is pale yellowish brown and backscattering (Figure 31A), and FC_18_004, which appears dusky red and is forward scattering (Figure 31B).

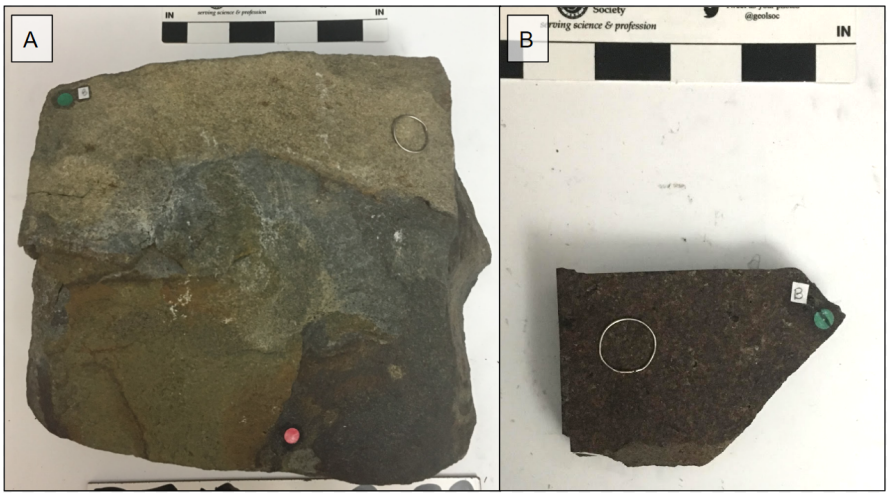

Figure 31: DF_18_003 (A) and FC_18_004 (B). These rocks represent two different types of weathering patterns seen in the sample suite, with DF_18_003 backscattering and DF_18_004 overall forward scattering. The metal ring marks the location on each rock where spectra were collected. Photo credit: Lena Gibbs.

4.2.2 DF_18_003 chemistry, mineralogy, and microtexture

The weathering rind of *DF_18_003* is found to be chemically and mineralogically similar to the interior. No new phases are observed and none are entirely removed with plagioclase, pyroxene, ilmenite, apatite, a felsic interstitial glass, and an altered mafic phase detected in both the interior and rind (Figure 32A, see Table 2 for chemical formulas). However, the rind is morphologically distinct with a notable increase in pore space and fracturing compared to the interior (detail in Figure 32B).

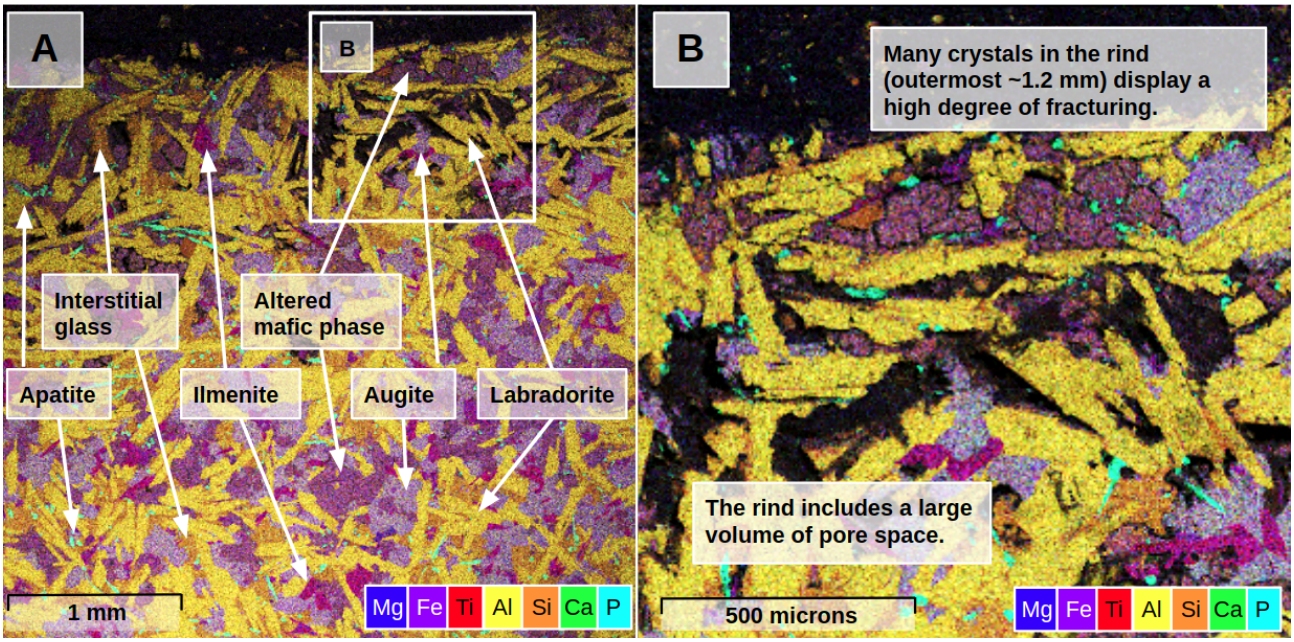

Figure 32: A cross-sectional image of DF_18_003 shows minimal change in chemistry and mineralogy but significant changes in morphology between the rock interior and its weathering rind. SEM EDS compositional data is here used to map rock components including plagioclase (yellow), pyroxene (light purple), ilmenite (magenta), apatite (cyan), interstitial glass (orange) and an altered mafic phase (dark purple).

Table 2: Compositional data for DF_18_003 acquired using SEM EDS.

	Plag	Aug	Ilm	Ap	Altered mafic phase (interior average)	Altered mafic phase (rind average)	Interstitial glass
Weight % oxide							
SiO_2	58.31	50.58	0	0	50.7	65.8	78.27
FeO	0	20.67	46.86	0	37.2	18	0
Al_2O_3	27.7	0	0	0	4.6	7.4	14.07
MgO	0	13.33	0	0	4	5.4	0
CaO	9.46	15.41	0	58.42	2.4	1.4	0
K_2O	0	0	0	0	0.6	1.3	7.66
Na_2O	4.53	0	0	0	0.4	0.6	0
TiO_2	0	0	53.14	0	0	0	0
P_2O_5	0	0	0	41.58	0	0	0
Total	100	99.99	100	100	99.9	99.9	100
Cation per formula unit							
# oxygen	**8**	**6**	**3**	**26**	**6**	**6**	**N/A**
Si	2.59	1.96	0	0	2.029	2.313	-
Fe	0	0.67	0.99	0	1.245	0.529	-
Al	1.45	0	0	0	0.217	0.307	-
Mg	0	0.77	0	0	0.239	0.283	-
Ca	0.45	0.64	0	10.81	0.103	0.053	-
K	0	0	0	0	0.031	0.058	-
Na	0.39	0	0	0	0.031	0.041	-
Ti	0	0	1.01	0	0	0	-
P	0	0	0	6.08	0	0	-
Cation sum	**4.88**	**4.04**	**2**	**16.89**	**3.895**	**3.584**	**-**

XRD data confirms that the interior and rind of *DF_18_003* are mineralogically similar with no new peaks appearing and none disappearing between the two spectra (Figure 33).

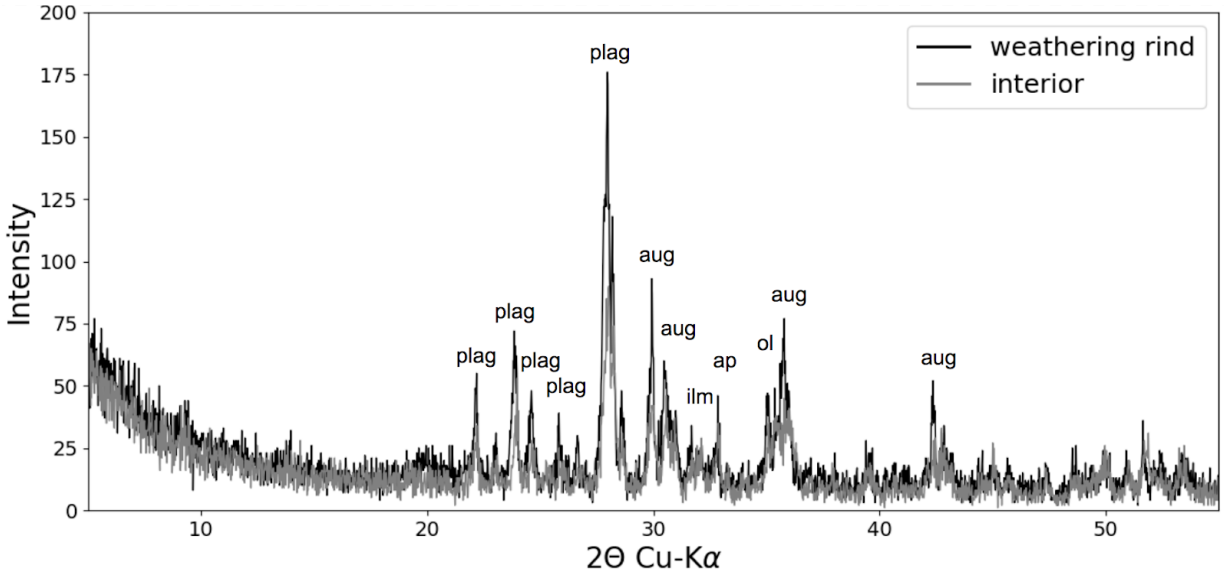

Figure 33: XRD data from powdered samples of the interior and weathering rind or DF_18_003 shows peaks consistent with labradorite, augite, iron-rich olivine, ilmenite, and apatite. In this data, there are no measurable changes in mineralogy from the interior to the rind.

However, XRD data for the isolated clay-sized (< 2 micron) fraction of DF_18_003 does show a difference in the prevalence of clay minerals in the rind as compared to the interior. These results show a significant peak at d=~14 angstroms (exact measurements varied from 13.1 to 14.5 angstroms) for the rind but only a very minor corresponding peak for the interior (Figure 34). Peaks in this range are typically associated with smectite and vermiculite clays.

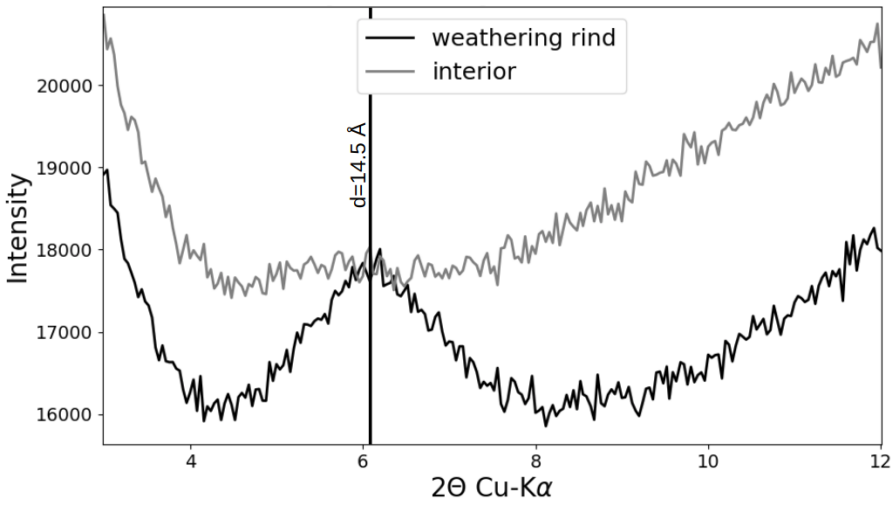

Figure 34: XRD data for the <2 micron size fraction for DF_18_003's interior (gray) and weathering rind (black).

After the isolated clay-size fraction of DF_18_003's rind was treated with ethylene glycol, the ~14 angstrom XRD peak (measured at 13.1 angstroms for this sample) shifted left to ~17 angstroms (Figure 35), which indicates that the clay in this sample is a 2:1 swelling clay.

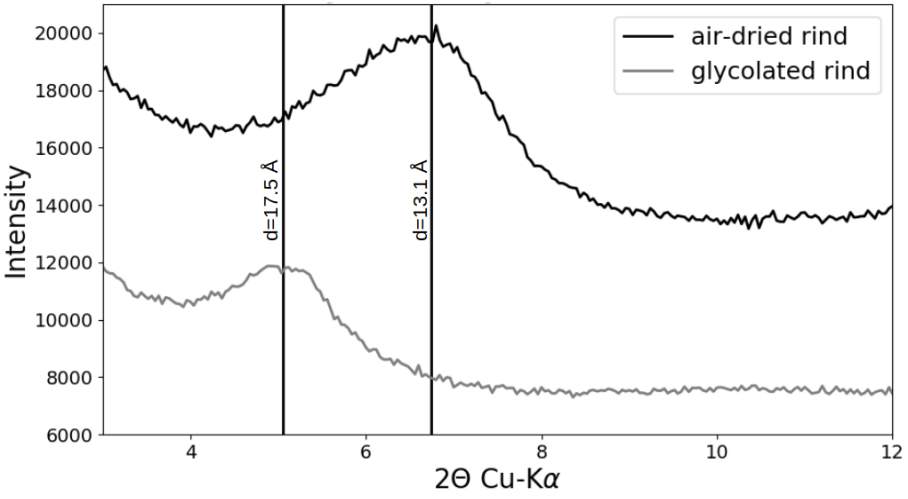

Figure 35: XRD data for the <2 micron size fraction for DF_18_003's weathering rind after air-drying (gray) and treatment with ethylene glycol (black).

In addition to this mineralogical change from interior to rind, chemistry was observed to change from the interior to the rind as well. In particular, the composition of the amorphous mafic phase

identified above was measured to change as a function of distance from the rock surface (Figure 36).

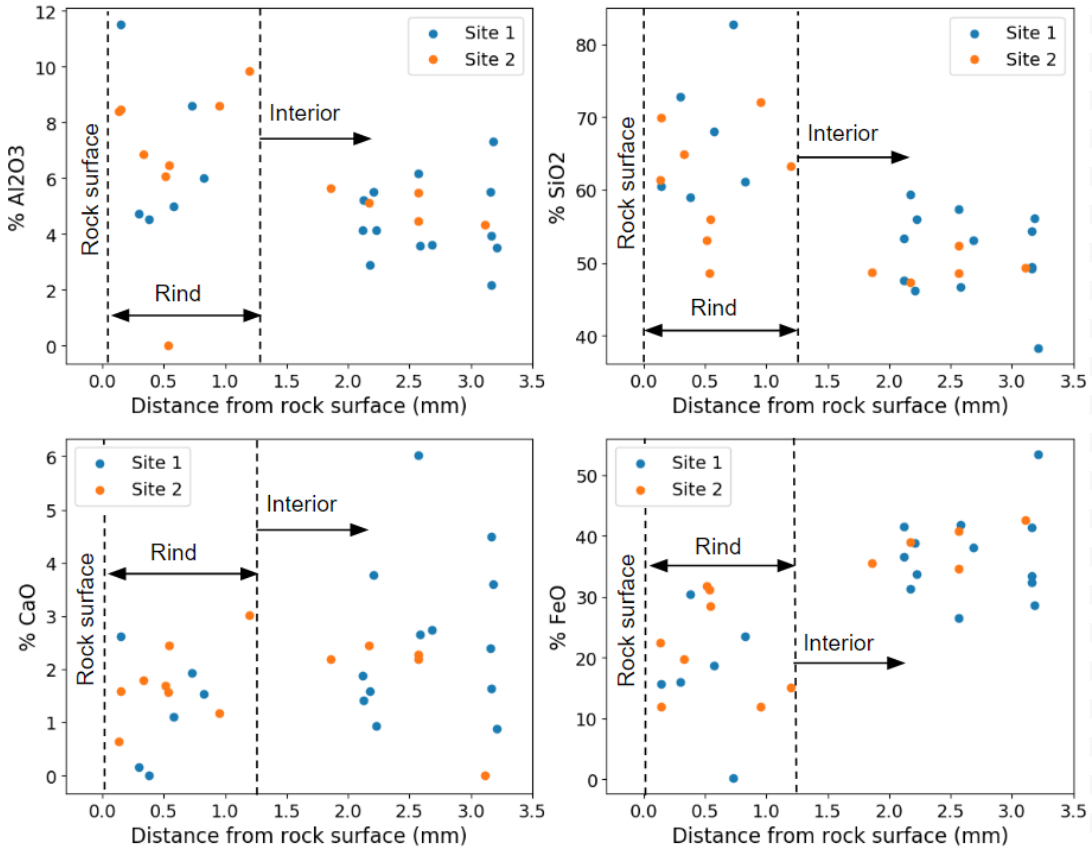

Figure 36: For the altered mafic phase identified above, weight % oxide is shown for Al_2O_3, SiO_2, CaO, and FeO as a function of distance from the rock surface. Compositional information was extracted from SEM EDS map data. When found in the weathering rind, crystals of this mafic phase are depleted in Fe and Ca and enriched in Al and Si compared to the same phase when found in the rock interior.

4.2.3 DF_18_003 photometry

Despite the pronounced mineralogical similarities between the rind and interior of *DF_18_003*, a photometric comparison shows significant weathering-induced changes (Figure 37). Spectra of the rock interior are forward scattering, with the highest reflectance occurring at the largest phase angle. The weathered exterior, however, is backscattering, with the highest reflectance occurring at the smallest phase angle.

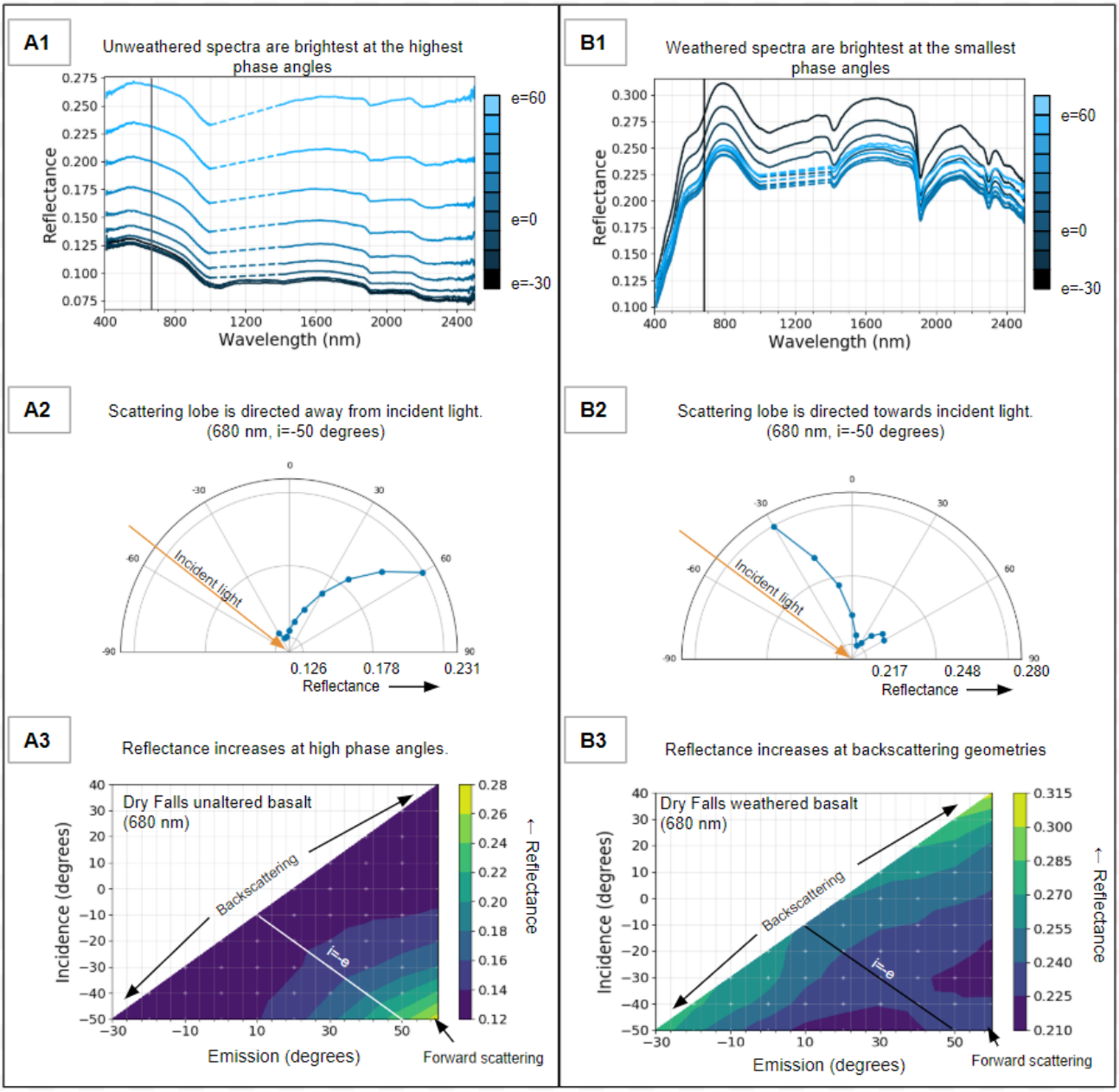

Figure 37: Spectrophotometry of the interior (A) and weathered exterior (B) of DF_18_003. Spectra taken at a fixed incidence angle of -50 degrees and varying emission angles show that the spectra of the interior are brightest at high phase angles (A1) whereas spectra of the exterior are brightest at small phase angles (B1). The shapes of the scattering lobes are shown in polar plots at a fixed wavelength (680 nm) in A2 (forward scattering) and B2 (backscattering). Heat maps show the same trends across a full goniometric sweep in A3 and B3.

4.2.4 FC_18_004 chemistry and mineralogy

SEM analysis of FC_18_004 also shows minimal change in chemistry from the interior to the surface (Figure 38A). Although morphological differences are not as pronounced as in DF_18_003, FC_18_004 does also display increased fracturing near the surface of the rock (Figure 38B).

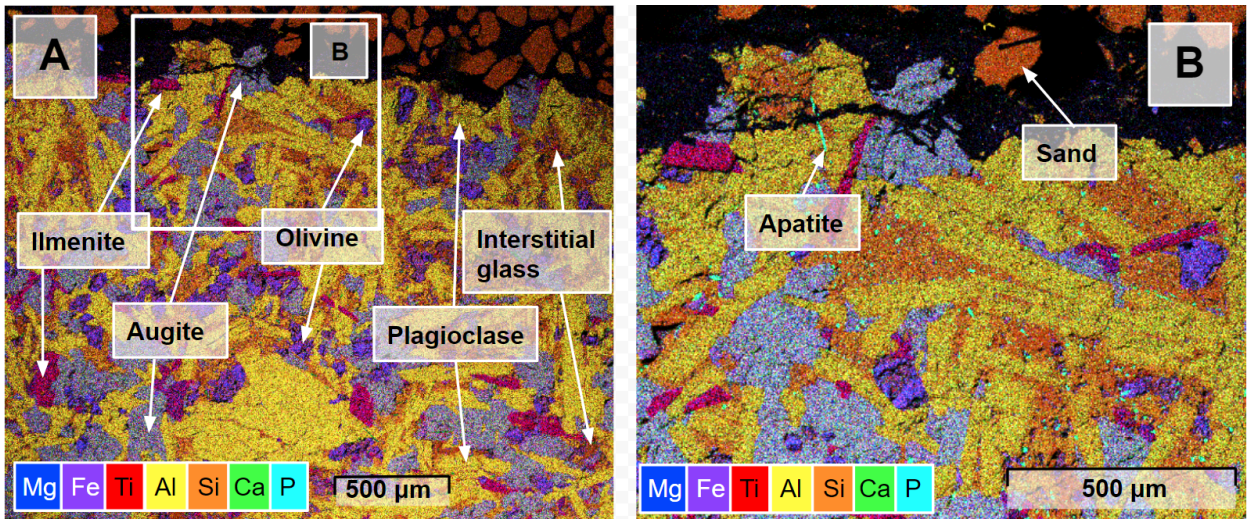

Figure 38: A cross-sectional image of FC_18_004 shows minimal change in chemistry and mineralogy between the rock interior and its weathering rind (A). Textural changes are less significant than for DF_18_003, but increased fracturing toward the surface is apparent in a detailed inset view (B). SEM EDS compositional data is here used to map rock components including plagioclase (yellow), pyroxene (light purple), ilmenite (magenta), interstitial glass (orange) and 10 micron scale apatite crystals (cyan). Quartz sand (orange) was embedded in the surrounding epoxy (black) to protect the sample during polishing. See Table 3 for detailed compositional data.

Table 3: Chemical data for FC_18_004 from SEM EDS.

	Plag	Aug	Olv	Titanium-rich oxide
Weight % oxide				
SiO_2	52.37	50.22	37.62	8.15
FeO	3.62	14.57	42.64	65.14
Al_2O_3	27.21	2.2	1.45	3.33
MgO	0.37	14.01	15.49	0.08
CaO	10.73	17.15	1.11	0.15
K_2O	0.75	0.14	0.21	0.15
Na_2O	4.55	0.3	0.34	0.07
TiO_2	0.33	1.2	0.88	19.09
P_2O_5	0.07	0.22	0.25	0.13
Total	100	100.01	99.99	96.29
Cation per formula unit				
# oxygen	**8**	**6**	**4**	**3**
Si	2.415	1.902	1.074	0.23
Fe	0.14	0.461	1.018	1.54
Al	1.479	0.098	0.049	0.111
Mg	0.025	0.791	0.659	0.003
Ca	0.53	0.696	0.034	0.005
K	0.044	0.007	0.008	0.005
Na	0.407	0.022	0.019	0.004
Ti	0.011	0.034	0.019	0.406
P	0.003	0.007	0.006	0.003
Cation sum	**5.054**	**4.018**	**2.886**	**2.307**

XRD data again confirms mineralogical similarities between the rind and interior with plagioclase, augite, olivine, and ilmenite accounting for the major peaks for both (Figure 39).

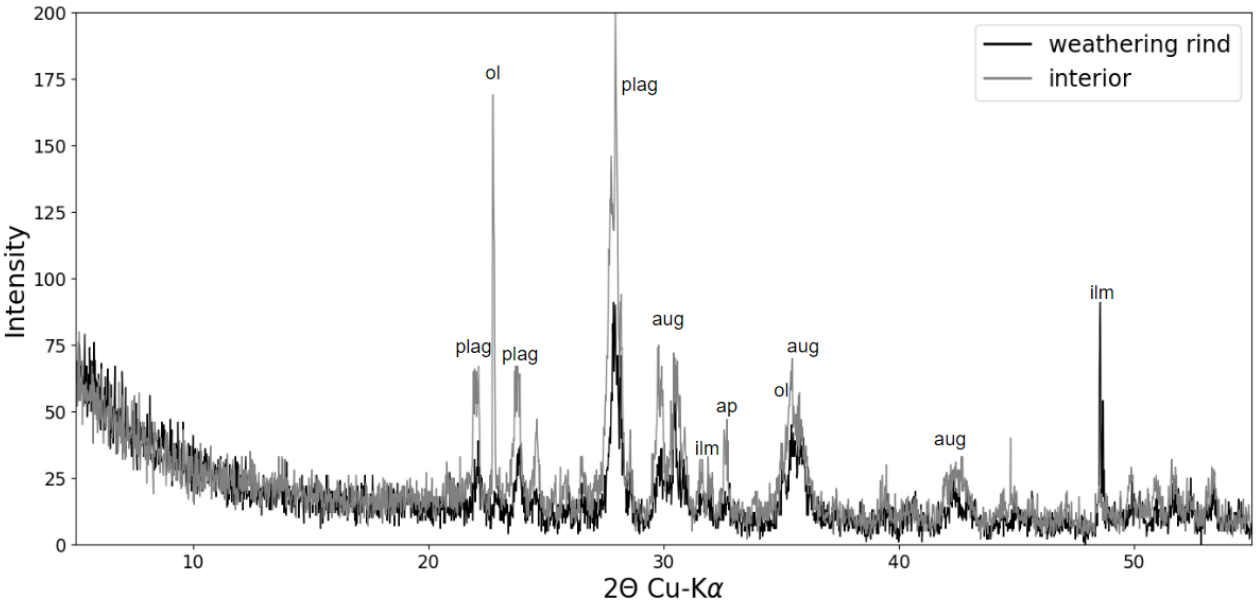

Figure 39: The interior of FC_18_004 is mineralogically similar to the weathering rind. The only measurable difference in XRD results is seen in the large peak at 22.7 degrees for the interior spectrum, which is small for the rind.

4.2.5 FC_18_004 photometry

Unlike DF_18_003, spectrophotometric data shows minimal influence of weathering on the photometric properties of FC_18_004. The rock interior scatters light into two distinct lobes, one backscattering and one forward scattering, with the forward scattering lobe slightly brighter than the backscattering lobe (Figure 40A). The weathered exterior is similar, with very little change in photometry (Figure 40B).

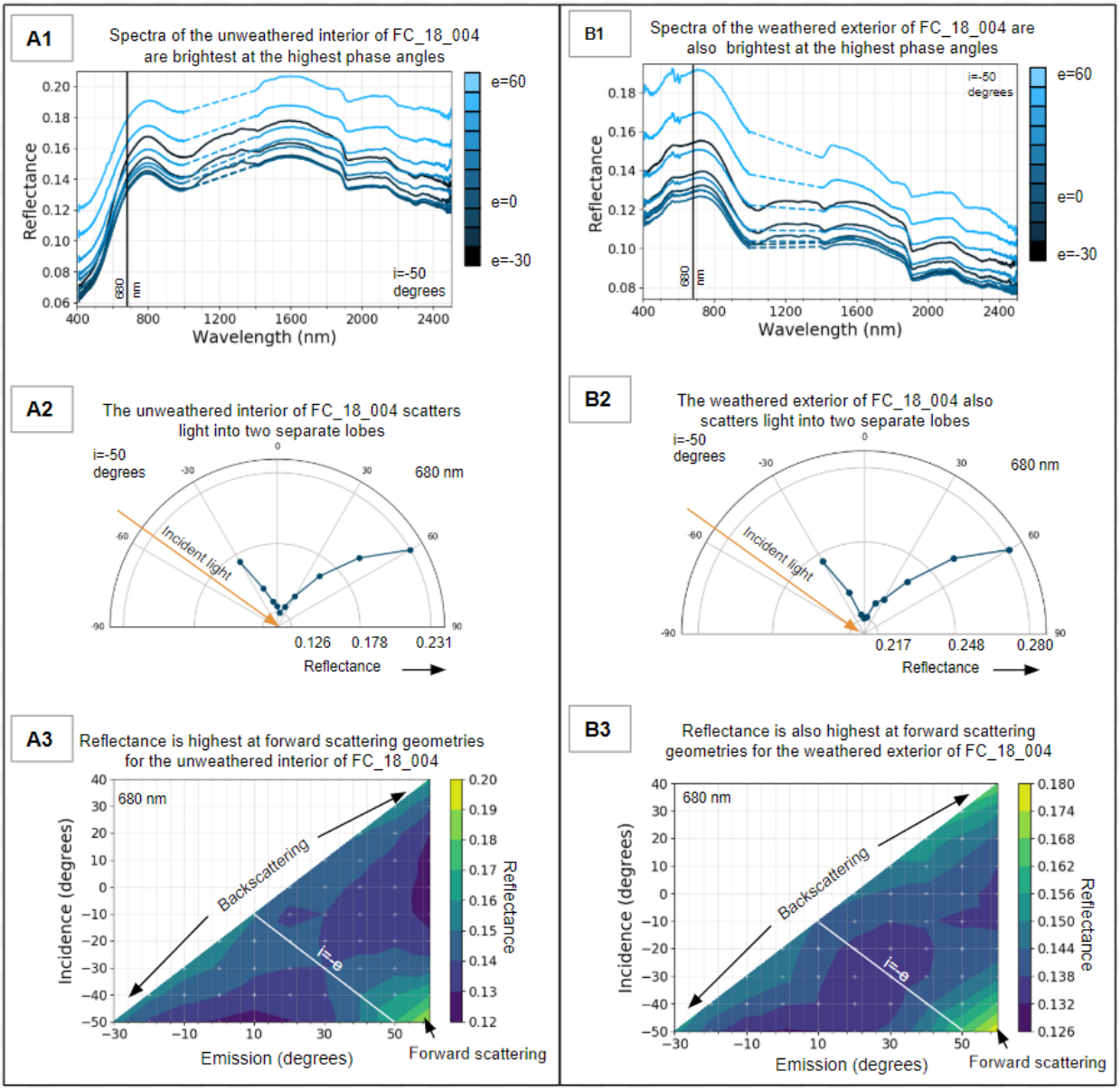

Figure 40: Spectrophotometry of the interior (A) and weathered exterior (B) of FC_18_004. Spectra taken at a fixed incidence angle of -50 degrees and varying emission angles show that the spectra of both the interior and exterior are brightest at high phase angles (A1, B1). The two-lobed shapes of both scattering lobes are shown in polar plots at a fixed wavelength (680 nm) in A2 and B2. Heat maps show the same trends across a full goniometric sweep in A3 and B3.

5. Discussion

5.1 Instrument characterization

5.1.1 Polarization artifacts in high phase angle measurements

One potential source of error in our photometric measurements comes from artifacts that ASD spectrometers have been shown to produce when data is collected at high phase angles (e.g. Buz 2017, Levesque and Dissanska, 2016). These peaks have been linked to polarization sensitivity of the instrument and can vary based on the orientation of the light source and detector head and the curvature of the cable as well as properties of the target material. In order to quantify the potential impact of these artifacts on our ability to measure photometric trends, we have used our spectrogoniometer system to characterize these artifacts for a suite of relevant materials .

Our results show that the size of these artifacts varies significantly from sample to sample and ranges from negligible (1% of signal, Figure 41A) to large (10% of signal, Figure 41B). These differences presumably stem from compositional and physical properties of these samples that influence how their surfaces change the polarization of incident light relative to how a Spectralon® white reference panel changes the polarization of incident light.

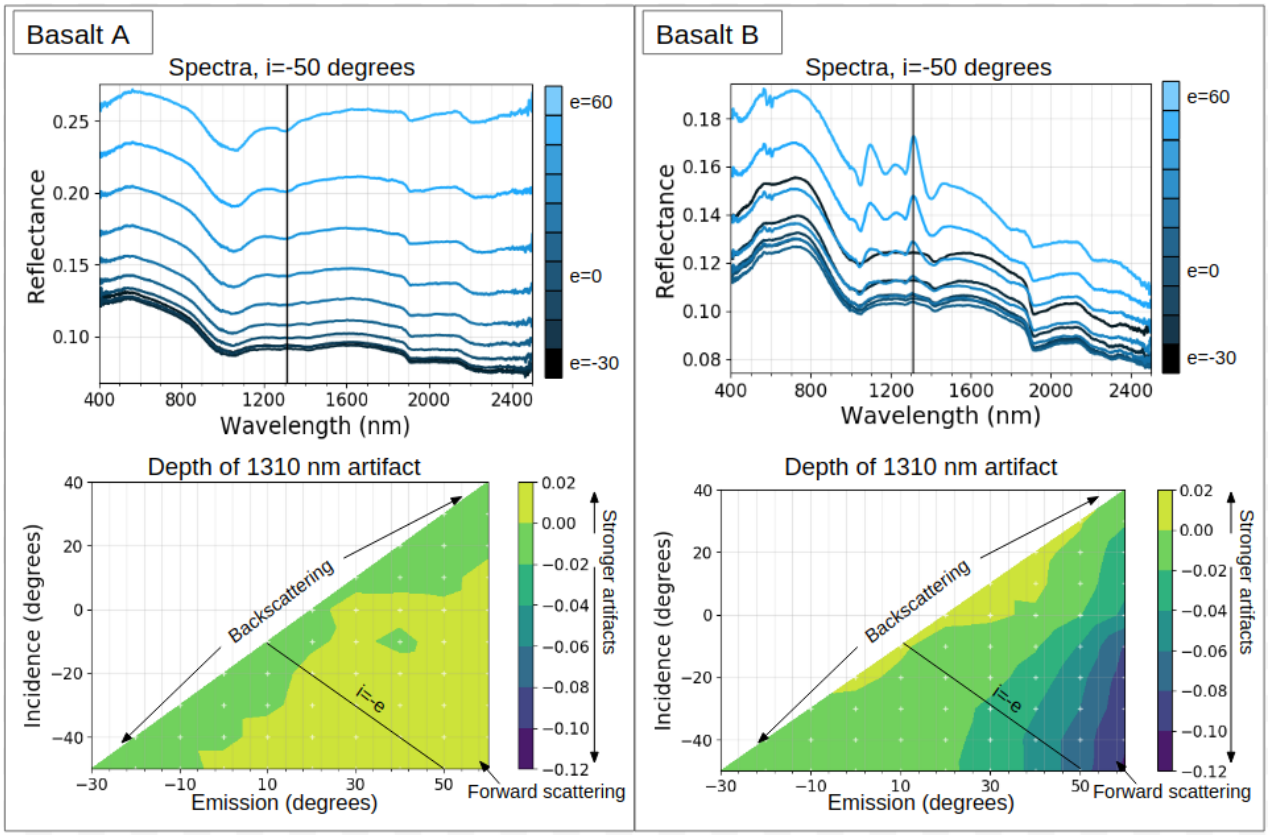

Figure 41: Band depth for the artifact at 1310 nm was measured using shoulders placed at 1270 and 1360 nm. Artifacts are small (~1%) for Basalt A at all viewing geometries, although they still begin to be significant at high phase angles. Basalt B, which appears similar at low phase angles, shows large negative-depth artifacts beginning at moderate phase angles. High phase angle spectra for Basalt B also show noisy behavior around 500 nm, whereas Basalt A spectra do not. While analysis of the 1100 nm artifact is not shown here, its behavior is similar.

Using our worst-case samples, we proceeded to quantify the depth of the artifacts in the most problematic wavelengths (centered around 1100 and 1310 nm) at different viewing geometries. As has been previously documented, these artifacts become more prevalent with increasing phase angle. Defining phase angle *g* as emission angle - incidence angle, we identified a 'safe zone' from *g*=-20 degrees to g=40 degrees where the height of the artifacts is never more than 0.1% relative to our Spectralon® white reference, even for the worst-case samples (Figure 42). To minimize error introduced into our science analyses, we opted to either use wavelengths that are not impacted by the 1100 nm and 1310 nm artifacts, or to look only at phase angles where artifacts are always small.

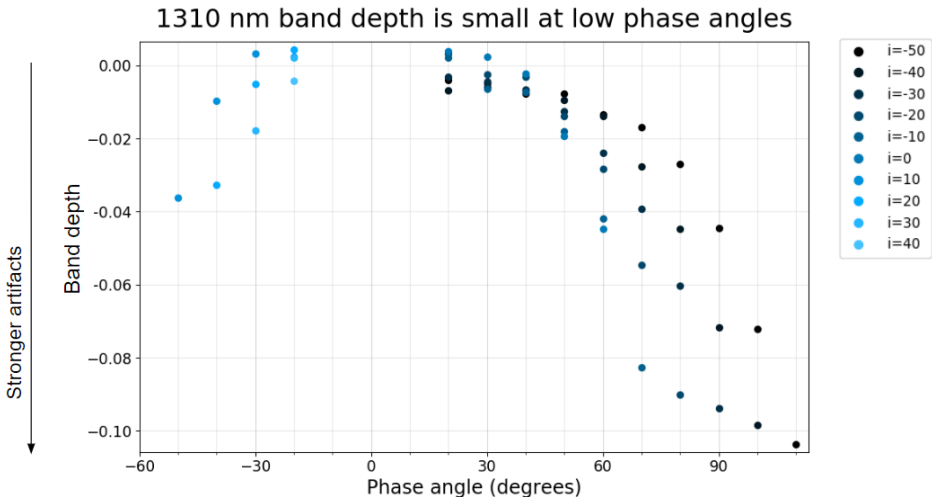

Figure 42: 1310 nm artifact band depth is plotted for basalt B as a function of phase angle. Even though this sample is prone to large artifacts, low phase angle measurements (-20 degrees to 40 degrees) do not show significant polarization artifacts. Band depth was measured using shoulders at 1270 and 1360 nm.

5.1.2 Helmholtz reciprocity

Helmholtz reciprocity states that reflectance at some emission and incidence angle should be the same if the positions of the detector and light source are switched, or in other words, R(i,e)=R(e,i). This axiom is known to hold for a wide variety of surfaces, but it is only valid if either a) incident and detected light are both unpolarized or b) incident and detected light have corresponding polarizations (e.g. Clark and Parry, 1985).

5.1.2.1 Non-reciprocity of surfaces as measured by WWU's spectrogoniometer

WWU's spectrogoniometer is designed to approximate the first situation (unpolarized light source, detector not sensitive to polarization), but we are aware that this is not strictly the case, as documented in section *5.1 Polarization Artifacts*. As a step toward quantifying other potential polarization effects, we quantified non-reciprocity as the percent difference between two reciprocal-geometry measurements for a variety of surfaces. Our findings indicate that while

reciprocity does hold true for some of our observations (e.g. Figure 43), there are particular samples (basalt with thin silica coatings, or glass cover slips on dark substrates, or some weathered basalt samples) that consistently show very significant non-reciprocal behavior when observed using our system (Figure 43).

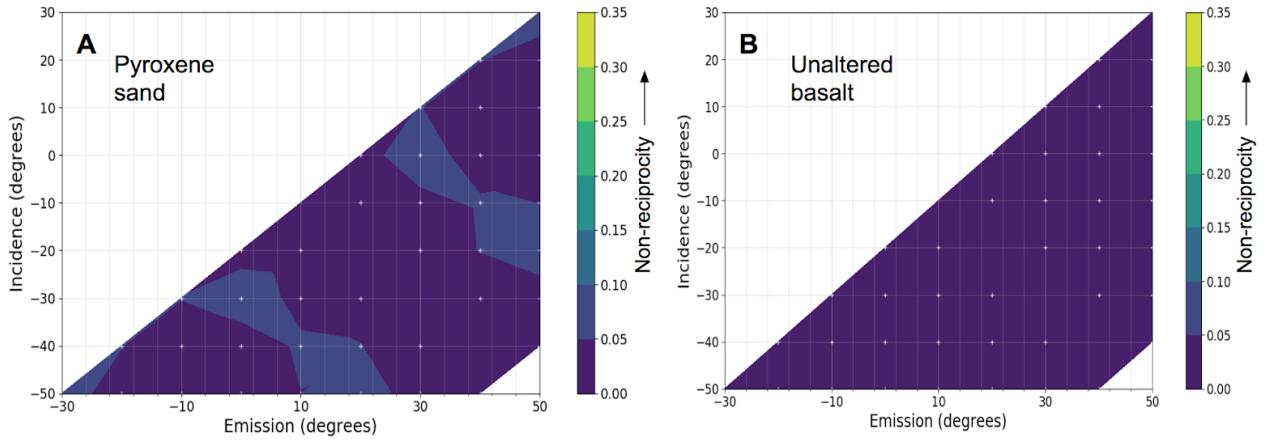

Figure 43: Non-reciprocity (percent change in reflectance between reciprocal measurements) for pyroxene sand (A) and unaltered basalt (B). Differences in reciprocal measurements are within the noise of the system, which has been measured to be ~.01 relative to a Spectralon white reference panel or about 5-10% relative to these dark samples. Note that these measurements are symmetrical about the line i=-e by definition, because non-reciprocity is calculated as the magnitude of the difference between R(i,e) and R(-e, -i). Non-reciprocity is measured at 680 nm.

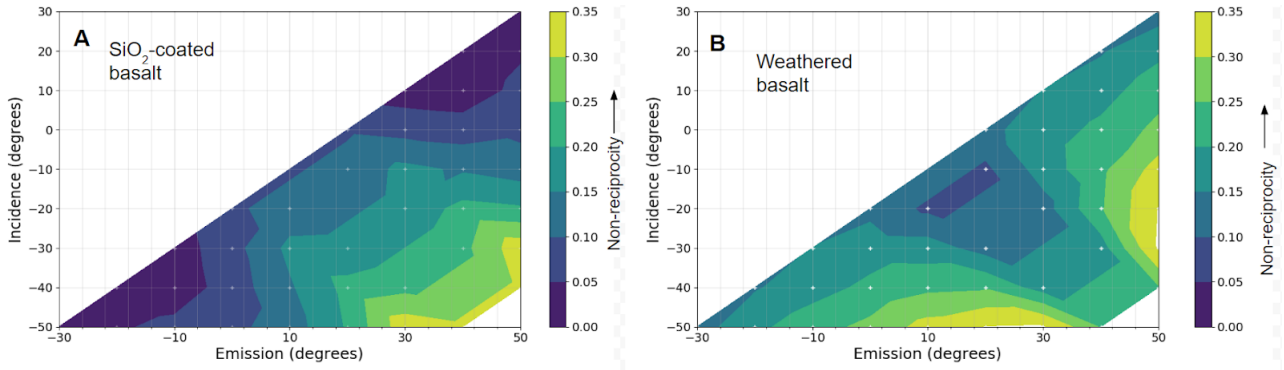

Figure 44: Non-reciprocity (percent change in reflectance between reciprocal measurements) for this basalt coated with amorphous SiO2 (A), and a naturally-weathered basalt (B). Differences in reciprocal measurements are very significant, up to ~35% of the signal. Non-reciprocity is measured at 680 nm.

We hypothesize that these non-reciprocal measurements, like the artifacts described above, may be caused by material-specific effects related to interactions with polarized incident light and/or the polarization sensitivity of the detector. The credibility of this hypothesis is supported

by a comparison with observations by Clark and Parry (1985) in their study of reciprocity and polarization. They quantified differences in reciprocal measurements for a system with the detector and light source in various combinations of polarization including unpolarized, polarized in the same plane, and cross-polarized, and our results for samples with synthetic silica coatings have a similar degree of non-reciprocity (~10%) as their findings for a system measuring reflectance of polished opal with one beam polarized and the other unpolarized (Table 4). This scenario likely does not constitute a perfect analog for WWU's spectrogoniometer because both our detector and our light source are likely partially polarized rather than one being fully polarized and the other unpolarized. However, it is a useful approximation and lends credence to the idea that polarization effects may be impacting our photometric measurements in subtle ways.

Table 4: Clarke and Parry measured bidirectional radiance factors β(i, e) for polished opal at reciprocal geometries using an instrument with one beam polarized and the other unpolarized. In this case, their results showed changes on the order of 10% between reciprocal measurements.

	$\frac{\beta(0_s, 57_r)}{\beta(57_s, 0_r)}$	$\frac{\beta(0_p, 57_r)}{\beta(57_p, 0_r)}$	$\frac{\beta(0_r, 57_s)}{\beta(57_r, 0_s)}$	$\frac{\beta(0_r, 57_p)}{\beta(57_r, 0_p)}$
Polished MS14 opal	1.100	0.924	0.917	1.092
Polished MS20 opal	1.092	0.923	0.917	1.085

Furthermore, because the work done by Clark and Parry (1985) shows that polarization of the light source can have a significant impact on measured reflectance even for a system with a detector not sensitive to polarization, these results highlight the importance of taking polarization effects into account when interpreting spectra collected by spacecraft, which may collect data under a range of polarization conditions. In the future, to develop a fully robust library of photometric data, analog measurements should be taken with an unpolarized detector under a range of light source polarization conditions. This will enable future researchers to determine which photometric properties persist under any realistic natural lighting scenario and which

require contextual information about the polarization of incident light in order to make confident interpretations.

5.1.2.2 Non-reciprocity of published Spectralon® reflectance values

Published photometric data on the bi-directional reflectance distribution function (BRDF) of Spectralon® was used to calibrate WWU's spectrogoniometer system as described in *3.1.3 Goniometer system calibration*. The data that the calibration process relies on was extracted from Biliouris et al., 2007 and was collected using a system reported to have an unpolarized light source and unpolarized detector. This has two implications. First, there may be discrepancies between Spectralon®'s published BRDF and Spectralon®'s BRDF under our system, which does not have a perfectly unpolarized light source or detector, and this may introduce error into our calibration algorithm. Second, for a system with an unpolarized light source and detector, Helmholtz reciprocity should hold, and we can test whether the published values are reciprocal as a check on the validity of the work. We have done this check and found that there is significant non-reciprocity in the published measurements (Figure 43). We are therefore cautious regarding the precision of the published dataset and suspect that this might introduce error of up to 4.2% into our calibrated measurements even if our light source and detector were perfectly unpolarized.

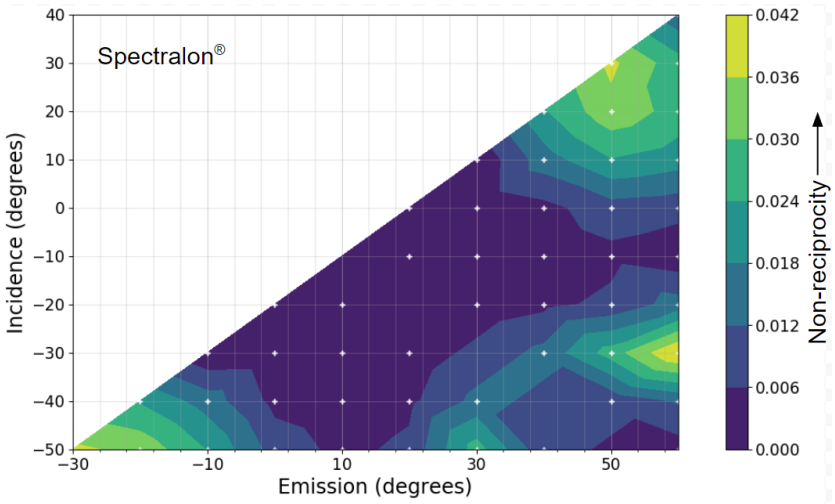

Figure 45: Differences in reciprocal measurements for published data on the BRDF of Spectralon®. Within the range used by our instrument, reflectance may vary from a measurement to its reciprocal measurement by upwards of 4%.

5.2 Science implications

5.2.1 Synthetically coated basalt photometry

5.2.1.1 Silica coatings

Spectra of coated and uncoated samples taken at standard viewing geometries were found to be similar enough that rock coatings like this would likely be overlooked by spacecraft if photometric effects were not considered. But, when observed at a range of viewing geometries, multiple distinctive trends including increased specularity and changing slopes from 550-950 nm and 1500-1700 nm provide examples of the photometric characteristics that may prove to be a robust means of differentiating between coated and uncoated rocks. And, because identification of these photometric parameters as regions of interest relied on visual inspection, additional diagnostic features may exist as well that have not yet been described. One example of a site where this method could be applied is the Pathfinder landing site, where amorphous silica coatings have been hypothesized to exist. Specular reflection has already been observed for

these martian rocks, so our work strengthens the case for silica coatings in this area. If additional spectrophotometric measurements could be made to determine whether the 550-950 nm and 1500-1700 nm slopes correlate to our synthetic coatings as well, it would further increase the credibility of the interpretation of the Pathfinder landing site rocks as coated with amorphous silica. However, because this project focused on samples with synthetic pure silica coatings, we have not accounted for the variability that may be induced by chemical impurities and other complexities that can be associated with natural coatings. Further investigation of natural silica-rich coatings will be required to verify whether the photometric trends we observed will hold for a representative suite of silica-coated rocks, or whether they are limited to our very simple samples.

5.2.1.2 Fe-rich coatings

Unlike pure silica coatings, coatings that include nanohematite create measurable differences in spectra even at standard geometries and are therefore unlikely to be completely overlooked. However, photometric trends could still provide an important means of differentiating between different types of Fe-rich coatings. Our results show that the coatings we applied, which consist of a mixture of amorphous silica and nanohematite, induce photometric properties that are intermediate between those of uncoated rocks and those of rocks with pure silica coatings. This indicates that the photometry of Fe-coated rocks may be dominated by other components of the coatings even though standard viewing geometry spectra are primarily influenced by Fe^{3+} absorptions. To confirm this hypothesis, more work should be done on a wider variety of Fe-rich coatings.

The observed negative slope in the near infrared from 1700-2400 nm for basalt samples with Fe-rich coatings correlates with observations by Johnson and Grundy (2001). And, as found by Fischer and Pieters (1993), the slope is most negative at small phase angles and most positive at high phase angles. In these previous studies, the negative slope was hypothesized to result from longer wavelengths penetrating to the darker substrate while shorter wavelengths bounced off the brighter coating. This interpretation also provides a plausible explanation for the observed photometric behavior, because at high phase angles, the increased light-coating interaction path length might prevent the incident light from penetrating to the dark substrate even at longer wavelengths. While this is a compelling explanation for the results of these previous studies, a challenge arises in applying the same interpretation to our results due to the comparative brightness of our uncoated samples. Because our uncoated samples are bright relative to our coated samples, we would expect that 'seeing through' the coating would lead to an *increase* in reflectance and a *positive* slope in the near infrared. However, because the uncoated surface brightness is influenced by roughness, which is influenced by the application of a coating, it remains possible that an increased relative contribution from the substrate material is a factor in the darkening of our spectra at longer wavelengths.

One factor that may limit the relevance of our Fe-rich coatings is the uneven distribution of Fe_2O_3 within the coatings. SEM analysis shows the nanohematite aggregates into clusters on the 100 micron scale. This clumpiness is morphologically different from the thin sheets of Fe-rich material observed within silica coatings on Earth (e.g. Figure 3) and these differences may influence spectroscopic and/or photometric characteristics of the resulting coating.

5.2.2 Naturally-weathered surface photometry, mineralogy, and chemistry

5.2.2.1 Photometry and spectroscopy of broad sample suite

The high degree of variability in the spectral and photometric characteristics of weathered basalts from the same or similar study sites indicates that relatively minor changes in weathering environment can lead to major changes in photometry. This adds complexity to analysis and precludes the identification of any one diagnostic weathering effect on photometry or spectroscopy, but also creates potential for specific interpretations about weathering environment to be made based on those photometric changes.

The positive correlation between near-infrared slope (measured from 1700-2400 nm) and phase angle that was observed for most (but not all) weathered surfaces is consistent with findings by Fischer and Pieters (1993) for basalt with ferric coatings. Based on SEM results showing iron oxides on weathered surfaces, and spectral results showing that the unaltered substrate is darker than the weathered exterior for FC_18_004, this correlation is interpreted to arise from the same causes previously identified - coatings become transparent at long wavelengths, and the darker substrate contributes more to the signal, but this effect is minimal at high phase angles where the light-coating interaction path length is maximized.

5.2.2.2 Photometry of DF_18_003 and links to mineralogy, chemistry, and morphology

The overall backscattering behavior of DF_18_003's weathered surface is interpreted to arise primarily from the morphological change from low pore space and fracturing in the interior to very high pore space and fracturing of the rind. This is consistent with photometric theory which holds that surface roughness, which is increased along with pore space and fracturing, can contribute to backscattering behavior (e.g. Ladouceur and Poladian, 1996).

One interesting feature of the photometry of DF_18_003 is the small secondary peak in reflectance at high phase angles (see Figure 37). This second peak in reflectance may be interpreted as a specular peak, or it may be related to a different material property. Regardless, it is interesting to note the similarity of these values to the photometry of backscattering materials at the Pathfinder Landing site (Figure 44). This is a comparison to soil rather than rock, but the similarity is not surprising given the highly porous and fractured nature of DF_18_003's rind.

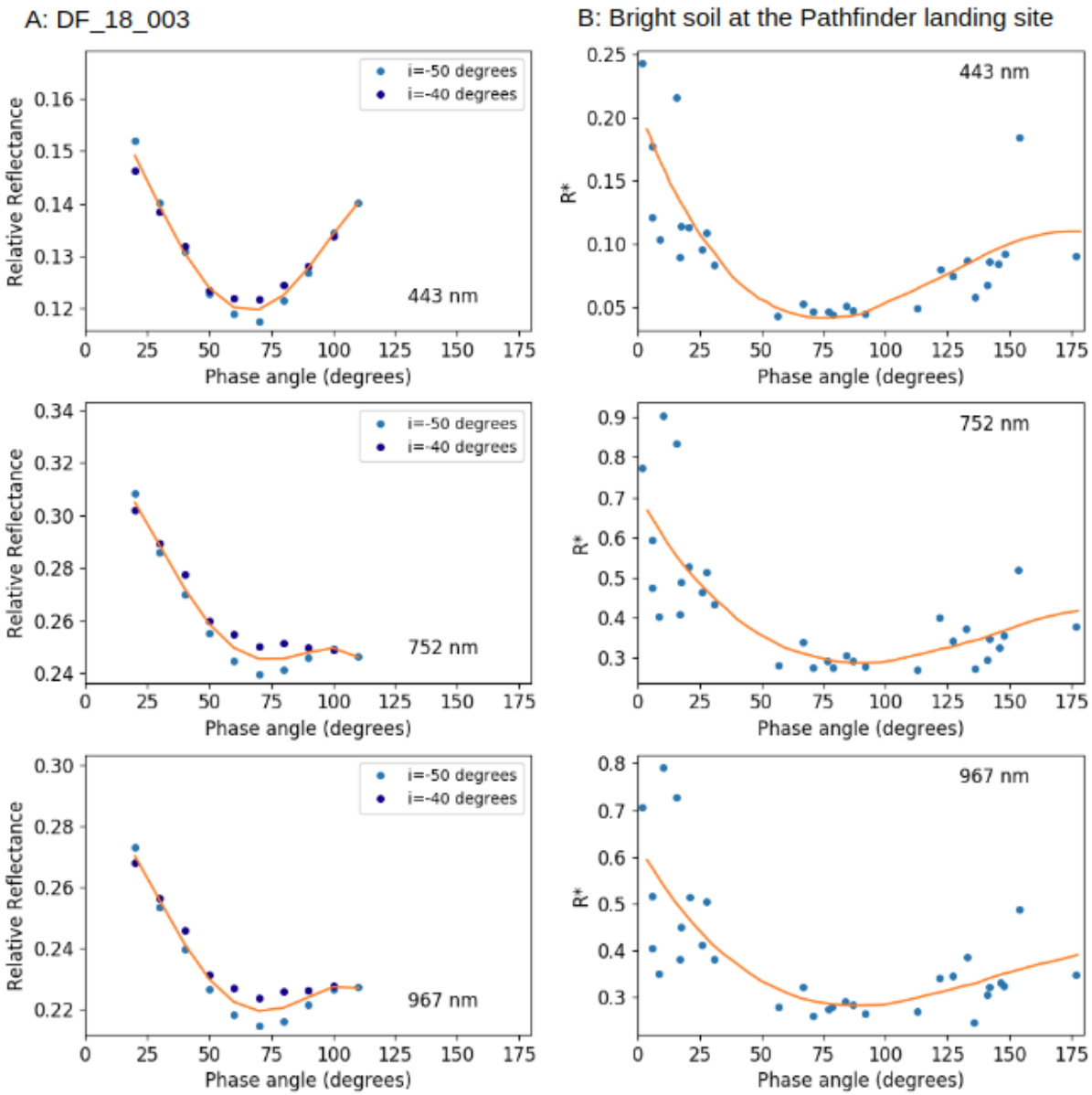

Figure 46: Reflectance as a function of phase angle for DF_18_003 (A) as compared to reflectance as a function of phase angle for bright soil at the Pathfinder landing site (B (data from Johnson et al., 1999)). Both are overall backscattering but both display a secondary peak in reflectance at forward scattering geometries. *R** is defined as reflectance relative to Pathfinder's onboard calibration targets.

Although the mineralogy and chemistry of DF_18_003 are found to be largely unchanged from the rock interior to the weathering rind, minor differences were observed in both chemistry and mineralogy. For example, although neither the interior nor the weathering rind of DF_18_003 was found to contain enough clay to create any measurable XRD peaks when the bulk

composition was analyzed, isolating the clay-sized fraction of each did enable the detection of clay signatures in XRD data. For the weathered exterior, the combination of a strong peak at ~14 angstroms for an air-dried sample and a corresponding peak at ~17 angstroms in a sample treated with ethylene glycol indicates the presence of a 2:1 swelling clay, likely a smectite although possibly vermiculite (Poppe et al., 2002). The interior of the rock shows the same ~14 angstrom peak, although it is much weaker than the peak for the weathered sample (see Figure 34). This suggests that the clay in the interior has the same mineralogy as the clay in the exterior, but is present only in very small amounts. This is consistent with the interpretation that most clays in these rocks formed as weathering processes, which primarily affect rocks' exposed surfaces, altered Al-rich primary igneous minerals to form clays. However, other viable clay-formation mechanisms do exist (e.g. deuteric alteration). And, it should also be noted that even for the rind, the absence of clay signatures in the bulk composition XRD data indicates that clays are only very minor constituents of these materials.

Additionally, within crystals of the altered mafic phase identified throughout the rock, chemical trends show Fe decreasing in concentration while Al increases. This is somewhat unexpected, as Fe tends to be a refractory constituent of most rocks, and might be explained by microfractures filling with clays rather than Fe being lost to the environment.

5.2.2.3 Photometry of FC_18_004 and links to mineralogy and morphology

Results from FC_18_004 support the hypothesis that the shape of a scattering lobe is closely linked to rock texture. Unlike DF_18_003, FC_18_004 remains largely intact from the rind to the exterior (although some fracturing is apparent), and this likely accounts for the photometric similarity between the interior and rind.

Like DF_18_003, this rock's reflectance seems to be split into a forward scattering lobe and a backscattering lobe. While there are many different factors that may be influencing this, there is again a noteworthy similarity to the photometry of martian materials, in this case to gray rocks at both the Pathfinder landing site and Gusev Crater (Figure 47). These gray rocks are of unknown composition but have been interpreted as dust-free, have likely experienced some degree of weathering (Johnson et al., 1999, Johnson et al., 2006) and are likely basaltic base on geologic context (e.g. Morris et al., 2006). There are significant differences in the two materials' photometry, for example FC_18_004 is more forward scattering than either of the martian rock types. But, the similar shape with relatively high reflectance at high and low phase angles with a minimum at moderate phase angles may be representative of some types of weathered martian rock and provides support for the continued use of these CRBs as martian analogs for photometric studies.

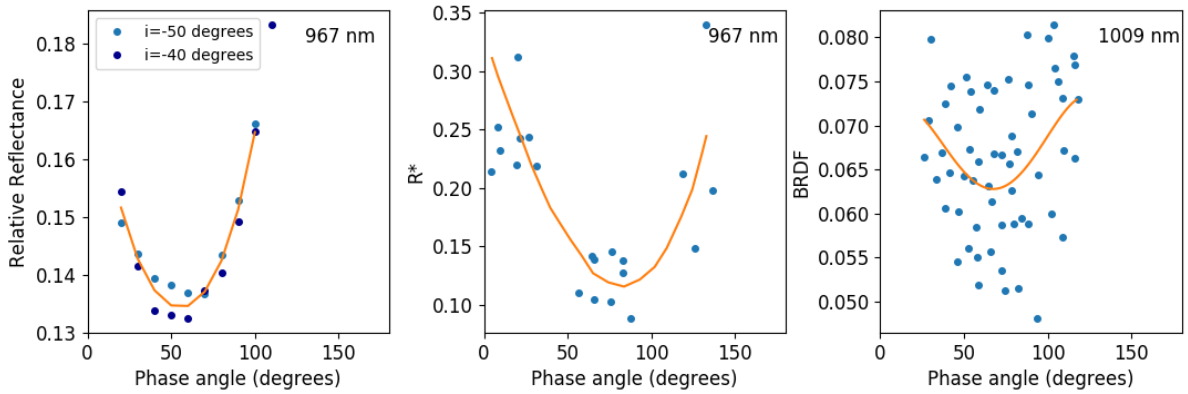

Figure 47: Reflectance as a function of phase angle for FC_18_004 (A) as compared to reflectance as a function of phase angle for gray rocks at the Pathfinder landing site (B. Data extracted from Johnson et al. 1999) and gray rocks in Gusev Crater (C. Data extracted from Johnson et al. 2006). Data is shown in blue and polynomial best fits are in orange. *R** is defined as reflectance relative to Pathfinder's onboard calibration targets. BRDF is the Bi-directional Reflectance Distribution Function value as defined in Hapke (1981). In all three cases, reflectance shows a distinctive two-lobed behavior with high reflectance at both forward and backscattering geometries.

Like DF_18_003, FC_18_004 is mineralogically and chemically similar from the interior to the weathering rind. XRD results do show olivine peaks for the interior spectra that are not present in the spectra for the rind. However, especially in light of SEM images that clearly show olivine crystals in the weathering rind of FC_18_004, the absence of XRD evidence for olivine in the rind is interpreted to be the result of imperfect sample preparation rather than an indicator of a true mineralogical change. This could arise from differences in the way the interior and exterior samples were powdered. The ball mill used to crush the interior sample would almost certainly have crushed all the sample to a uniform powder. The rotary tool used to separate weathering rind material, on the other hand, could have failed to fully powder some components. If olivine crystals were present but were not powdered, they might only have been measured in a few orientations, which would lead to the absence of some expected olivine peaks in the resulting spectra.

5.2.3 Relevance to spacecraft operations

Two key instruments for martian spectroscopy are the Compact Reconnaissance Imaging Spectrometer for Mars (CRISM) onboard NASA's Mars Reconnaissance Orbiter (MRO) and the Mastcam multispectral imager on the Curiosity Rover, both of which are currently being used to investigate the martian surface. CRISM has spectral resolution and range similar to the ASD reflectance spectrometer used for this study (Murchie et. al., 2007) so we can have reasonable confidence that the trends described here would be detectable using CRISM. However, as an orbiting instrument, CRISM does not have the spatial resolution needed to characterize individual rocks as was done for this study. Mastcam does have high spatial resolution, but the spectral resolution and range are significantly reduced compared to WWU's instrument (Malin et al., 2010), and it is not obvious whether Curiosity would be able to detect the photometric trends

identified in this project or not. In this section, we consider 1) whether Mastcam would be capable of detecting the photometric trends described in this study and 2) how photometric observations of rinds and coatings might be integrated into both tactical and strategic spacecraft operations planning.

5.2.3.2 Detectability of photometric trends using Mastcam

The Mastcam instrument uses a set of 12 filters set at carefully chosen wavelengths to piece together spectra that are very useful for measuring martian mineralogy despite limited range and resolution (Malin et al., 2007). Using bandpass data from Bell et al., 2018, the spectra collected for this study were convolved to these Mastcam filter positions, resulting in a dataset that is the equivalent of what the Curiosity rover would see if it were to observe our samples on Mars (Figure 48).

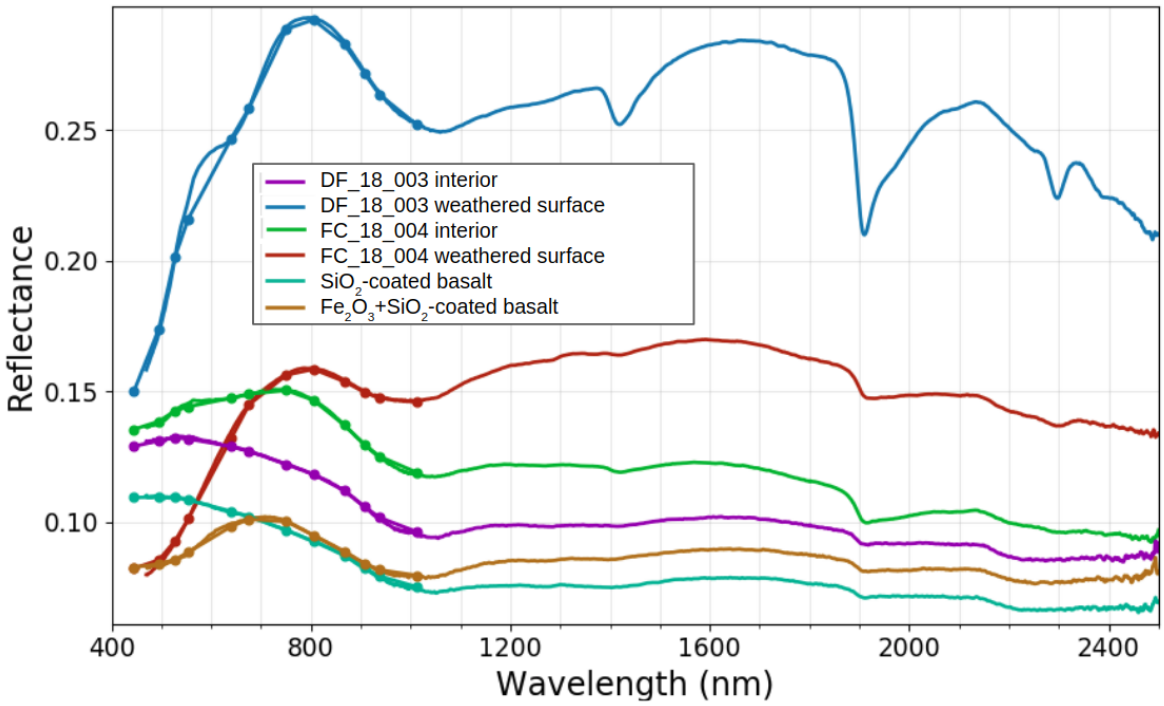

Figure 48: Data convolved to Mastcam filter locations is overlain on a spectrum for each of the materials used in this study. Each color corresponds to a different sample, with solid lines showing lab spectra and dots indicating convolved values at each Mastcam filter location. For simplicity, this plot shows only a single geometry for each sample, but data was convolved at all geometries measured.

Using these convolved spectra, photometric analyses were repeated for each sample type. With the exception of photometric trends measured outside Mastcam's spectral range (e.g. slopes 1500-1700 nm) all photometric trends observed in laboratory spectra would be equally detectable using Mastcam on Mars (Figures 49-52).

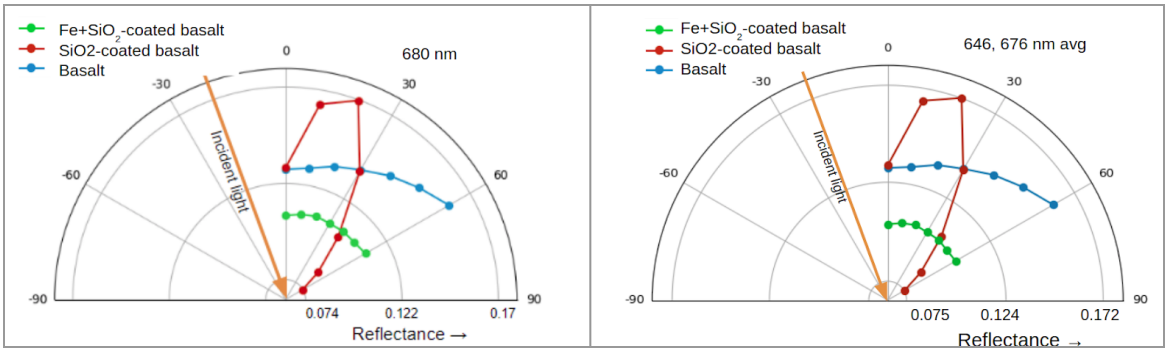

Figure 49: Photometric analyses of laboratory spectra (left) were repeated for convolved spectra (right) for specularity of coated samples. Trends are equally observable in laboratory and convolved spectra.

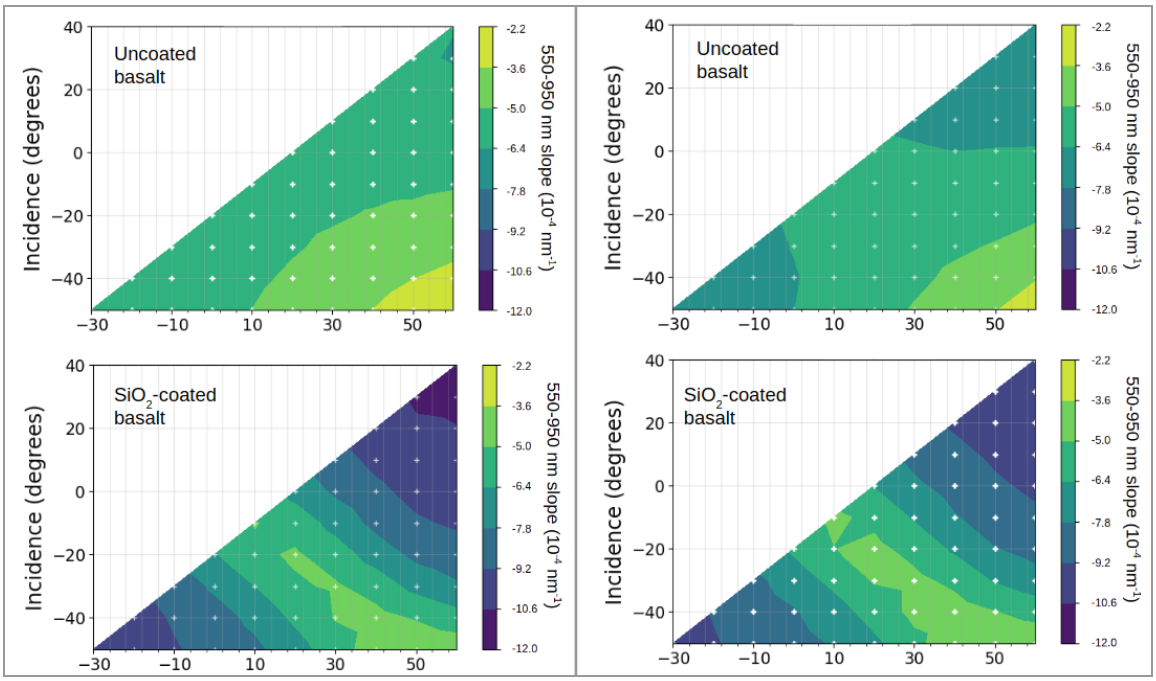

Figure 50: Photometric analyses of laboratory spectra (left) were repeated for convolved spectra (right) for photometry of the slope 550-950 nm. Trends are equally observable in laboratory and convolved spectra.

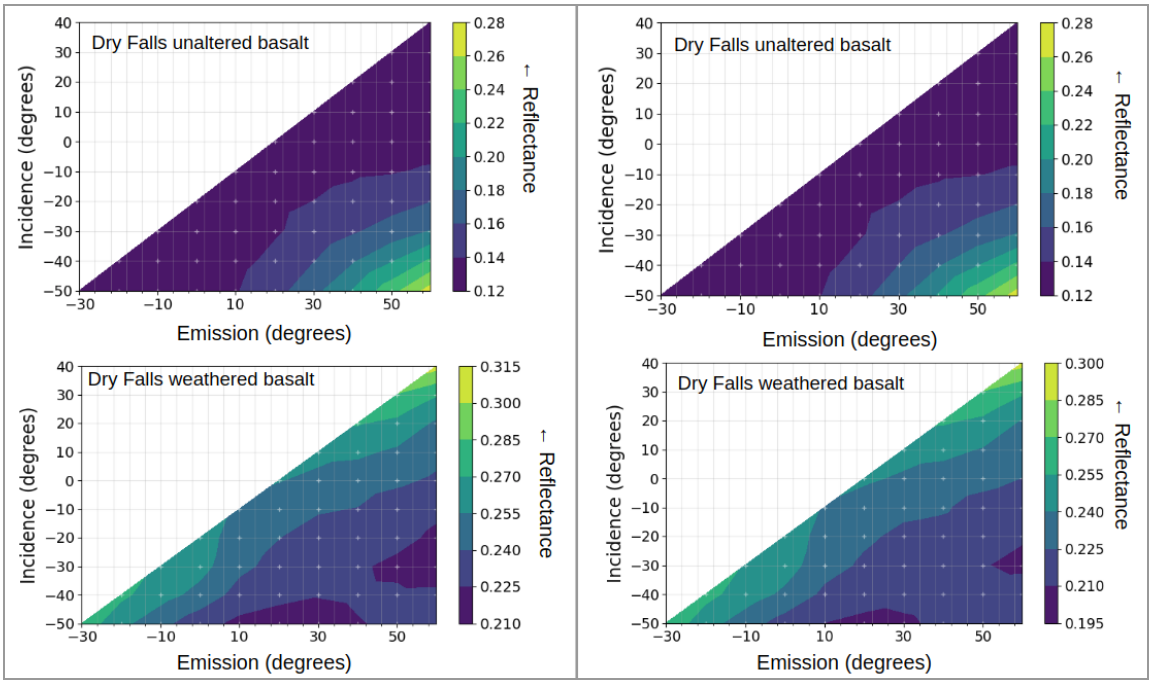

Figure 51: Photometric analyses of laboratory spectra (left) were repeated for convolved spectra (right) for scattering lobe shape of DF_18_003's unaltered interior (top, forward scattering) as compared to its weathering rind (bottom, backscattering). This trend is equally observable in laboratory and convolved spectra.

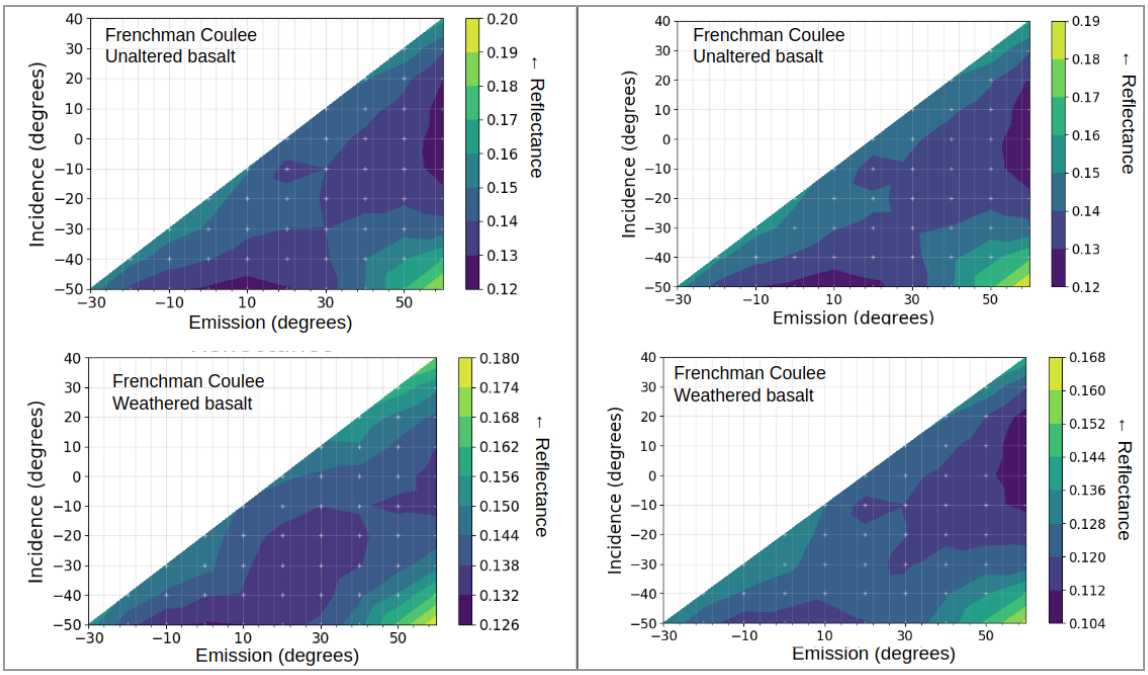

Figure 52: Photometric analyses of laboratory spectra (left) were repeated for convolved spectra (right) for scattering lobe shape of FC_18_004's unaltered interior (top, forward scattering) as compared to its weathering rind (bottom, also forward scattering). This similarity is equally observable in laboratory and convolved spectra.

5.2.3.3 Example operations scenario

Detection and characterization of weathering rinds and coatings on Mars would likely be a multi-step process involving multiple instruments on different spacecraft. Preliminary observations and photometry characterizations of large regions of the surface could be carried out using data from CRISM. Photometric trends identified through this work could inform rover science operations team decisions, and lead to further photometric characterizations with higher spatial resolution on the ground using Mastcam. These observations could then be used to identify specific rock targets of interest, which could be characterized in detail using other analytical tools on the rover. In particular, the ChemCam instrument could create a profile of composition as a function of depth for a rock target by collecting spectra immediately when the laser began to fire, rather than ignoring the first few laser bursts as is commonly done when the intention is to measure bulk rock composition.

6. Conclusions and Future Work

6.1 Summary of findings

This project represents some of the first photometric research on naturally-weathered rock surfaces as well as providing photometric datasets for Mars-relevant synthetic coatings. A summary of the major findings of this project are as follows:

1. Mars-relevant synthetic coatings exhibit distinctive photometric trends, even when these coatings are so thin as to be largely invisible in standard-geometry spectra. Specifically, the results of this work indicate that observations of photometric trends (as exemplified by the slopes from 550-950 nm and 1500-1700 nm) combined with measurements of specularity may provide a robust means to detect pure silica coatings where they might otherwise be overlooked. And, while the addition of Fe^{3+} limits the usefulness of the

550-950 nm slope measurement, scattering lobe shape and the 1500-1700 nm slope continue to be distinct from uncoated rocks. Similar silica-rich coatings have been hypothesized to be widespread on Mars, and because of the hypothesized connection between silica coatings and aqueous conditions, the detection of similar coatings on Mars would have significant implications for habitability. This means that this new technique could lead to a significant step forward in our understanding of martian paleoclimate. However, because the scope of this work was limited to very simple synthetically coated samples, the applicability of our results needs to be verified via the photometric characterization of a suite of naturally silica-coated analog samples.

2. Through detailed photometric, spectroscopic, mineralogical, and chemical investigations of two representative naturally-weathered rocks, it has been found that major weathering-induced changes in photometry may be primarily the result of textural changes, with increased pore space linked to backscattering photometric behavior. More work remains to be done to understand how these textural changes may be linked to environmental conditions. Interestingly, mineralogical changes classically associated with weathering processes, including clay formation, were not observed for the rocks characterized. Instead, mineralogy and chemistry were observed to show only minor changes from the rock interior to the rind.

In addition to these findings, a major outcome of the project is the development of an automated spectrogoniometer system for characterizing the photometry of naturally-weathered surfaces. This system is able to take spectra at high angular resolution in a time-efficient and repeatable manner, and it can accommodate large naturally-weathered samples rather than being limited to small homogeneous powder samples. However, because polarization effects related to both the

light source and the detector may be influencing this system's measurements, the spectrogoniometer should be improved by incorporating light source and detector depolarizers into the design. And, especially in light of the unexplained non-reciprocity of the data published by Biliouris et al. (2010), the BRDF of Spectralon® should be independently verified to ensure the validity of our calibration procedure.

6.2 Future directions

This project has laid the groundwork for numerous further photometric studies. With the functioning goniometer system in place, detailed photometric characterizations can be carried out with relative ease, which will enable future researchers to efficiently investigate a variety of surfaces from a broad suite of weathering environments. The resulting rich photometric dataset will be used to improve understanding of martian surface processes in two major ways. First, it will help researchers investigating bulk rock compositions to untangle the effects of thin coatings and rinds from the signal they are looking for. And second, it will create a new tool for characterizing martian weathering processes via the detection of weathering rinds and coatings linked to specific weathering environments on Earth. Ultimately, these correlations will be used to inform conclusions about past and present environmental conditions on Mars and lead to a deeper understanding of the Red Planet's geology.

Because this project has demonstrated the high value of photometric measurements for characterizing Mars-relevant surfaces, a proposal has been submitted to NASA's Solar System Workings grant program to fund ongoing work. As one component of that proposal, a preliminary design for a new, 3-dimensional goniometer has been completed by engineering company First Mode (Figure 53).

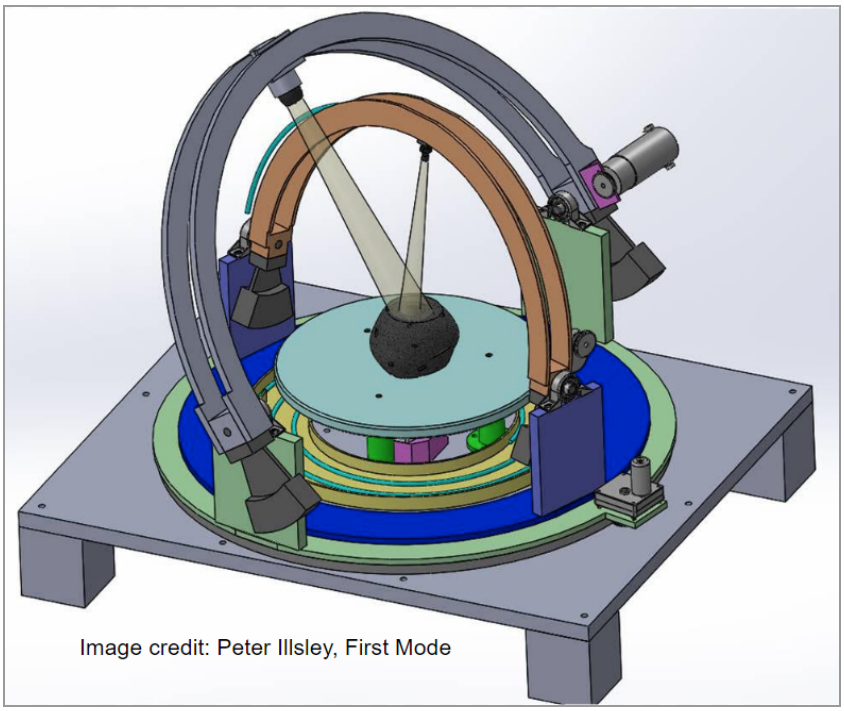

Figure 53: A conceptual design for a planned 3D goniometer will enable measurements of azimuthal effects and an expanded range for incidence and emission angles.

This new goniometer will have all the features of our existing 2D goniometer with respect to angular resolution, sample accommodation, and time-efficient and repeatable automated data collection, but it will additionally allow for a full range of azimuth angles and an expanded range of incidence and emission angles. This will enable future researchers to characterize photometric functions in more detail, opening the door to more precise interpretations of photometric trends observed by spacecraft and more insights into planetary geology.

7. Bibliography

Arvidson, R. E., Squyres, S. W., Bell, J. F., Catalano, J. G., Clark, B. C., Crumpler, L. S., … Wolff, M. J. (2014). *Ancient Aqueous Environments at Endeavour Crater, Mars. Science, 343(6169), 1248097–1248097.*doi:10.1126/science.1248097

Bandfield, J. L., Hamilton, V. E. & Christensen, P. R. A global view of martian surface compositions from MGS-TES. Science 287, 1626–1630 (2000).

Bell, J.F., III, T.B. McCord, and P.D. Owensby (1990), Observational evidence of crystalline iron oxides on Mars, J. Geophys. Res. 95, 14447–61.
Bibring, J.-P. (2006). Global Mineralogical and Aqueous Mars History Derived from OMEGA/Mars Express Data. Science, 312(5772), 400–404. doi:10.1126/science.1122659 Clark, B.E. et al. (2002), NEAR Infrared Spectrometer Photometry of Asteroid 433 Eros, Icarus, 155, 189.

Bell, J. F., III, et al. (2003), Mars Exploration Rover Athena Panoramic Camera (Pancam) investigation, J. Geophys. Res., 108(E12), 8063, doi:10.1029/2003JE002070

Bell, J. F., J. N. Maki, G. L. Mehall, M. A. Ravine and M. A. Caplinger (2014), Mastcam-Z: A geologic, stereoscopic, and multispectral investigation on the NASA Mars-2020 Rover, International Workshop on Instrumentation for Planetary Missions, Greenbelt, Maryland.
Biliouris, D. et al. (2007), A Compact Laboratory Spectro-Goniometer (CLabSpeG) to Assess the BRDF of Materials. Presentation, Calibration and Implementation on Fagus sylvatica L. Leaves, *Sensors* 7 1846-1870

Bishop, J. L., Dobrea, E. Z. N., McKeown, N. K., Parente, M., Ehlmann, B. L., Michalski, J. R., … Bibring, J.-P. (2008). *Phyllosilicate Diversity and Past Aqueous Activity Revealed at Mawrth Vallis, Mars. Science, 321(5890), 830–833.*doi:10.1126/science.1159699
Bruegge, C.; Chrien, N. and Haner, D. A Spectralon BRF data base for MISR calibration applications. Remote Sens. Environ. 2001, 76, 354-366.

Buz, J. (2017), Mastcam-Z Calibration Target Analysis. Ehlman Lab, Caltech.

Camp, V.E., Reidel, S.P., Ross, M.E., Brown, R.J., and Self, S., 2017, Field-trip guide to the vents, dikes, stratigraphy, and structure of the Columbia River Basalt Group, eastern Oregon and southeastern Washington: U.S. Geological Survey Scientific Investigations Report 2017–5022–N, 88 p., https://doi.org/10.3133/sir20175022N

Chemtob, S. M., B. L. Jolliff, G. R. Rossman, J. M. Eiler, and R. E. Arvidson (2010), Silica coatings in the Ka'u Desert, Hawaii, a Mars analog terrain: A micromorphological, spectral, chemical, and isotopic study, J. Geophys. Res., 115, E04001, doi: 10.1029/2009JE003473.

Clark, R.N., Roush, T.L. (1984). Reflectance spectroscopy—Quantitative analysis techniques for remote sensing applications. J. Geophys. Res. 89, 6329–6340.

Clarke, F. J. J., & Parry, D. J. (1985). Helmholtz Reciprocity: its validity and application to reflectometry. Lighting Research & Technology, 17(1), 1–11. doi:10.1177/14771535850170010301

Cloutis, E.A., M.J. Gaffey, T.L. Jackowski, K.L. Reed (1986), Calibrations of Phase Abundance, Composition, and Particle Size Distribution for Olivine-Orthopyroxene Mixtures from Reflectance Spectra, J. Geophys. Res., 91, 811.

Cloutis, E.A., M.A. Craig, L. Kaletzke, K. McCormack, L. Stewart (2006). HOSERLab: A new planetary spectrophotometer facility. Lunar Planet. Sci. Conf. XXXVII. Abstract 2121.

Cloutis, E. A., Craig, M. A., Kruzelecky, R. V., Jamroz, W. R., Scott, A., Hawthorne, F. C., & Mertzman, S. A. (2008). *Spectral reflectance properties of minerals exposed to simulated Mars surface conditions. Icarus, 195(1), 140–168.*doi:10.1016/j.icarus.2007.10.028

Cloutis, E.A., M.A. Craig, R.V. Kruzelecky, W.R. Jamroz, A. Scott, F.C. Hawthorne, and S.A. Mertzman (2008), Spectral reflectance properties of minerals exposed to simulated Mars surface conditions, Icarus, 195, 140–168.

Colman, S.M. (1982). Chemical weathering of basalts and andesites; evidence from weathering rinds USGS Paper No. 1246

Crisp, J. and M.J. Bartholomew, Mid-infrared spectroscopy of Pahala ash palagonite and implications for remote sensing studies of Mars (1992), J. Geophys. Res., 97, E9, 14,691-14,699.

Dorn, R.I. (1995). Digital processing of back-scatter electron imagery: A microscopic approach to quantifying chemical weathering. GSA Bulletin, 107(6), 725-741.

Dorn, R.I. (2013). Rock coatings. In: Shroder, J. (Editor in Chief), Pope, G.A., (Ed.), Treatise on Geomorphology. Academic Press, San Diego, CA, vol. 4, Weathering and Soils Geomorphology, pp. 70–97/.

Ehlmann, B.L., D.L. Bish, S.W. Ruff, J.F. Mustard (2012), Mineralogy and chemistry of altered Icelandic basalts: Application to clay mineral detection and understanding aqueous environments on Mars, J. Geophys. Res., 117, E00J16.

Ehlmann, B.L., G. Berger, N. Mangold, J.R. Michalski, D.C. Catling, S.W. Ruff, E. Chassefière, P.B. Niles, V. Chevrier, F. Poulet (2013). Geochemical Consequences of Widespread Clay Mineral Formation in Mars' Ancient Crust. Space Science Reviews, 174(1-4), 329–364. http://doi.org/10.1007/s11214-012-9930-0.

Fernando, J. et al. (2015), Characterization and mapping of surface physical properties of Mars from CRISM multi-angular data: Application to Gusev Crater and Meridiani Planum. Icarus 253, 271–295.

Fischer, E.M. and Pieters, C.M. (1993) The Continuum Slope of Mars: Bidirectional Reflectance Investigations and Applications to Olympus Mons, Icarus, Volume 102, Issue 2, Pages 185-202, ISSN 0019-1035, https://doi.org/10.1006/icar.1993.1043.

Frey, H.M., K.J. Szramek, M.R. Manon, M.T. Kissane (2013). Slow chemical weathering in a semiarid climate: Changes in the mineralogy and geochemistry of subaerial lava flows in the Deschutes River Basin, central Oregon. Chemical Geology, 347, 135-152

Gordon, S.J., R.I Dorn (2005). In situ weathering rind erosion. Geomorphology, 67(1), 97-113

Grotzinger, J.P. et al. (2013), A Habitable Fluvio Lacustrine Environment at Yellowknife Bay, Gale Crater, Mars, Science, 342, doi:10.1126/science.1242777.

Guinness, E. A., Arvidson, R. E., Dale-Bannister, M. A., Singer, R. B., & Bruckenthal, E. A. (1987). On The spectral reflectance properties of materials exposed at the Viking landing sites. Journal of Geophysical Research: Solid Earth, 92(B4), E575–E587. doi:10.1029/jb092ib04p0e575

Guinness, E.A., R.E. Arvidson, I. Clark, and M.K. Shepard (1997), Optical scattering properties of terrestrial varnished basalts compared with rocks and soils at the Viking Lander sites, J. Geophys. Res. 102, 28687–703.

Hapke, B., 1981. Bidirectional reflectance spectroscopy. 1. Theory. J. Geophys. Res. 86, 3039–3054.

Hapke, B., Wells, E., 1981. Bidirectional reflectance spectroscopy. 2. Experiments and observations. J. Geophys. Res. 86, 3055–3060.

Hapke, B., 1984. Bidirectional reflectance spectroscopy. 3. Correction for macroscopic roughness. Icarus 59, 41–59.

Hapke, B., 1986. Bidirectional reflectance spectroscopy. 4. The extinction coefficient and the opposition effect. Icarus 67, 264–280.

Hapke, B., 1993. Theory of Reflectance and Emittance Spectroscopy. Cambridge University Press, NY, NY.

Hapke, B., Nelson, R., Smythe, W., 1998. The opposition effect of the Moon: Coherent backscatter and shadow hiding. Icarus 133, 89–97.

Hapke, B., 2002. Bidirectional reflectance spectroscopy. 5. The coherent backscatter opposition effect and anisotropic scattering. Icarus 157, 523–534.

Hapke, B., 2008. Bidirectional reflectance spectroscopy. 6. Effects of porosity. Icarus 195, 918–926.

Hapke, B.W., Shepard, M.K., Nelson, R.M., Smythe, W.D., Piatek, J., 2009. A quantitative test of the ability of models based on the equation of radiative transfer to predict the bidirectional reflectance of a well-characterized medium. Icarus 199, 210–218.

Horgan, B. and J.F. Bell III (2012), Widespread weathered glass on the surface of Mars, Geology, 40, 5, 391–394.

Jackson et al. (1992), Bidirectional Calibration Results for 11 Spectralon and 16 BaSO4 Reference Reflectance Panels, *Remote Sensing of the Environment* 40:231-239.

Johnson, J.R., et al. (1999), Preliminary results on photometric properties of materials at the Sagan Memorial Station, Mars, J. Geophys. Res., 104, 8809–30.

Johnson, J.R., and W. M. Grundy (2001), Visible/near-infrared spectra and two-layer modeling of palagonite-coated basalts, Geophys. Res. Lett., 28, 2101–2104, doi:10.1029/2000GL012669.

Johnson, J.R., et al. (2006), Radiative transfer modeling of dust-coated Pancam calibration target materials: Laboratory
visible/near-infrared spectrogoniometry, J. Geophys. Res., 111, E12S07, doi:10.1029/2005JE002658.

Johnson, J.R., Shepard, M.K., Grundy, W.M., Paige, D.A., and Foote, E.J. (2013), Spectrogoniometry and modeling of martian and lunar analog samples and Apollo soils. Icarus, 223(1) 383-406. doi:10.1016/j.icarus.2012.12.004
Knoll, A.H., et al. (2008), Veneers, rinds, and fracture fills: Relatively late alteration of sedimentary rocks at Meridiani
Planum, Mars, J. Geophys. Res., 113, E06S16, doi:10.1029/2007JE002949.

Kraft, M. D., and R. Greeley (2000), Rock coatings and aeolian abrasion on Mars: Application to the Pathfinder landing site, *J. Geophys. Res.*, 105(E6), 15107–15116, doi: 10.1029/1999JE001229.

Kraft, M.D., J.R. Michalski, T.G. Sharp (2003). Effects of pure silica coatings on thermal emission spectra of basaltic rocks:
Considerations for Martian surface mineralogy. Geophys. Res. Lett., 30(24), 2288–4. doi:10.1029/2003GL018848

Ladouceur, F., & Poladian, L. (1996). Surface roughness and backscattering. Optics Letters, 21(22), 1833. doi:10.1364/ol.21.001833

Lanza, N. L., et al. (2016), Oxidation of manganese in an ancient aquifer, Kimberley formation, Gale crater, Mars, *Geophys. Res. Lett.*, 43, 7398–7407, doi: 10.1002/2016GL069109.

Levesque et al. (2014). Polarization artefacts correction procedure for a spectro-polarimetric goniometer. 10.1109/IGARSS.2014.6947108.

Lichtenberg, K.A., et al. (2007), Coordinated analyses of orbital and Spirit Rover data to characterize surface materials on the cratered plains of Gusev Crater, Mars, J. Geophys. Res., 112, E12S90, doi:10.1029/2006JE002850.

Long, Philip & Wood, Bernard. (1986). Structures, textures, and cooling histories of Columbia River Basalt flows. Geological Society of America Bulletin - GEOL SOC AMER BULL. 97. 10.1130/0016-7606(1986)97<1144:STACHO>2.0.CO;2.

Malin, M. C., et al. (2010), The Mars Science Laboratory (MSL) mast-mounted cameras (Mastcams) flight instruments, 41st Lunar Planet. Sci. Conf., held March 1–5, 2010 in The Woodlands, Texas. LPI Contrib. 1533, p.1123.
Minnaert, M., 1941. The reciprocity principle in lunar photometry. SAO/NASA Astrophysics Data System (ADS).

Michalski, J. R., Kraft, M. D., Sharp, T. G., & Christensen, P. R. (2006). Effects of chemical weathering on infrared spectra of Columbia River Basalt and spectral interpretations of martian alteration. *Earth and Planetary Science Letters*, *248*(3-4), 822-829. DOI: 10.1016/j.epsl.2006.06.034

Minitti, M., C.M. Weitz, M.D. Lane, and J.L. Bishop, Morphology, chemistry, and spectral properties of Hawaiian rock coatings and implications for Mars (2007), J. Geophys. Res., 112, E05015, doi:10.1029/2006JE002839.

Morris, R. V., et al. (2006), Mo¨ssbauer mineralogy of rock, soil, and dust at Gusev crater, Mars: Spirit's journey through weakly altered olivine basalt on the Plains and pervasively altered basalt in the Columbia Hills, J. Geophys. Res., doi:10.1029/2005JE002584, in press.

Murchie, S., et al. (2007), Compact Reconnaissance Imaging Spectrometer for Mars on Mars Reconnaissance Orbiter, J. Geophys. Res., doi:10.1029/2006JE002682, in press.

Murchie, S. L., Mustard, J. F., Ehlmann, B. L., Milliken, R. E., Bishop, J. L., McKeown, N. K., … Bibring, J.-P. (2009). *A synthesis of Martian aqueous mineralogy after 1 Mars year of observations from the Mars Reconnaissance Orbiter. Journal of Geophysical Research, 114.*doi:10.1029/2009je003342

Painter, T.H.; Paden, B. and Dozier, J. Automated spectro-goniometer: A spherical robot for the field measurement of the directional reflectance of snow. Rev. of Scient. Instr. 2003, 74, 12, 5179- 5188.

Pieters, C. M. (1983), Strength of mineral absorption features in the transmitted component of near-infrared reflected light: First results from RELAB, *J. Geophys. Res.*, 88(B11), 9534–9544, doi:10.1029/JB088iB11p09534.

Pilorget, C., J. Fernando, B.L. Ehlmann, F. Schmidt, T. Hiroi (2016). Wavelength dependence of scattering properties in the VIS-NIR and links with grain-scale physical and compositional properties. Icarus, 267, 296–314.

Pommerol, A., & Schmitt, B. (2008). Strength of the H2O near-infrared absorption bands in hydrated minerals: Effects of particle size and correlation with albedo. Journal of Geophysical Research, 113(E10).doi:10.1029/2007je003069

Pommerol, A. et al. (2013), Photometric properties of Mars soils analogs. J. Geophys. Res. 118, 2045–2072.

Poppe, L.J., V.F. Paskevich, J.C. Hathaway, and D.S. Blackwood. (2002). A Laboratory Manual for X-Ray Powder Diffraction. United States Geological Survey Open-File Report 01-041. U.S. Geological Suvey, MA.

Rampe, E. B., M.D. Kraft, T.G. Sharp (2013). Deriving chemical trends from thermal infrared spectra of weathered basalt: Implications for remotely determining chemical trends on Mars. Icarus, 225(1), 749-762.

Rice, M.S., E.A. Cloutis, J.F. Bell III, S.A. Mertzman, D.L. Bish, M. Craig, B. Mountain, R.W. Renaut, B. Gautason (2013). Reflectance spectra diversity of silica-rich materials: Sensitivity to environment and implications for detections on Mars. Icarus, 223, 499–533. doi:10.1016/j.icarus.2012.09.021

Roger C. Wiens, et al. (2012). The ChemCam Instrument Suite on the Mars Science Laboratory (MSL) Rover: Body Unit and Combined System Tests. Space Science Reviews, Volume 170. 167-227.

Sak, P.B. et al. (2010). Controls on rind thickness on basaltic andesite clasts weathering in Guadeloupe. Chemical Geology, 276(3), 129-143.

Salvatore, M.R., J.F. Mustard, J.W. Head, R.F. Cooper, D.R. Marchant, M.B. Wyatt (2013). Development of alteration rinds by oxidative weathering processes in Beacon Valley, Antarctica, and implications for Mars. Geochimica et Cosmochimica Acta, 115, 137-161.

Sandmeier, St. Acquisition of Bidirectional Reflectance Factor Data with Field Goniometers. Remote Sens. Environ. 2000, 73, 257-269.

Sato, H., M.S. Robinson, B. Hapke, B.W. Denevi, and A.K. Boyd (2014), Resolved Hapke parameter maps of the Moon, J. Geophys. Res. Planets, 119, 1775–1805, doi:10.1002/2013JE004580.

Schaepman, M.E. and Dangel, S. Solid laboratory calibration of a nonimaging spectroradiometer. Applied Opt. 2000, 39, 21, 3753-3765.

Schmidt, F., J. Fernando (2015), Realistic uncertainties on Hapke model parameters from photometric measurement. Icarus 260, 73–93.

Seelos, K.D., R.E. Arvidson, B.L. Jolliff, S.M. Chemtob, R.V. Morris, D.W. Ming, G.A. Swayze (2010), Silica in a Mars analog environment: Ka'u Desert, Kilauea Volcano, Hawaii, J. Geophys. Res., 115, E00D15, doi:10.1029/2009JE003347

Serrot, G.; Bodilis, M.; Briottet, X. and Cosnefroy, H. Presentation of a new BRDF measurement device. The European Symposium on Remote Sensing, SPIE, Euporto, Barcelona, Spain 1998, 3493, 34-40.
Shepard, M.K., P. Helfenstein, (2007). A test of the Hapke photometric model. J. Geophys. Res. 112, E03001.

Shepherd, M.K., P. Helfenstein, (2011) A laboratory study of the bidirectional reflectance from particulate samples. *Icarus* 215 526-533.

Shkuratov, Y., L. Starukhina, H. Hoffmann, G. Arnold (1999). A Model of Spectral Albedo of Particulate Surfaces: Implications for Optical Properties of the Moon. Icarus, 137(2), 235–246. http://doi.org/10.1006/icar.1998.6035

Singer, R.B., T.L. Roush (1983), Spectral Reflectance Properties of Particulate Weathered Coatings on Rocks: Laboratory Modeling and Applicability to Mars. LPSC XIV, p. 708.

Snyder, W, (1998) Reciprocity of the Bidirectional Reflectance Distribution Function (BRDF) in Measurements and Models of Structured Surfaces

Solheim, I.; Hosgood, B.; Andreoli, G. and Piironen, J. Calibration and Characterization of Data from the European Goniometer Facility (EGO). Joint Research Centre, Report EUR 17268 EN, 1996, pp 169.

Solomon, S. et al. (2005). New Perspectives on Ancient Mars. Science, 307(5713), 1214–1220.

Sun, DW, and Yunfeng, LV. (2017). Photopolarimetric properties of a manmade target over a wide range of measurement directions. Optics Express.

Veverka, J. et al. (1988). Photometry and polarimetry of Mercury. In: Mercury. University of Arizona Press, pp. 37–58.

Wyatt, M. B., and H. Y. McSween (2002). Spectral evidence for weathered basalt as an alternative to andesite in the northern lowlands of Mars, Nature, 417, 263 – 266